NOTICE

The quality of this microform is heavily dependent upon the quality of the original thesis submitted for microfilming. Every effort has been made to ensure the highest quality of reproduction possible.

If pages are missing, contact the university which granted the degree.

Some pages may have indistinct print especially if the original pages were typed with a poor typewriter ribbon or if the university sent us an inferior photocopy.

Previously copyrighted materials (journal articles, published tests, etc.) are not filmed.

Reproduction in full or in part of this microform is governed by the Canadian Copyright Act, R.S.C. 1970, c. C-30.

AVIS

La qualité de cette microforme dépend grandement de la qualité de la thèse soumise au microfilmage. Nous avons tout fait pour assurer une qualité supérieure de reproduction.

S'il manque des pages, veuillez communiquer avec l'université qui a conféré le grade.

La qualité d'impression de certaines pages peut laisser à désirer, surtout si les pages originales ont été dactylographiées à l'aide d'un ruban usé ou si l'université nous a fait parvenir une photocopie de qualité inférieure.

Les documents qui font déjà l'objet d'un droit d'auteur (articles de revue, tests publiés, etc.) ne sont pas microfilmés.

La reproduction, même partielle, de cette microforme est soumise à la Loi canadienne sur le droit d'auteur, SRC 1970, c. C-30.

Canada

PROPERTIES OF THE SEMIMAGNETIC SEMICONDUCTOR ALLOY

$Zn_{2x}(CuIn)_yMn_{2z}Te_2$ (x+y+z = 1)

by

CHAMPA R. NEAL

Thesis

presented to the University of Ottawa

in partial fulfillment of the

requirements for the degree of

Master of Science

in

Physics

University of Ottawa

Department of Physics

Ottawa, Ontario

1987

ISBN 0-315-40726-3

UNIVERSITÉ D'OTTAWA
UNIVERSITY OF OTTAWA

ABSTRACT

A study of some crystallographic, optical and magnetic properties of the pseudo-ternary alloy system $Zn_{2x}(CuIn)_yMn_{2z}Te_2$ is presented in this report.

Polycrystalline samples of this alloy system were prepared from the elements by the standard melt and anneal technique. A total of 60 different alloy compositions were made for the experiments described in this work. Debye-Scherrer x-ray powder photographs were obtained for each sample to check the homogeneity. The lattice parameter *a*, determined from the photographs were plotted as a function of composition and thus the range of zinc blende single phase, chalcopyrite single phase and two phase fields were found. Fitting of lattice parameter values was done by using a simple empirical equation and this was used to draw contours of constant lattice parameter.

Energy gap values E_g were investigated by using the optical absorption technique for all samples in the single cubic phase and for some in the chalcopyrite phase. Values of E_g for these phases were plotted as a function of composition. These energy gap values extrapolated to different a points at z=1.0 and it is clear that these aiming points of E_g vs z lines vary with the structure concerned. This fact can be used to determine or confirm the boundaries of the various fields.

Measurements of magnetic susceptibility were carried out using a SQUID magnetometer in the temperature range $4.2 \leq T \leq 250K$. From these, values for the spin glass transition temperature, T_g and for the Curie Weiss temperature , θ were determined. These parameters were plotted as a function of composition. The results indicated that

despite the apparent single phase appearence of the x-ray photographs, two different magnetic phases were found and these were attributed to crystallographic ordering of the manganese atoms. For many samples, the susceptibility measurements showed two transition temperatures, the lower one was attributed to the disordered structure and the higher one to the ordered structure. The variation of these transition temperatures with z produced different lines for the chalcopyrite and cubic structures. A study of the exchange interaction using these T_g values for the disordered structure suggested that the magnetic spins were coupled to each other indirectly through antiferromagnetic superexchange. This invoved a virtual transition between the valence band and non-localized Mn 3d band. Nearest and next nearest exchange parameter values, J_1 and J_2, were predicted using this exchange mechanism and they agreed fairly well with those determined previously from other types of measurements.

The ESR spectrum was studied as a function of temperature. Two lines corresponding to the ordered and disordered structures were observed. The variation of the ESR linewidth with temperature indicated that the disordered phase showed spin glass behavior. The structure of the ordered phase has not as yet been determined.

ACKNOWLEDGEMENTS

I would like to express my thanks to Professor John C. Woolley for his assistance, encouragement and unlimited patience throughout the course of this work.

I would like to acknowledge the help I received from Professor G. Lemarche in magnetic susceptibility measurements and Professor A. Manoogian in ESR work.

I wish to thank Tom Donofrio andSamir Chehab for the considerable number of discussions and for the help received on the use of the computing facilities.

Special thanks to Mr. Bei Wah Chan for handling the technical aspects of the ESR measurements.

My gratitude also goes to a very special person, my husband Alan for patience encouragement and understanding during the course of this work.

TABLE OF CONTENTS

LIST OF FIGURES

Chapter 1

General Introduction

During the past several years the materials which are known as "semimagnetic semiconductors" have attracted a great deal of attention for several reasons. This new group of semiconducting materials are defined as either semimagnetic semiconductors (SMSC) which was suggested by Galazka (1) or diluted magnetic semiconductors (DMS) named by Furdyna (2). These semimagnetic semiconductors can be obtained by replacing some non-magnetic ions in a semiconductor by a magnetic ion such as Mn, Fe , Cr etc. The most common examples for SMSC are $Cd_{1-z}Mn_zTe$, $Zn_{1-z}Mn_zTe$, $Cd_{1-z}Mn_zSe$, $Hg_{1-z}Mn_zTe$, and $Hg_{1-z}Mn_zSe$. The range of composition of the above SMSC are $z \leq 0.7$, $z \leq 0.78$, $z \leq 0.3$, $z \leq 0.5$, and $z \leq 0.3$ respectively. The ranges given correspond to compositions in which good quality single phase crystals have been actually grown and used in research (2). These materials can in several instances be synthesized up to somewhat higher values of z (2), but when the Mn content exceeds that shown above , the crystals of these alloys tend to be of poorer quality and or to contain precipitates of other phases (e. g. MnTe, $MnTe_2$). Semimagnetic semiconductors are thus the solid solutions between ordinary semiconductors for which $z = 0$ and magnetic semiconductors for which $z = 1.0$. If the process is regarded as dilution of a magnetic semiconductor with a non magnetic component, we can refer to them as diluted magnetic semiconductors.

As with the large majority of these SMSC in the literature, in the present work Mn has been used as the magnetic component in the alloy system. As a result of introducing magnetic ions, interesting magnetic and optical properties can be obtained. Since manganese contains five bound and unpaired d electrons, it gives the atom a net magnetic moment. The

interaction of these electrons with each other as well as with the band electrons via exchange interaction, gives rise to interesting magnetic and magneto-optical properties. Antiferromagnetic interactions between manganese ions distributed randomly with non-magnetic ions can lead to interesting magnetic behavior such as the spin glass effects predicted theoretically (3) and observed in these materials (4-5). Numerous types of measurements have been made (6-7-8) on these materials. Optical energy gap, magnetic susceptibility, low temperature specific heat and electron spin resonance are some of the measurements that have been done by the researchers mentioned above. Some of these measurements have been extended to pseudo-ternary systems such as $Cd_xZn_yMn_zTe$, $Cd_xZn_yMn_zSe$ ($x+y+z = 1$) with a zinc blende structure. If the alloy so produced is to be a semiconductor, then the ratio of electron to atom must be conserved. That is on the average , the magnetic ions must replace non-magnetic cations of the same valency. Most of the work on such alloys (1-2) has been concerned with replacement by manganese of the divalent elements Zn, Hg, Cd etc. (e.g. $Zn_{1-z}Mn_zTe$). However it is possible to produce similar alloys from chalcopyrite I II VI_2 compounds, the ternary analogs of the II VI compounds. If the paramagnetic ion to be introduced is divalent Mn, then to retain the ratio of electron to atom, I and III cations have to be replaced by two manganese atoms giving alloys of the form $(I\text{-}III)_{1-z}Mn_{2z}Te_2$. Examples of these alloys are $Zn_{2x}(CuIn)_yMn_{2z}Te_2$, $Cd_{2x}(CuIn)_yMn_{2z}Te_2$ and $Cd_{2x}(CuGa)_yMn_{2z}Te_2$ ($x+y+z= 1$). In this thesis, a systematic study of the properties of $Zn_{2x}(CuIn)_yMn_{2z}Te_2$ over a broad composition range has been undertaken.

In a ternary system, phase equilibria can be given as a function of temperature with two compositions as independent variables. If any pseudo ternary alloy is described as $A_xB_yC_zD$ with $x+y+z= 1$, then the compositions of the alloy can be represented by a triangle as shown in Fig (1.1). Each point in the triangle represents a particular value of x, y and z

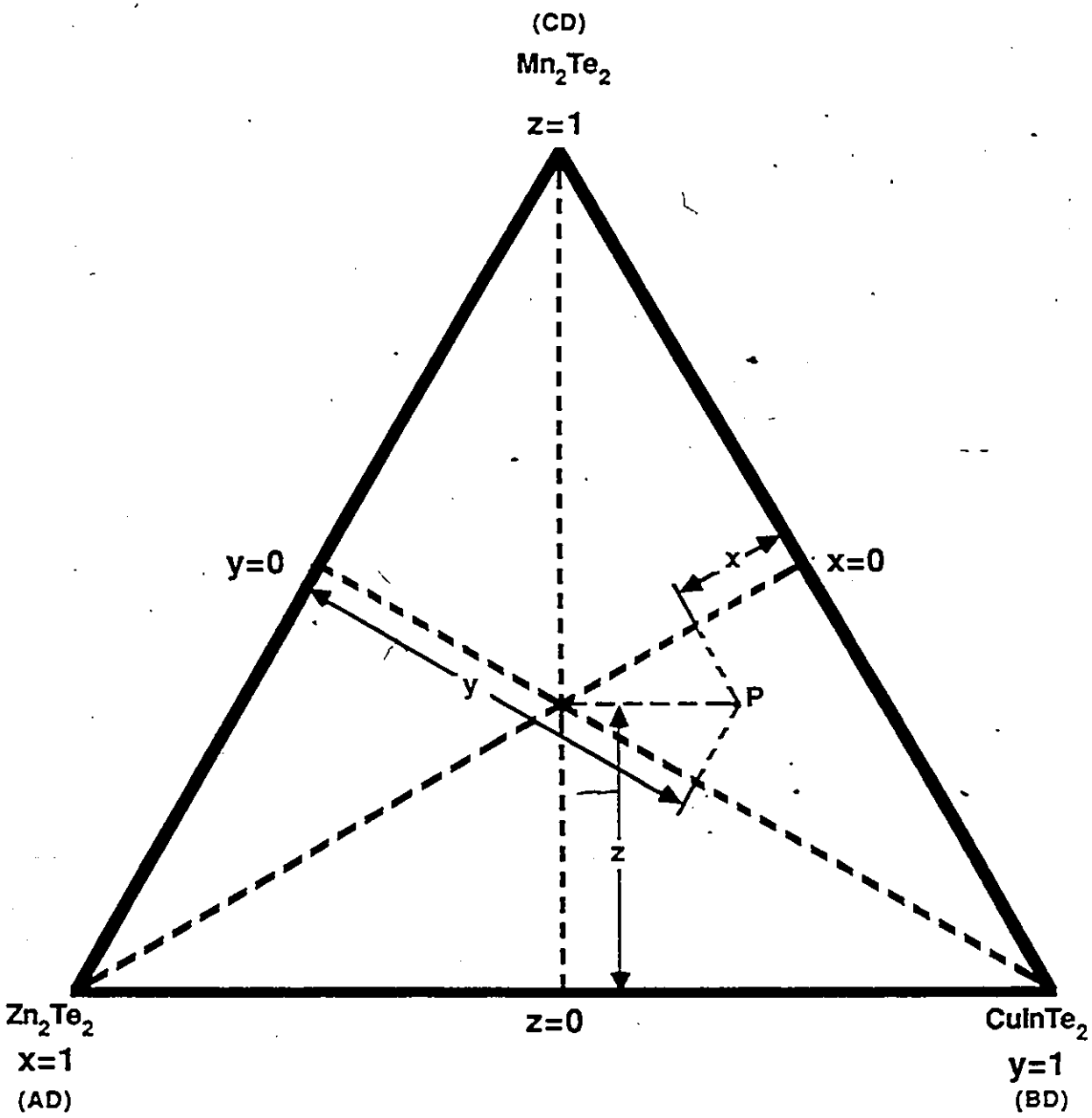

Fig (1.1) Triangular Coordinate System.
Any point 'P' in the diagram represents a sample of composition (x, y, z).

and hence a particular composition. Three binary alloys $A_{1-x}B_xD$, $A_{1-z}C_zD$ and $B_{1-z}C_zD$ are given by the edges of the triangle while the pure compounds AD, BD and CD are shown at each corner. Therefore in any case, any two properties of the material can be controlled independently of each other. Also, any isothermal section of the three dimensional model is thus an equilateral triangle on which the phase equilibrium at that temperature can be depicted in two dimensions. In the diagram for the present system, the pseudo binary SMSC alloys $Zn_{1-z}Mn_zTe$ and $(CuIn)_{1-z}Mn_{2z}Te_2$ are represented by the left and right edges respectively while the bottom edge represents $Zn_{2x}(CuIn)_{1-x}Te_2$. The pure compounds which are MnTe, Zn Te and $CuInTe_2$ are shown at each corner of this equilateral triangle. For the remainder of this thesis, a sample with a particular composition will be referred to by a label of the form (x, y, z) where x, y and z are the percentages of Zn_2Te_2, $CuIn_2Te_2$ and Mn_2Te_2. Note also that any straight line from the corner where MnTe occurs, to the $Zn_{2x}(CuIn)_{1-x}Te_2$ edge represents a particular y:x composition ratio.

The measurements described in this thesis are as follows. Chapter 2 deals with the production of alloys and the variation of the lattice parameter with the composition to find the limit of solid solution. First, the method of preparation of samples followed by the introduction and description of the two structures zinc blende and chalcopyrite is given. The next section is concerned with the x-ray analysis of the samples which allows us to determine the range of solid solution. The main feature in the calculations of accurate lattice parameter values by x-ray photographs is indicated.

Chapter 3 gives the study of the variation of the energy gap with the composition for both zinc blende and chalcopyrite materials by optical absorption. First, a brief introduction with the theory is presented and the experimental details of the preparation of samples for absorption measurements is discussed. In addition to these results, the values of energy gap

provide useful information about ordering in the lattice.

The main aim of the work described in chapter 4 is to investigate the magnetic properties of the samples. In this chapter, low field measurements of magnetic susceptibility will be studied as a function of temperature in the range 4.2 to 250K on all the samples in single phase regions. Values of the spin glass temperature T_g and Curie Weiss temperature θ are presented. The values of T_g are initially analysed in terms of an equation proposed by Escorne et al.(9). Finally interesting information about the exchange interaction is obtained by using a modified Escorne type plot. For many samples, the susceptibility measurements give two transition temperatures, the lower one corresponding to a disordered structure and higher to an ordered structure. The variation of these transition temperatures with manganese composition gives two different lines for the ordered and disordered cases for both zinc blende and chalcopyrite structures.

The last chapter deals with some ESR measurements on these samples. In this case, ESR measurements made on the manganese constituent of $Zn_{2x}(CuIn)_yMn_{2z}Te_2$ covering the whole range of solid solution will be discussed. The measurements were made as function of temperature below 300K. The results will be discussed qualititatively since the form of the results was complicated by the occurrence of both ordered and disordered phases in the same sample. As a result, it was not possible to investigate the variation of ESR linewidth with temperature. Finally, an overall discussion of all the measurements will be given in chapter 6.

To carry out the measurements listed above, a large number of samples of different compositions were required. Polycrystalline samples were used because it would take a very long time to prepare so many single crystal samples. Previously, comparison of the results obtained from polycrystalline samples with those obtained from single crystals showed that there was no significant difference in the case of measurements of the type made here. The work discussed in this thesis is part of a larger research programme involving a range of

alloy systems including

$$Cd_xZn_yMn_zTe_2 \qquad (10)$$

$$Cd_{2x}(CuIn)_yMn_{2z}Te_2 \qquad (11)$$

$$Cd_{2x}(CuGa))_yMn_{2z}Te_2 \qquad (12)$$

$$Cd_{2x}(AgIn)_yMn_{2z}Te_2 \qquad (13)$$

$$Cd_xZn_yMn_zSe_2 \qquad (14)$$

To discuss some of the measurements described in this thesis, it is often necessary to include results obtained by other members of the research group. Wherever this is done, appropriate reference is made at each point.

Chapter 2

Solid Solution and Lattice Parameter Values

2.1 Introduction

An alloy can be defined as a combination of two or more metals or of metals and non metals. Depending on the composition and temperature, a single phase or a mixture of phases can occur in the alloy at equilibrium and under a constant atmospheric pressure. In order to study any physical property of an alloy, it is necessary to determine the range of single phase solid solution and this certainly applies to our alloy system $Zn_{2x}(CuIn)_yMn_{2z}Te_2$. The boundary edges of the triangle $Zn_{1-z}Mn_zTe_2$ and $(CuIn)_{1-z}Mn_{2z}Te_2$ which as mentioned earlier in chapter 1 have been studied previously show a wide range of solid solution (10-11).

In the present alloy system, it is seen that two single phase regions occur, the zinc blende structure and also a small region of chalcopyrite structure. The isothermal section of the $Zn_{2x}(CuIn)_yMn_{2z}Te_2$ phase diagram obtained during the experimental studies of solid solubility is presented in this chapter as a function of the z and y variables.

2.2 Zinc blende and Chalcopyrite Crystal Structures

The crystal structure of zinc blende is derived from the tetrahedrally bonded diamond structure, Fig. (2.1 a). The Bravais lattice is f.c.c. The diamond structure may be viewed as two f.c c. structures displaced from each other by one quarter of a body diagonal. The cubic zinc sulfide (zinc blende) structure results when zinc atoms are placed on one f. c. c. sub-lattice and sulphur atoms placed on the other f.c.c. sub-lattice as in Fig. (2.1b). The conventional unit cell is a cube. Turning to the system with which we are

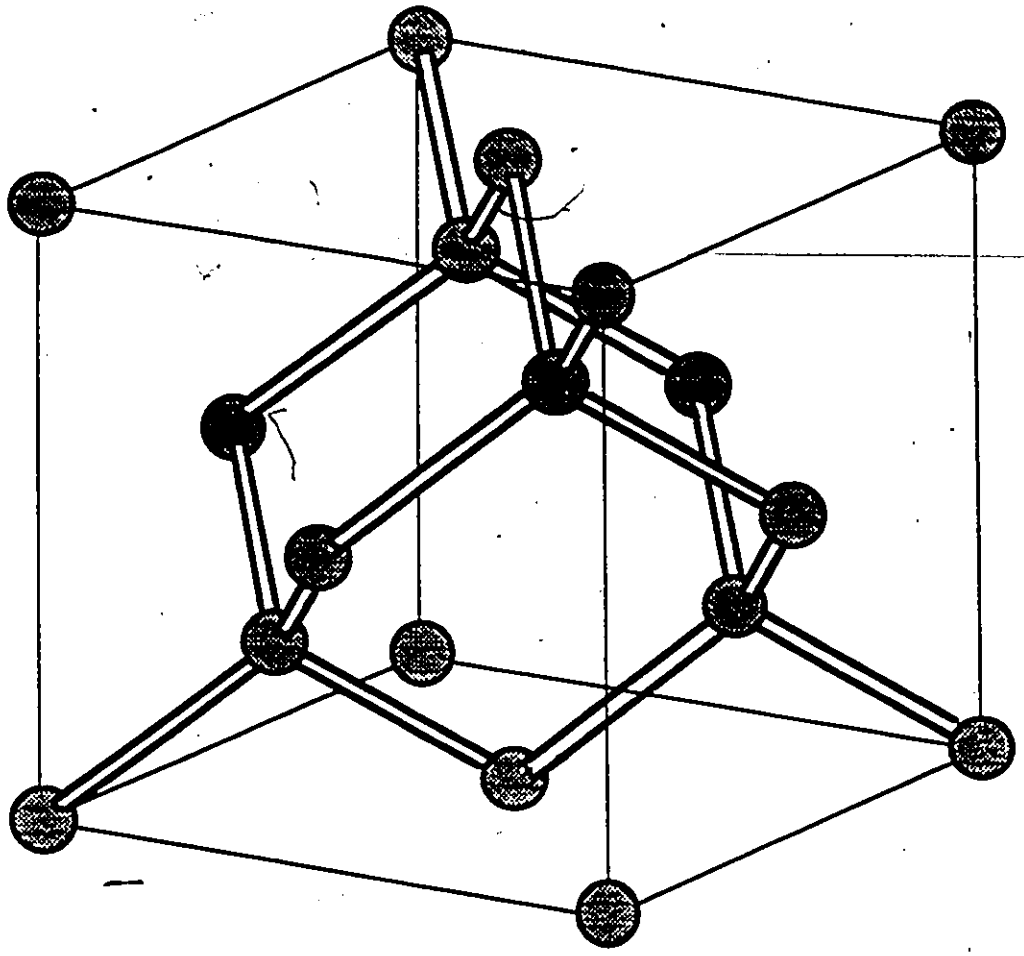

Fig (2.1a) Crystal Structure of Diamond

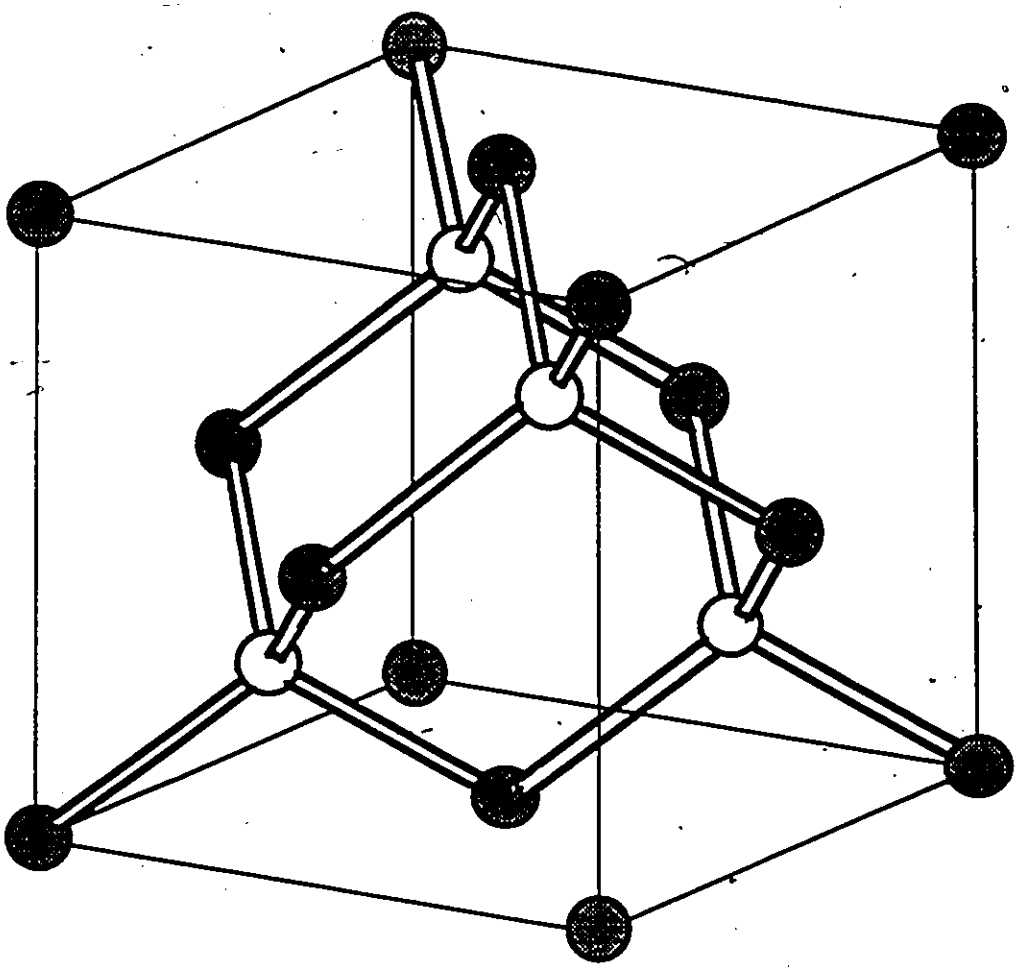

Fig (2.1b) Crystal Structure of Zinc Blende

dealing here, for the cubic alloys one of the f. c. c. sub-lattice is occupied by the cations and the other sub-lattice by the anions with an average of four valence electrons per site. The coordinates of the cations Zn, Cu, In and Mn are:

$$000,\ 0\frac{1}{2}\frac{1}{2},\ \frac{1}{2}0\frac{1}{2},\ \frac{1}{2}\frac{1}{2}0$$

The coordinates of the tellurium anions are:

$$\frac{1}{4}\frac{1}{4}\frac{1}{4},\ \frac{1}{4}\frac{3}{4}\frac{3}{4},\ \frac{3}{4}\frac{1}{4}\frac{3}{4},\ \frac{3}{4}\frac{3}{4}\frac{1}{4}$$

About each cation (anion) there are four equally distant anions (cations) at the corner of a regular tetrahedron. Another feature of these structures is that the diamond structure possesses a centre of inversion symmetry at the midpoint of each line connecting the nearest neighbour atoms while the zinc blende structure does not.

In the case of the I III IV_2 compounds and alloys, the structure is also adamantine. However, because of the ordering of the constituent cations, the symmetry of the unit cell does not remain the same. The materials have a body centered tetragonal structure with a ratio of $c/a \leq 2$. This structure is known as chalcopyrite and it is illustrated in Fig. 2.2. A few common examples of this structure are $CuFeS_2$, $CuInSe_2$, $CuInTe_2$ and $AgInTe_2$. The unit cell of chalcopyrite contains sixteen atoms as compared to eight for the zinc blende structure discussed above. In the chalcopyrite structure there are two cations sub-lattices, each occupied by one type of cation, and one anion sub-lattice. In the present system, each of Zn, Cu, In and Mn is tetrahedrally coordinated by four Te atoms while each Te atom is tetrahedrally coordinated by a mixture of cations as shown in Fig. 2.2 by the double lines. For $Zn_{2x}(CuIn)_yMn_{2z}Te_2$ the ratio of c/a for the chalcopyrite phase was found to be 2 in all cases.

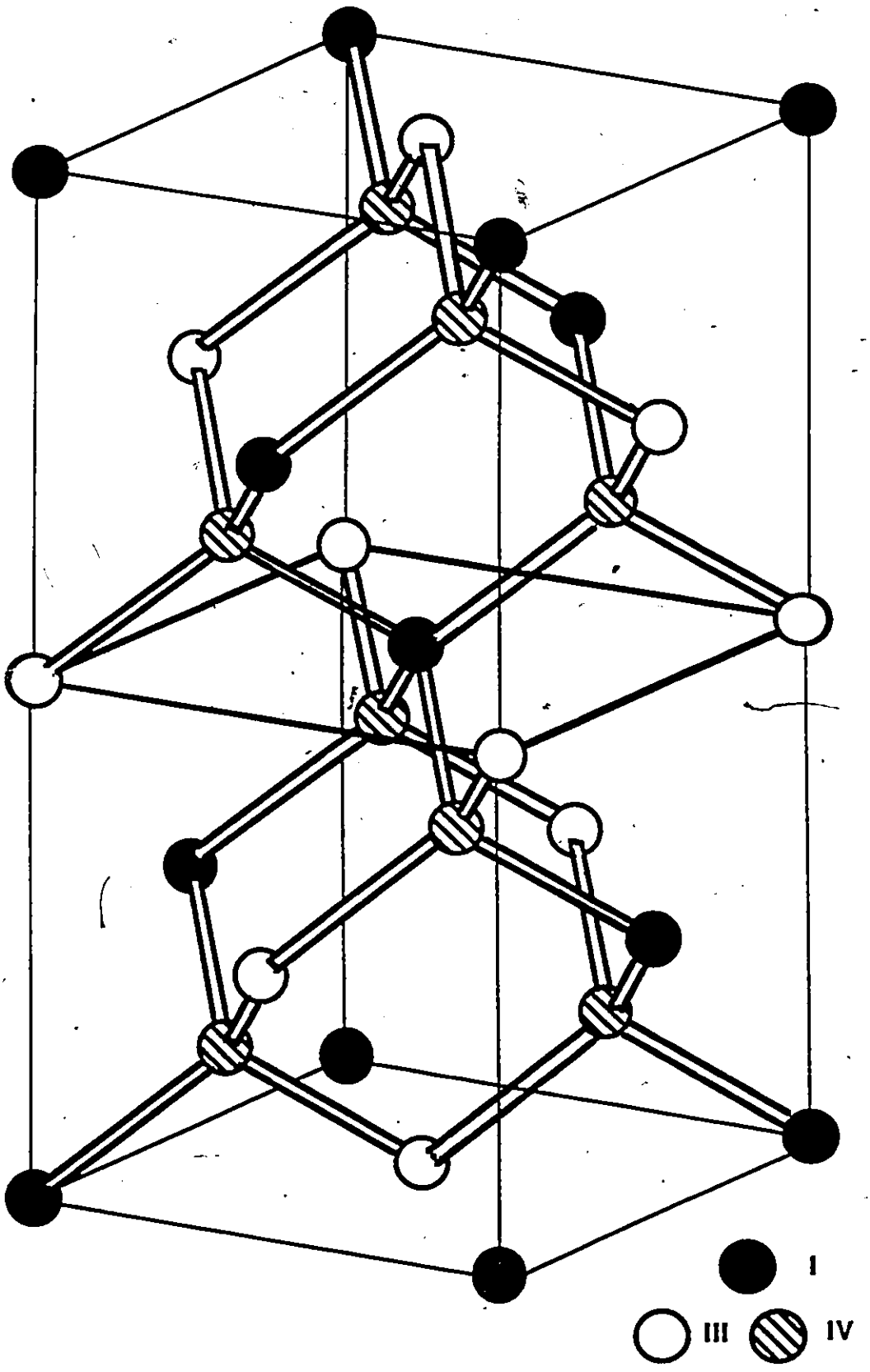

Fig (2.2) Crystal Structure of Chalcopyrite

2.3 Preparation of Samples

To study the various properties of interest in the present work, about sixty samples were made with different compositions using the melt and anneal method, the constituent elements being sealed under vacuum in small quartz tubes. Approximately one gram of each sample was made using appropriate weights of the elements in the alloy. The segments of quartz tubes used for these samples were about 5 - 6 cm long and had a diameter of 0.7 cm. It was found that some of the elements, particularly the manganese, react with quartz to some extent during the melting process. To prevent this, the interiors of the tubes were carbonized in the following way. First, one end of the ampoule was sealed. Then a piece of absorbent paper was soaked in acetone and placed in the open end of the ampoule. The sealed end was heated over an open flame. As soon as the concentration of acetone vapour was high enough, a layer of red hot carbon would start accumulating at the hot end of the tube. The heating process was continued until the carbon layer was thick enough to be opaque under a strong light.

Having been carbonized and filled with the required elements,the tubes were sealed under a vacuum of about 10^{-5} mm Hg. Then these ampoules were placed in a melting furnace and heated to 1150° C and kept at this temperature for 10 - 15 minutes. During this process the samples were shaken to make sure that the contents were mixed properly. The furnace was then switched off and the samples were left in the furnace to cool to room temperature. This procedure helped to avoid breakage of the quartz upon solidification of the alloy. Then the samples were transferred to an annealing furnace. The chosen annealing temperature depended on the melting points of compounds concerned and for the present system was 600° C for all but a few samples. The Debye-Scherrer x-ray powder photographs of these particular samples showed a blurring and faintness in the high angle

lines and it was found that to obtain a good equilibrium condition in the samples longer annealing times or annealing at higher temperature was needed. Therefore these particular samples were annealed at approximately 800° C. The samples were kept in the annealing furnace for 3 - 4 weeks and then the furnace was turned off and they were left to cool. This annealing process gave good solid samples which were used for the various measurements described below.

To determine lattice parameter values and the solid solution limits, Debye-Scherrer x-ray diffraction photographs were taken using CuK_α radiation. A schematic Debye-Scherrer camera is shown in Fig 2.3. It consists essentially of a cylindrical chamber with a light tight cover, a collimator to admit and define the incident radiation, a beam stop to confine and stop the transmitted beam, a means of holding the film tightly against the inside circumference of the camera, and a specimen holder that can be rotated. The powdered specimen was mounted on a thin glass fibre which was fixed to the specimen holder. Such a photograph was taken of each sample to determine the equilibrium conditions and the lattice parameter values for the zinc blende and/or chalcopyrite structures present, and hence to find the regions of single phase condition.

2.4 X - ray analysis

As mentioned in chapter one, the compositions to be investigated are shown in Fig (2.4). The lines were chosen as $x = y$, $x = 3y$, $x = 7y$ etc. so that the values could be easily compared. To calculate lattice parameter values the positions of the diffraction lines were measured using a travelling microscope and values of Bragg angle were calculated. It is known that the angle so obtained need not be the correct Bragg angle since the diffraction lines can be displaced from the true position due to various effects such as shrinkage of the film, absorption in the specimen etc. To eliminate these effects, two methods have been

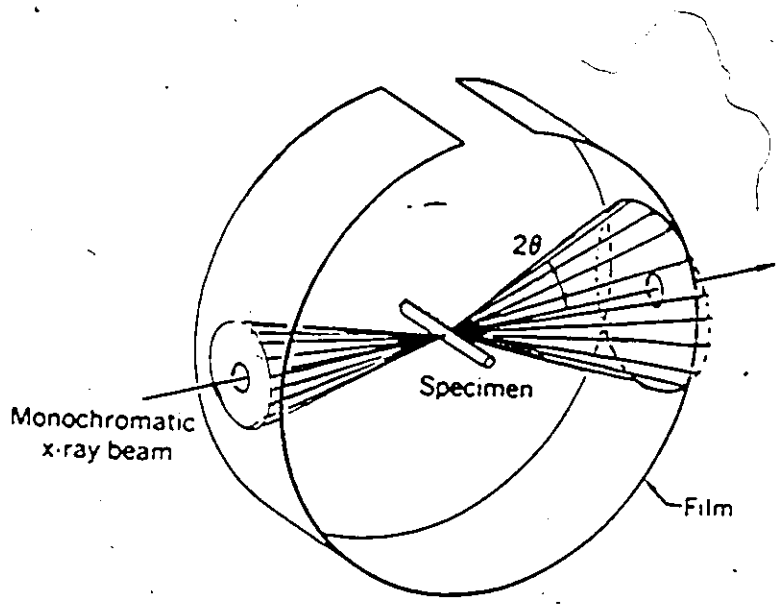

Fig (2.3) X-Ray Powder Diffraction Camera.

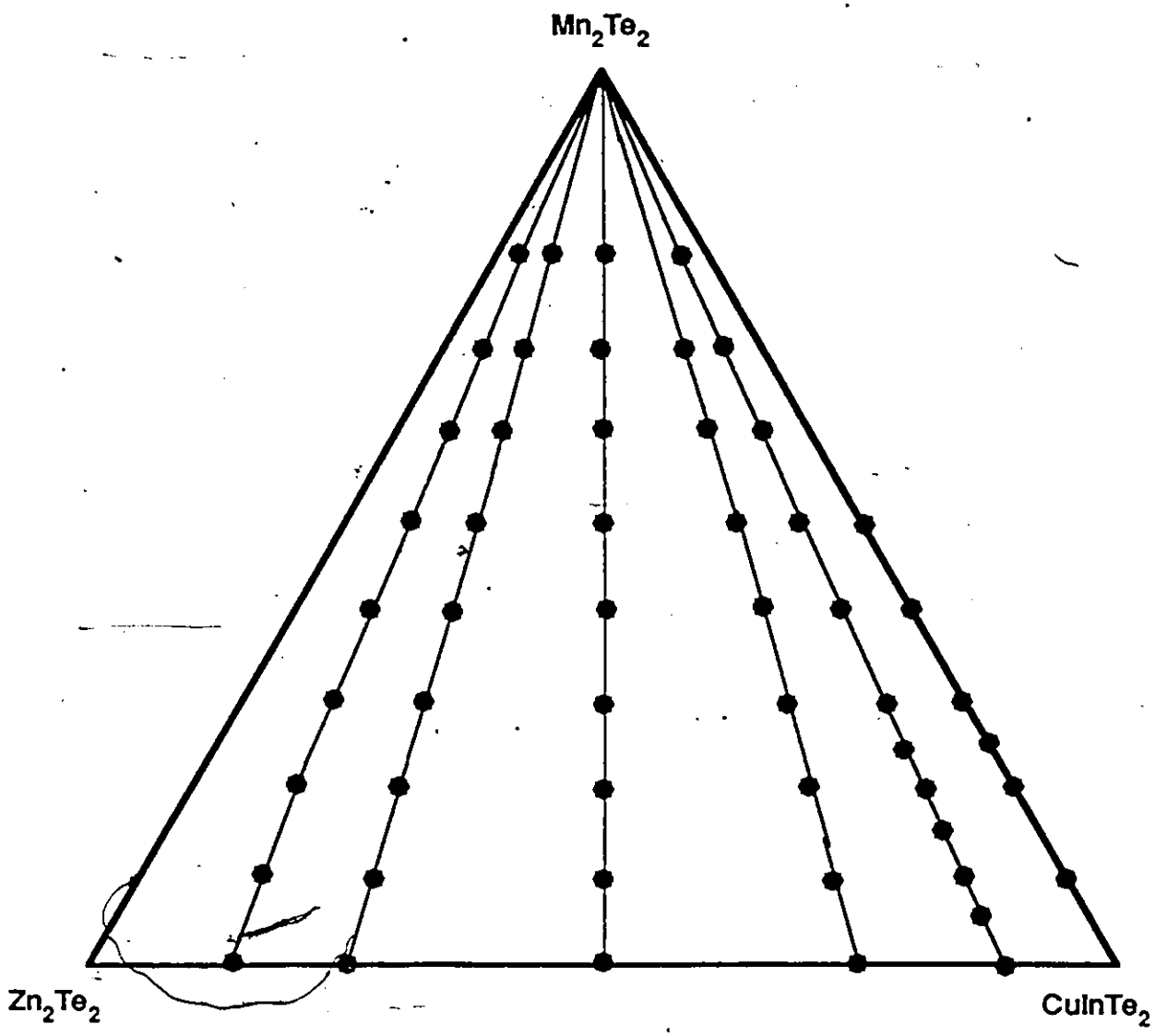

Fig (2.4) Samples studied by powder x-ray photographs.

used, the Nelson- Riley (15) extrapolation and the internal calibration technique. These two methods are described later in this chapter.

From the x-ray analysis, it was found that there were three different phase fields involved in the the system, Fig. (2.5). The region between the dashed curve and the solid curve represents a cubic single phase with zinc blende structure. The samples lying in the upper region of the triangle closest in composition to MnTe are two phases and contain zinc blende and hexagonal MnTe phases. The field between the solid line and the corner which represents $CuInTe_2$ was found to be single phase with chalcopyrite structure. A small number of two phase samples were measured to determine the single phase limits and all further measurements were made only on the single phase cubic and chalcopyrite samples.

2.5 Analysis for the cubic Zinc blende structure

Once the cubic powder pattern has been indexed, the lattice parameter *a*, can be determined by using the Bragg condition for diffraction and this is given for the cubic case by the expression:

$$a = \frac{\lambda}{2\sin\theta}\sqrt{h^2 + k^2 + l^2} \qquad (2.1)$$

where θ is the Bragg angle, λ is the wave length of the radiation, (hkl) are the Miller indices for individual scattering planes, and $N = h^2 + k^2 + l^2$ is an integer. In a simple cubic lattice, any possible set of hkl values can occur, while for f. c. c. lattices only certain N values are allowed. For an f. c. c. lattice, h, k, and l values should be either all even or all odd (16) for diffraction maxima to occur. Therefore the possible values of N in the zinc blende structure are 3, 4, 8, 11, 12, 16, 19, 20, 24, 27, 32, 35, 36, 40, 43, 44, 48, 51, 52, 56 and 59 etc. Also the indices satisfy the conditions

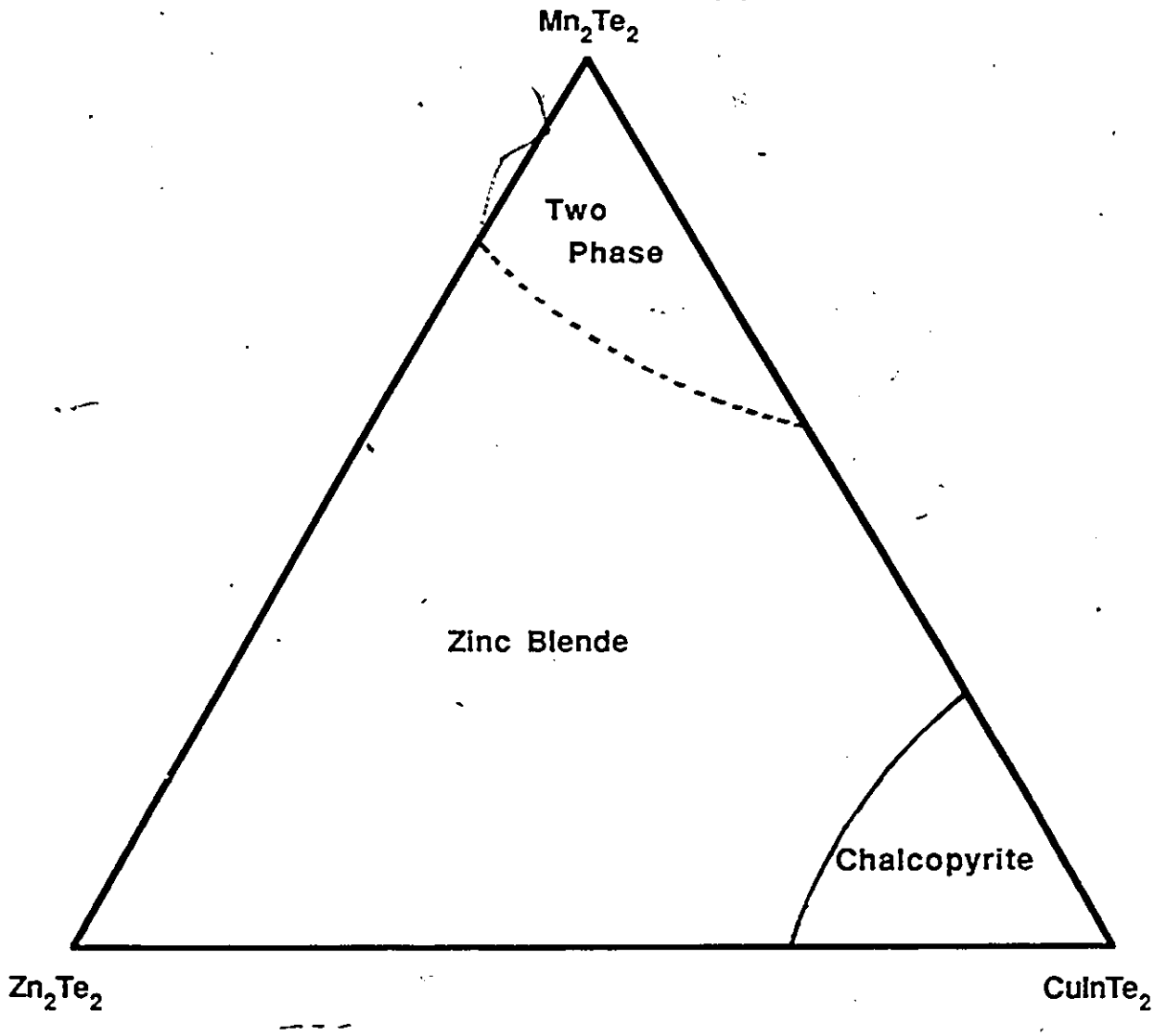

Fig (2.5) Illustration of the Three Different Phase Fields Involved in the System

$$h + k + l = 4n \qquad I \propto (F_{hkl})^2 = 16 (f_A + f_B)^2$$

$$h + k + l = 4n + 2 \qquad I \propto (F_{hkl})^2 = 16 (f_A - f_B)^2 \qquad (2.2)$$

$$h + k + l = 2n + 1 \qquad I \propto (F_{hkl})^2 = 16 (f_A^2 + f_B^2)$$

giving the strong and the weak lines where the intensity of line I is proportional to the square of the structure factor (F_{hkl}) and the atomic scattering factor f_A, f_B. For example, the strong and the weak lines can be written in the following way.

$h + k + l = 4n$	220	400	422	etc.	(strong)
$h + k + l = 4n + 2$	200	222	420	etc	(weak)
$h + k + l = 2n + 1$	111	311	331	etc	(strong)

where n is an integer.

It may be shown that the effect due to the absorption vanishes at $\theta = 90^0$. The procedure usually adopted for the cubic materials therefore, is to derive an apparent cell dimension *a*, for a number of lines on the photograph and plot these values against a suitable function of the Bragg angle θ to give a linear extrapolation to the value corresponding to $\theta = 90^0$. This is the Nelson - Riley method and the semi- empirical function used is

$$f(\theta) = \frac{1}{2} \{ \frac{\cos^2\theta}{\sin\theta} + \frac{\cos^2\theta}{-\theta} \} \qquad (2.3)$$

In any case, it must never be assumed that the process of extrapolation can automatically produce a precise value of lattice parameter from careless measurements made on film of

poor quality. For high precision, the high angle lines must be used and the lines must be sharp and the K_α doublet should be well resolved at high angles. In the present work, the wavelength used for all x-ray photographs was 0.15405 nm. In the case of the chalcopyrite materials, if c/a = 2 the photographs are very similar to the cubic case and with only one apparent parameter, the method describe above can still be used in the analysis. However, for samples with $c/a \neq 2$ it is difficult to use the Nelson - Riley method to determine two or more accurate parameter values. Thus another method is used, this being the internal calibration method. In this method, an internal standard sample with an accurately known parameter is mixed with the sample being investigated. Then values of Bragg angle for both materials are calculated. A correction curve $\Delta\sin^2\theta$ vs $\sin^2\theta$ to allow for absorption effects etc. is calculated from the data for the standard material. Hence the corrected values of $\sin^2\theta$ for the unknown sample are then obtained which allows accurate values for the lattice parameters to be calculated. In the present work only the Nelson - Riley method was used since for all of the chalcopyrite samples c/a = 2 and so the analysis was the same as for the cubic materials as indicated below.

2.6 Analysis for the chalcopyrite samples

The two structures of zinc blende and chalcopyrite are such that they have the same atomic positions. Therefore all the diffraction lines due to the zinc blende structure will occur in the x - ray films of the chalcopyrite samples. In addition to these zinc blende structure lines, a set of ordering lines corresponding to the chalcopyrite structure will occur. This can be discussed in the following way. For chalcopyrite materials which have the tetragonal structure, the Bragg condition is given by

$$\sin^2\theta = \frac{\lambda^2}{4}\left\{\frac{h^2+k^2}{a^2} + \frac{l_T^2}{c_T^2}\right\} \qquad (2.4)$$

If the same value of $\sin^2\theta$ is to be obtained for both the chalcopyrite and cubic structures when $c_T = 2c_c$, then we must have $l_T = 2l_c$. Thus lines which are labelled hkl_c in the cubic case will be $hk2l_c$ for the chalcopyrite case. i.e. the chalcopyrite photographs can be initially analysed with cubic hkl and then all l values doubled. If we consider a diffraction line which appears in both structures, for example N = 19, this corresponds to the 331 diffraction line for zinc blende and to the 332 line for chalcopyrite. For materials with $c/a \neq 2$ this line would split into two and the other set of hkl would be 316. Since the chalcopyrite samples in the present work was c/a = 2 only one line was obtained. If this method is used for the chalcopyrite ordered lines, it is found that half integral l_c values are obtained indicating that the l_T value is odd. For example, if an ordering line on the basis of a cubic analysis has a N value of 1.25, then it must have hkl_c values of 1 , 0, 1/2. The corresponding hkl_T values for the chalcopyrite structure are 1,0,1 obtained by doubling the l_c value. Table (2.1) illustrates the possible combinations of the values of hkl for both the zinc blende and chalcopyrite structures.

2.7 Results

The variation of lattice parameter values with manganese composition z is shown in Fig (2.6). Each line represents a different x : y ratio. It is seen that firstly, the cubic lines are straight within the limits of experimental error and secondly, all of the cubic lines can be extrapolated to a single point with a value of a = 0.634 nm at z = 1. This point

N	h k l	Zinc Blende h k l	Chalcopyrite h k l
1.25	1 0 1/2		1 1 1
3.0	1 1 1	1 1 1	1 1 2
3.25	1 0 3/2		1 0 3
4.0	2 0 0	2 0 0	2 0 0 0 0 4
5.25	2 1 1/2		2 1 1
7.25	2 1 3/2		2 1 3
	1 0 5/2		1 0 5
8.0	2 2 0	2 2 0	2 2 0 2 0 4
9.25	3 0 1/2		3 0 1
11.0	3 1 1	3 1 1	3 1 2 1 1 6
11.25	3 0 3/2		3 0 3
	2 1 5/2		2 1 5
12.0	2 2 2	2 2 2	2 2 4
13.25	3 2 1/2		3 2 1
	1 0 7/2		1 0 7
15.25	3 0 5/2		3 0 5
16.0	4 0 0	4 0 0	4 0 0 0 0 8
17.25	4 1 1/2		4 1 1
19.0	3 3 1	3 3 1	3 2 2 3 1 6
19.25	4 1 3/2		4 1 3
20.25	4 2 0	4 2 0	4 2 0 4 0 4
21.25	3 0 7/2		3 0 7
	1 0 9/2		1 0 9
23.25	4 1 5/2		4 1 5
24.0	4 2 2	4 2 2	4 2 4 2 2 8
25.25	2 1 9/2		2 1 9
27.0	3 3 3	3 3 0	3 3 6
	5 1 1	5 1 1	5 1 2 1 1 10
29.25	3 0 9/2		3 0 9
31.25	1 0 11/2		1 0 11
32.0	4 4 0	4 4 0	4 4 0 4 0 8
35.0	5 3 1	5 3 1	5 3 2 5 1 6 3 1 10
37.25	5 0 7/2		5 0 7
40.0	6 2 0	6 2 0	6 2 0 6 0 4 2 0 12
43.0	5 3 3	5 3 3	5 3 6 3 3 10
44.0	6 2 2	6 2 2	6 2 4 2 2 12
45.25	3 2 7/2		3 2 7
48.0	4 4 4	4 4 4	4 4 8
49.25	5 2 9/2		5 2 9
51.0	5 5 1	5 5 1	5 5 2 5 1 10
	7 1 1	7 1 1	7 1 2 14 1 1
53.25	3 2 11/2		3 2 11
56.0	6 4 2	6 4 2	6 4 4 6 2 8 4 2 12
57.25	1 0 15/2		1 0 15
59.0	5 5 3	5 5 3	5 5 6 5 3 10
	7 3 1	7 3 1	7 3 2 7 1 6 3 1 14

Table (2.1) Possible combinations of hkl values for zinc blende and chalcopyrite.

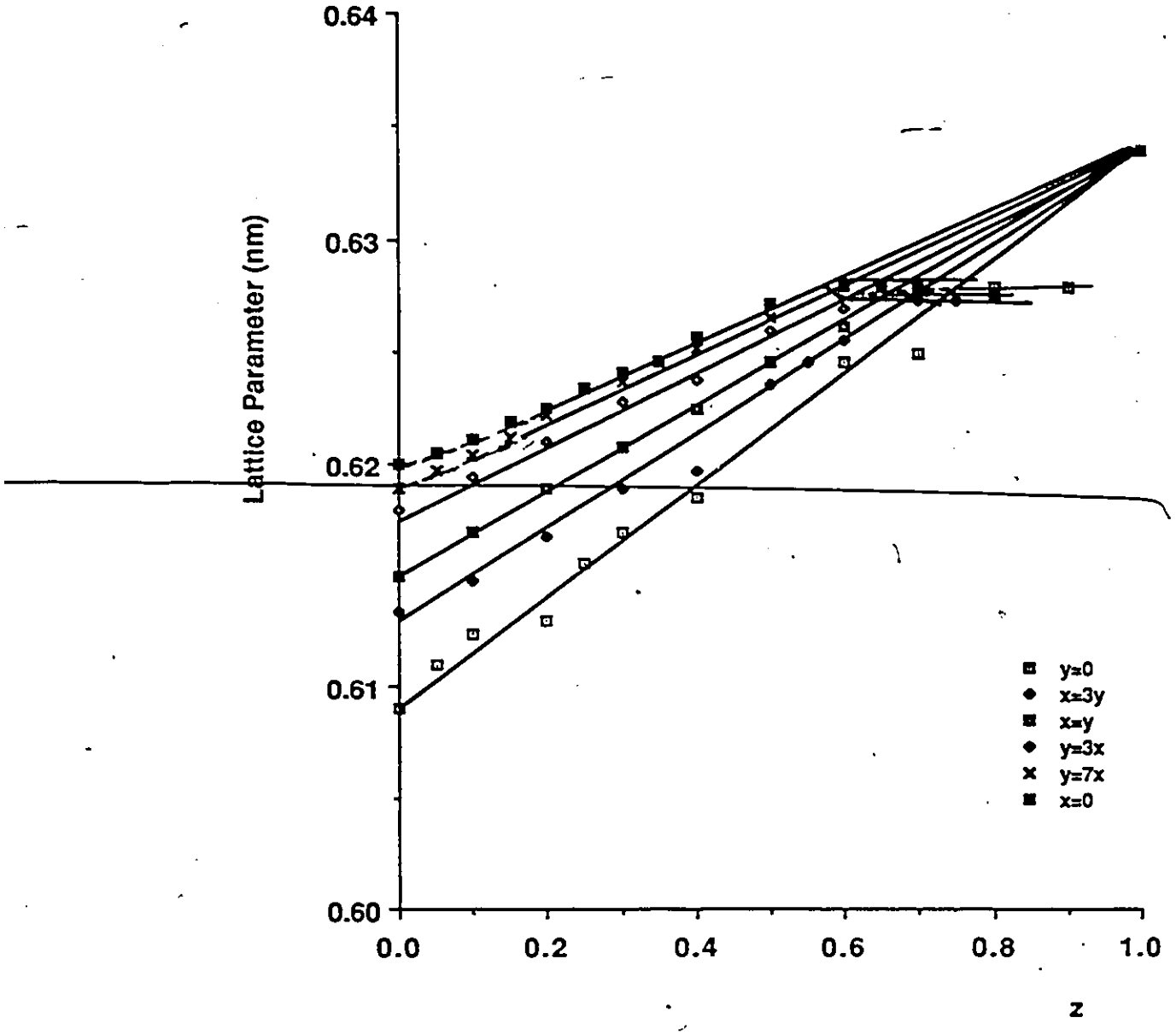

Fig (2.6) The variation of lattice parameter with z for different x:y.

specifically indicates the lattice parameter that MnTe would have in the zinc blende form. The limits of solid solution for the x = 0 edge andthe y = 0 edge occur at z = 0.76 and z=0.56 respectively (10-11). This is represented by the sudden leveling off of the a vs z graph at the phase boundary lines drawn in Fig (2.6). The same behavior occurs for the other lines in the diagram. Since the composition of the zinc blende phase remains constant for a particular x : y ratio, the value of the lattice parameter will remain constant and equal to the lattice parameter of the last single phase material on that line. Therefore, by measuring the lattice parameters of the zinc blende phase of various samples, one can determine the position of the horizontal lines in Fig (2.6). Thus this will give the position of the limit between thesingle phase and two phase regions by extrapolating back to intersect with the original fitted lines. The boundary is illustrated in Fig (2.6) by the dotted curve crossing the intersections of the fitted lines and the horizontal lines. Lattice parameter values for the samples having the chalcopyrite structure did not lie on a straight line against z. Those chalcopyrite samples are shown by dashed lines in Fig (2.6).

Fig (2.7) illustrates the variation of lattice parameter values with y for various values of constant manganese concentration, z. It is seen that in the cubic field these lines are parallel. The chalcopyrite field in the system is represented by the region enclosed by dotted lines. The line which was drawn intersecting all the lines at the points where x = 0 was extrapolated to y = 0 to obtain the lattice parameter of hypothetical zinc blende MnTe structure with a value of 0.634 nm as mentioned earlier. The lattice parameter value of $CuInTe_2$ is given by the point at y = 1 and the value is 0.621 nm. These values agree with the previous results (10-11) within the experimental limits.

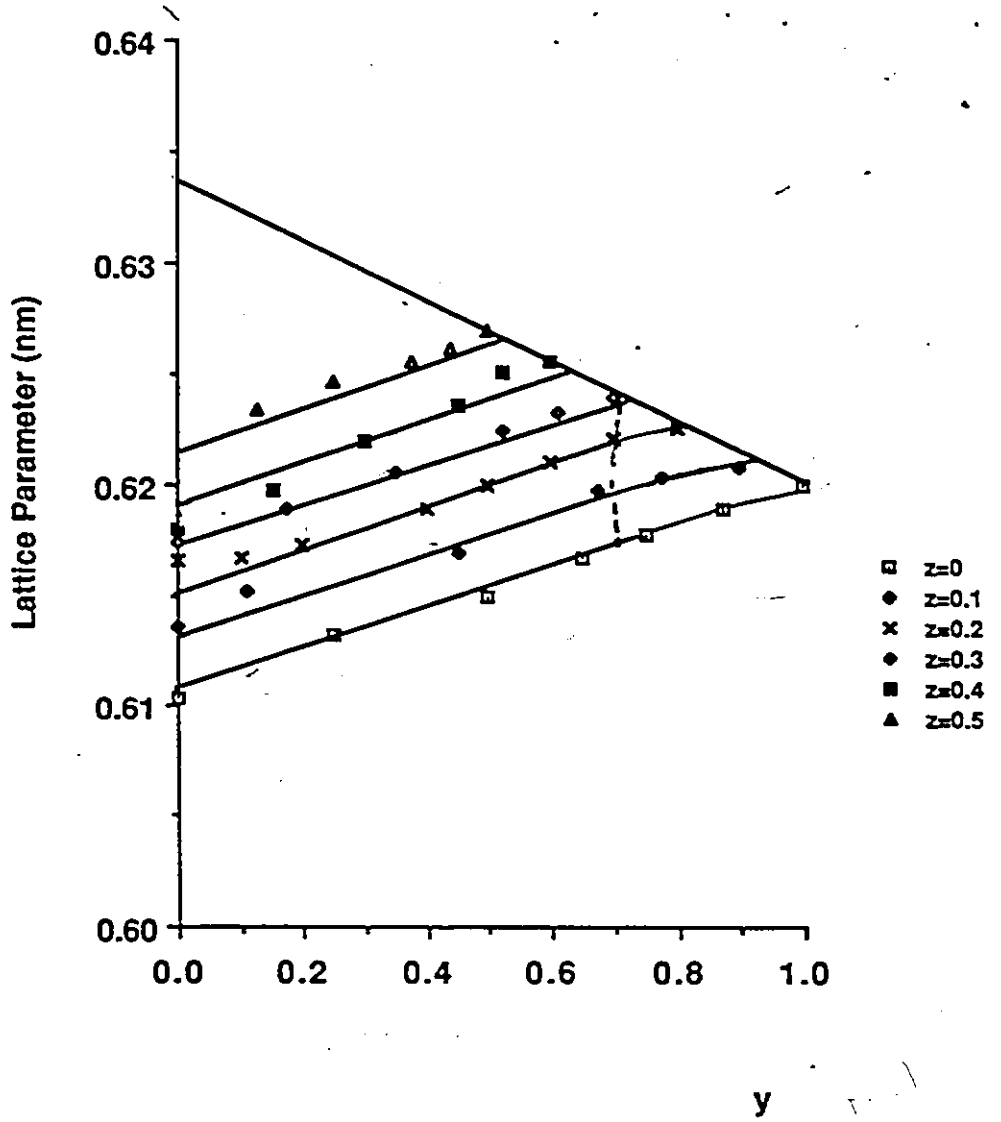

Fig (2.7) The variation of lattice parameter with y for constant z.

2.8 Calculation of constant lattice parameter contours

Having studied how the lattice parameters vary with the concentration z and y, it may be very useful to find a mathematical expression which represents the variation of the lattice parameter with composition. One advantage of doing this is for predicting values of the lattice parameter for intermediate compositions. Since the various graphs plotted have shown that the lattice parameter varies linearly with composition (except for the chalcopyrite samples), a general power series, considering only linear terms can be used to represent the variation of lattice parameter with composition in the cubic range. In this work the following convention was adopted. From Fig (2.6) and Fig (2.7), it is clear that the lattice parameter values show a linear variation with z and y and this can be given by

$$a(z, y) = A + By + Cz \qquad (2.6)$$

To predict lattice parameter values for general alloy composition, Williams et al. (17) proposed a method using an interpolation formula. Using the nomenclature of Williams et al, let a parameter Q have values of B_1, B_2 and B_3 for the compounds at the corners of the triangle and then the values along each edge may be written as $T_{ij}(x)$ where

$$T_{ij}(x) = xB_j + (1-x)B_i - x(1-x)C_{ij} \qquad (2.7)$$

where $i = 1,2,3$ and $j = 1,2,3$ with $i \neq j$

For any point in the pseudoternary system the value of Q may be written as

$$Q(x, y, z) = \frac{xy\,T_{12}(u) + yz\,T_{23}(v) + zx\,T_{31}(w)}{xy + yz + zx} \qquad (2.8)$$

where u , v and w are given by

$$u = \frac{(1 - x + y)}{2}, \quad v = \frac{(1 - y + z)}{2}, \quad w = \frac{(1 - z + x)}{2}$$

For the case of the lattice parameter value a , a linear variation is observed along the edges so that all C_{ij} 's are zero. Under this condition eq.(2.8) reduces to the equation (2.6) with

$$B_1 = A, \qquad B_2 = A + B, \qquad B_3 = A + C \qquad (2.10)$$

A least square fit of the experimental values to equation (2.6) gives the relation

$$a = 0.6102 + 0.0097y + 0.0227z \text{ nm} \qquad (2.11)$$

with a standard deviation of $\sigma = 0.0014$ nm. The constant lattice parameter contours obtained by numerical solution of eq. (2.11) are presented in Fig (2.8).

2.9 Discussion

The variation of the lattice parameters with composition is typical of all alloys of this pseudoternary type so far investigated (10-11). The limits of single phase cubic and chalcopyrite solid solutions were determined by x-ray diffraction. It is seen that the variation of lattice parameter with composition is linear in the cubic field but for the chalcopyrite phase the variation appears to be non-linear. This latter effect may be due to non- stoichiometry in the chalcopyrite materials (18).

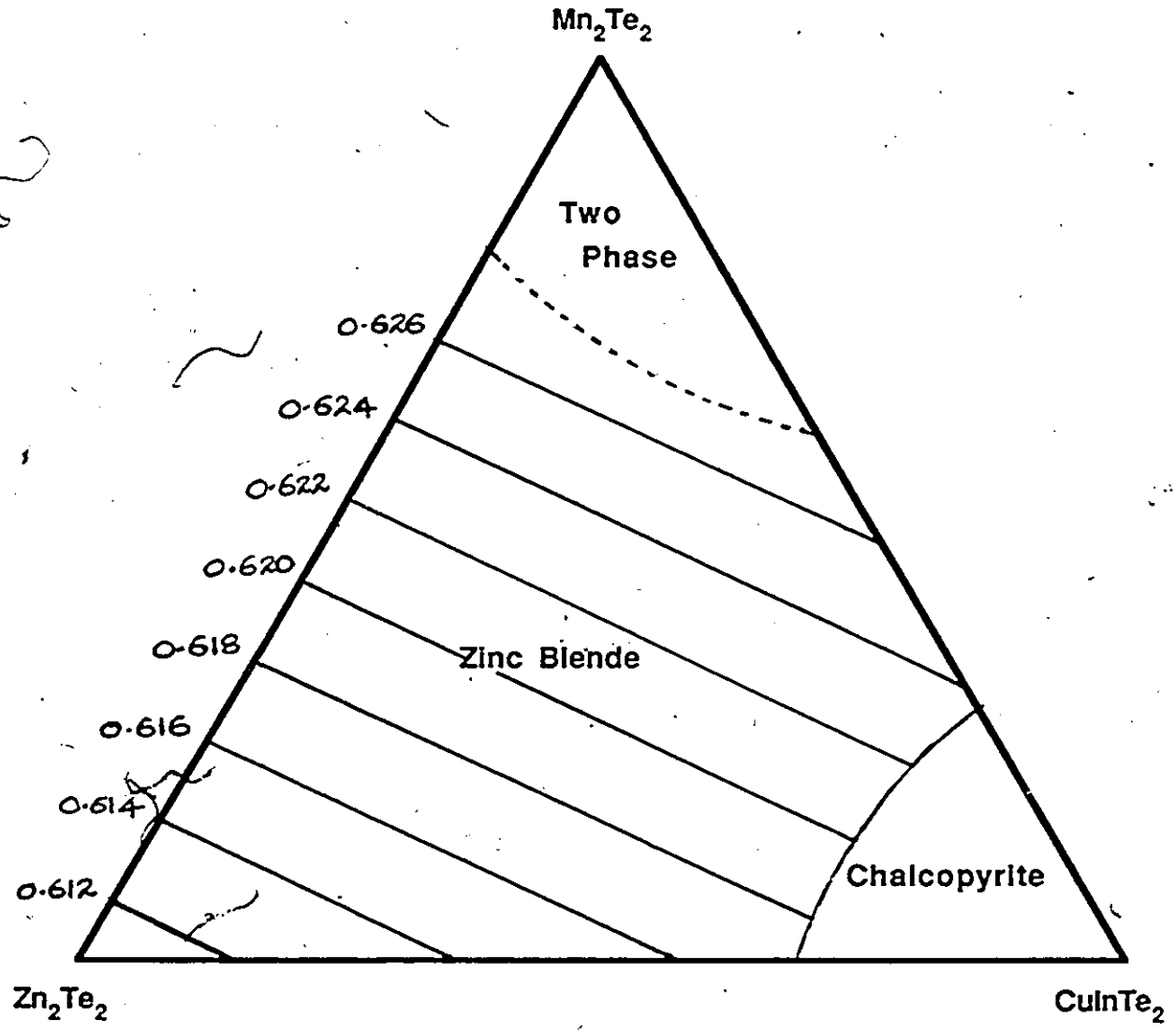

Fig (2.8) Values of Constant Lattice Parameter
The values indicated are in units of nanometers

Results from other diagrams (11-13) and measurements of magnetic susceptibility and ESR indicate that ordering of Mn atoms can occur in parts of the cubic and chalcopyrite single phase fields. However the variation of lattice parameter with composition gives a smooth curve across the complete range and hence the limits of the ordered field can not be determined from the variation of the lattice parameter values. The range of the ordered solid solution has been found from optical measurements and will be discussed in the next chapter.

For the two phase samples, the x-ray photographs show lines which correspond to the hexagonal structure of MnTe. This was confirmed by comparing these films with a x-ray film of MnTe. In order to use the variation of lattice parameter to determine the phase boundaries, as mentioned earlier it is important to remember that in a single phase region the lattice parameter changes smoothly and continuously with composition. In a two phase region one can always find " tie " lines along which the relative amounts of two phase changes but the composition and hence lattice parameter values remain constant. As mentioned at the beginning of this chapter the edges $x = 0$ and $y = 0$ which belong to $Zn_{1-z}Mn_zTe$ (10) and $(CuIn)_{1-z}Mn_{2z}Te_2$ (11) have been studied previously and the present results agree with the limits of solid solution for those systems as well as with the values of lattice parameter. Finally the variation of lattice parameter with composition was fitted to a suitable empirical equation and the accuracy of fitting was better than the average experimental uncertainty and from the fitted parameters contours of constant lattice parameter were drawn.

With regard to the accuracy of the various points in the lattice parameter vs composition curves, the expected accuracy in a depends upon the sharpness of the lines in the x-ray photographs and should be in the range $\pm$ 0.005 to $\pm$ 0.01 A. However the experimental scatter of the points is greater than this and the main limit of accuracy is in the values of the composition. The variation in this case has not been directly determined. But from the graphs on page 22, the error in z could be as much as $\pm$ 0.02.

Chapter 3

Optical Measurements

3.1 Introduction

Having established the phase diagram of $Zn_{2x}(CuIn)_yMn_{2z}Te_2$, other important properties of these materials can be investigated in the single phase regions. The determination of the optical constants of a semiconductor can provide a wealth of information about their band structure. It has been suggested by various people (1-6) that the energy band structure may be affected by a number of influences such as temperature and magnetic field as well as by intrinsic effects such as the magnetic ion concentration. Therefore, one can obtain a range of possible energy gap values for a given system by varying the above properties.

The optical measurements of semimagnetic semiconductors are powerful tools for studying the energy band structure of solids, specifically the energy difference between the top of the valence band and the bottom of the conduction band (energy gap). A common way of observing the energy gap is by determining the absorption by transmission measurements and this is the procedure used in this work. Since E_g is the minimum energy for the transition of an electron from the valence band into the conduction band, the absorption spectrum is characterized by a strong increase in the absorption coefficient at $E_g=h\upsilon$. The shape of the absorption edge is determined by the nature of the optical transition between the upper edge of the valence band and lower edge of the conduction band. In other words, the measurements of the fundamental absorption edge yield the nature (direct, indirect, allowed, forbidden) of the transition involved. If both band extrema lie at the same point in the Brillouin zone, direct transitions are possible. These can be separated into "allowed and forbidden " transitions depending upon the type of wave function involved. One simple example of allowed transitions takes place, for example, if

the valence band wave function is derived from p states of the individual atoms, and the conduction band function from s states. If the former were derived for example, from d states then since d-->s is a forbidden atomic transition, this would be considered a forbidden transition which can be seen in solids. When the band extrema lie at different k values, only indirect transitions with phonon participation are possible. The transitions responsible for this process cannot be a one step photon absorption process because the photon has insufficient momentum. Since momentum would not be conserved, the change in the momentum of the electron has to be taken up by a phonon which is either absorbed or emitted. In direct transitions the absorption edge is characterized by a very steep behavior while in indirect transitions, the absorption curve is much more shallow.

Another method of studying the energy gap is by reflection measurements. This can be very useful especially where transmission measurements are impossible due to the excessive background absorption. However, in the present work, all the direct energy gaps were measured using the absorption technique.

3.2 Theory of Optical Absorption

Experimentally, one can observe the intensity of the wave reflected from the surface of the sample and/or the intensity of the wave transmitted through the sample. When a beam of light of intensity I_o is incident normally on the surface of a sample of thickness d, a portion I_R is reflected and a portion I_T transmitted. Considering the transmission intensity for experimental conditions such that interference effects due to internal reflection are negligible, (which is the case in the present work because of the thickness of the sample) the transmission can be expressed by

$$T = \frac{I_T}{I_O} = \frac{(1 - R^2)\left(1 + \frac{k^2}{n^2}\right)\exp(-\alpha d)}{1 - R^2 \exp(-2\alpha d)} \qquad (3.1)$$

where R is the reflection coefficient and n and k are the refractive index and the extinction coefficient of the material respectively. Since k is much less than n near the absorption edge and the value $R^2 \exp(-2\alpha d)$ much smaller than 1 in the cases considered here, a simple expression for the transmitted intensity can be obtained as

$$I_T = I_O(1 - R^2)\exp(-\alpha d) \qquad (3.2)$$

Generally, the reflectivity varies slowly with photon energy and one may consider $(1 - R^2)$ as a constant over the energy range of the absorption edge. Therefore the ratio I_O / I_T which depends only on α and d can be given in logarithmic form as

$$\ln \frac{I_O}{I_T} = \alpha d - \text{constant} \qquad (3.3)$$

The theory of interband optical absorption (19) shows that for a direct allowed transition, the absorption coefficient varies with the photon energy $h\upsilon$ according to the equation

$$\alpha h\upsilon = A[h\upsilon - E_g]^{1/2} \qquad (3.4)$$

The corresponding result for a forbidden transition is

$$\alpha h\upsilon = B[h\upsilon - E_g]^{1/3} \qquad (3.5)$$

When the transition is indirect allowed, eq (3.4) becomes

$$\alpha h\upsilon = C [h\upsilon - E_g]^2 \qquad (3.6)$$

where A , B and C are slowly varying functions of the energy and $h\upsilon$ is the photon energy. When the transition is direct allowed, the usual method of determining the value of E_g involves plotting a graph of $(\alpha h\upsilon)^2$ against $h\upsilon$.

3.3 Experimental Procedure

The samples prepared by the melt and anneal process described in chapter 2 were used for these measurements. For the absorption work, the samples were cut into thin discs about 1mm thick using a carborundum wheel. These discs were polished by the following method. First, a disc was mounted on a brass rod using molten paraffin wax as the adhesive. When the wax had cooled down and was hard enough to hold the sample tightly, the sample was polished on a rotating wheel with appropriate polishing powder and water. Care was taken not to break the sample during the process by putting little pressure on the rod and rotating it slowly. When the thickness had been reduced to about 100μm - 150μm the sample was removed from the brass rod by dissolving the wax in hot acetone. The polished surface was then etched in a solution of 99% pure methanol with 3% bromine by rubbing the sample on absorbent paper saturated with the solution until a good polished surface was obtained. Care had to be taken so as not to break the sample during this process which involved 2 - 3 minutes of the etching procedure. The sample was then ready for the absorption measurements and it was mounted on a brass plate which had been suitably drilled so that the polished sample completely covered the drilled hole.

Fig. (3.1) shows the experimental set up for the absorption measurements. In this experiment, a 30w tungsten ribbon lamp was used as the light source. A chopper was placed at the entrance slit of the monochromater, a Spex 1720 with interchangeble gratings for the various wavelength ranges investigated. The light from the source was chopped at about 885 Hz. The brass plate with the sample was placed immediately in front of the detector so that when the monochromatic light from the exit slit was focussed on to the sample, all of the transmitted light would fall on the sensitive area. In general, a Dumont 6911 or an EMI 6255 photomultiplier was used as a detector. The output from the photomultiplier was connected to a PAR 186 A lock-in amplifier, the sensitivity of which was adjusted according to the intensity of the transmitted light. Some of the samples had sufficiently low energy gap values that wavelengths beyond the long wave limit of the photomultiplier had to be used. In those cases, a biased PbS cell was used as the detector with a PAR 113 roll - off amplifier before the lock - in amplifier, since the signal from the PbS cell was small. In all cases, the wavelength of the incident light was continuously varied and the output from the lock-in was traced on a pen recorder.

3.4 Results

In order to obtain the absorption coefficient from eq.(3.3), the constant had to be determined. Dividing eq.(3.3) by the thickness of the sample d gives

$$\frac{1}{d}\ln\frac{I_O}{I_T} = \alpha - \frac{1}{d}\,\text{constant} \qquad (3.7)$$

In addition to the constant term in eq.(3.4), there will be background absorption due to scattering effects etc. which must also be allowed for. A typical curve of $1/d\ln I_O/I_T$ vs $h\upsilon$ is shown in fig. (3.2) for the sample with $y = 0.25$, $z = 0.5$ measured at 300K. The

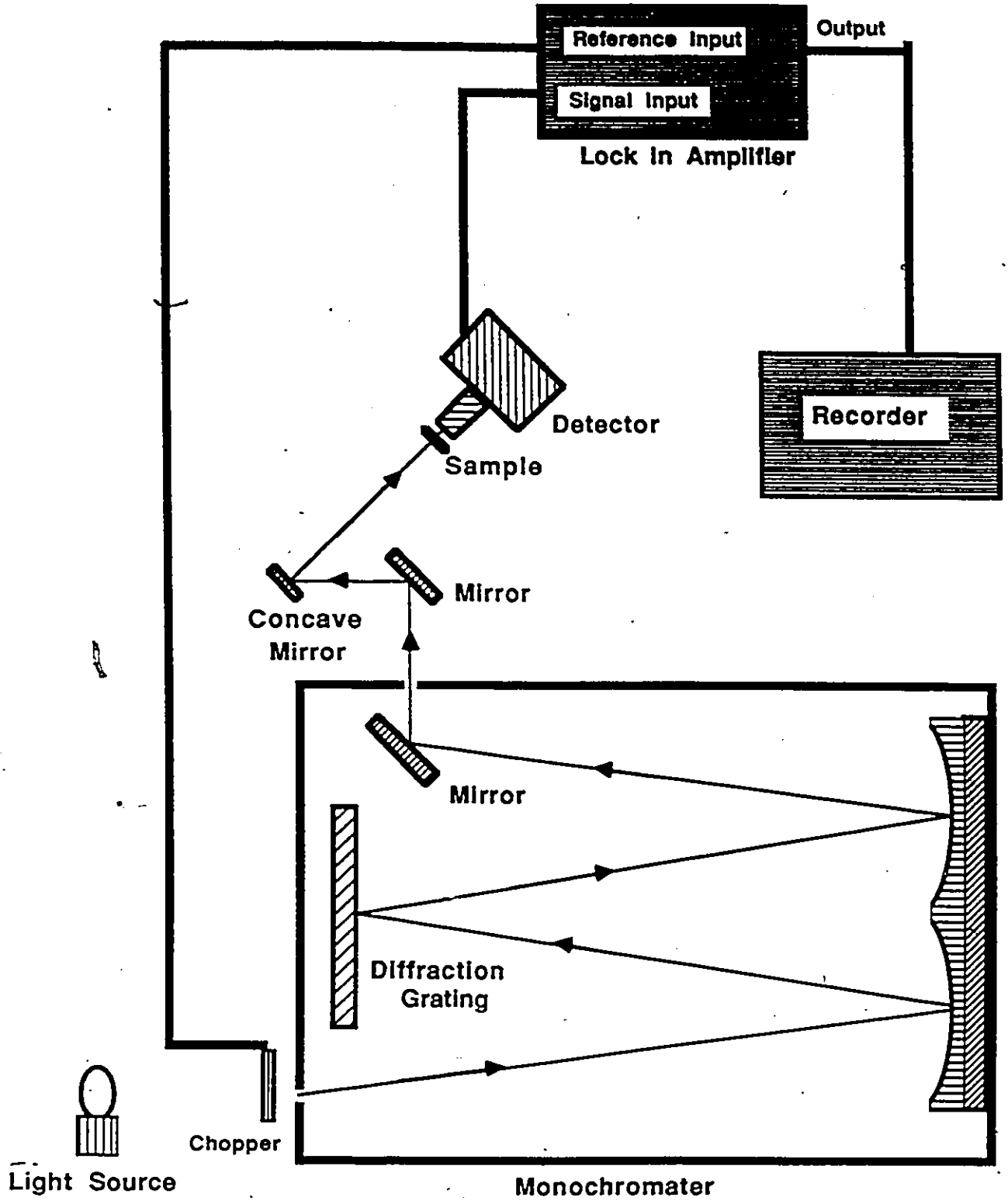

Fig (3.1) Block Diagram of the Optical Experimental Set Up Used in the Absorption Measurements

required value of α can be obtained by subtracting from the measured values of $1/d\ln I_O/I_T$ background values obtained by extrapolation from the region of the curve well away from the edge. It was found that in all cases a linear extrapolation was sufficient for this purpose.

The resulting values of α vs $h\upsilon$ are shown in Fig. (3.2). With regard to the semimagnetic alloys, since both absorption and reflection measurements have previously shown (18) that the transition is direct, equation (3.4) was used for the analysis of the absorption data. Having obtained the value of α, a second graph $(\alpha h\upsilon)^2$ vs $h\upsilon$ was plotted. Fig. (3.3) and Fig. (3.4) represent the variation of $(\alpha h\upsilon)^2$ vs $h\upsilon$ for x=0.175, y=0.525, z=0.3 and x=0.45, y=0.45, z=0.1. The energy gap was given by the intercept on the $h\upsilon$ axis. The intercept can be obtained by extrapolating the straight part of graph to the $h\upsilon$ axis as indicated in Fig. (3.3) and Fig. (3.4). It can be seen that the curves show appreciable deviation from linearity at low values of $(\alpha h\upsilon)^2$ due to some tailing effects. Possible effects include tailing due to random cation arrangement (20) transitions involving optical phonons occurring below the direct gap value (19-20), or effects of large impurity concentrations. The range of α over which measurements could be made was limited because with the polycrystalline material used, it was not possible to polish samples down below a certain thickness before they disintegrated. However, at all compositions samples were prepared which allowed a sufficient part of the linear region of the $(\alpha h\upsilon)^2$ vs $h\upsilon$ line to be drawn and so reasonably accurate values of E_g could be obtained.

The variation of E_g with z for various lines of constant $f = y/(x + y)$ is shown

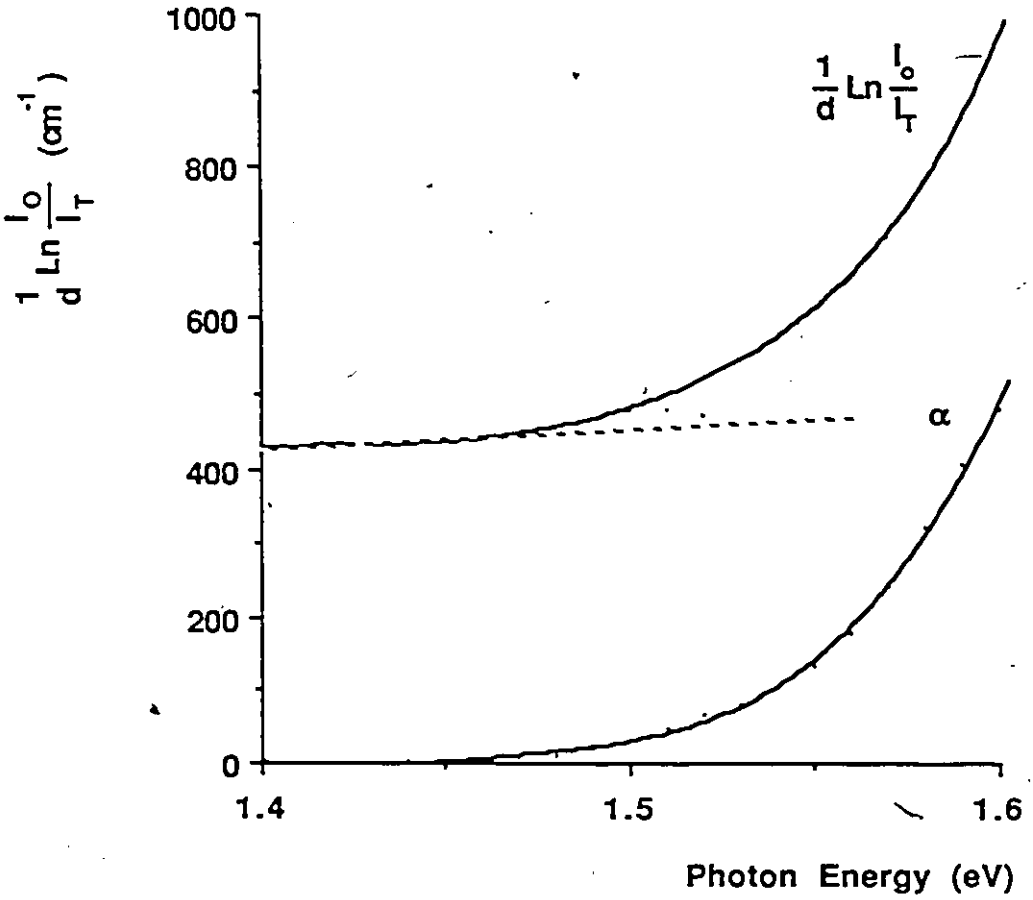

Fig (3.2) $\frac{1}{d} Ln \frac{I_o}{I_T}$ vs Energy for the Sample x=y, z=0.5
A straight line extrapolation of the background, dashed line, was subtracted from the experimental values to give absorption coefficient α

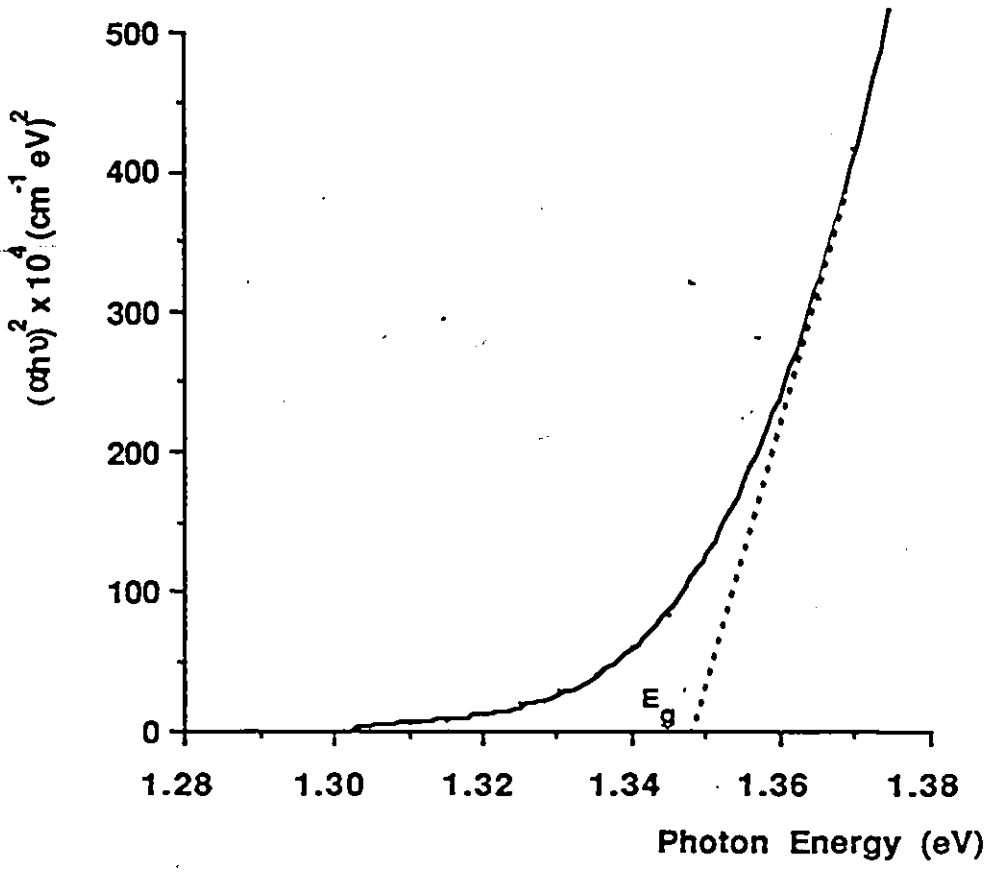

Fig (3.3) Variation of $(\alpha h\upsilon)^2$ with energy for x=3y, z=0.3

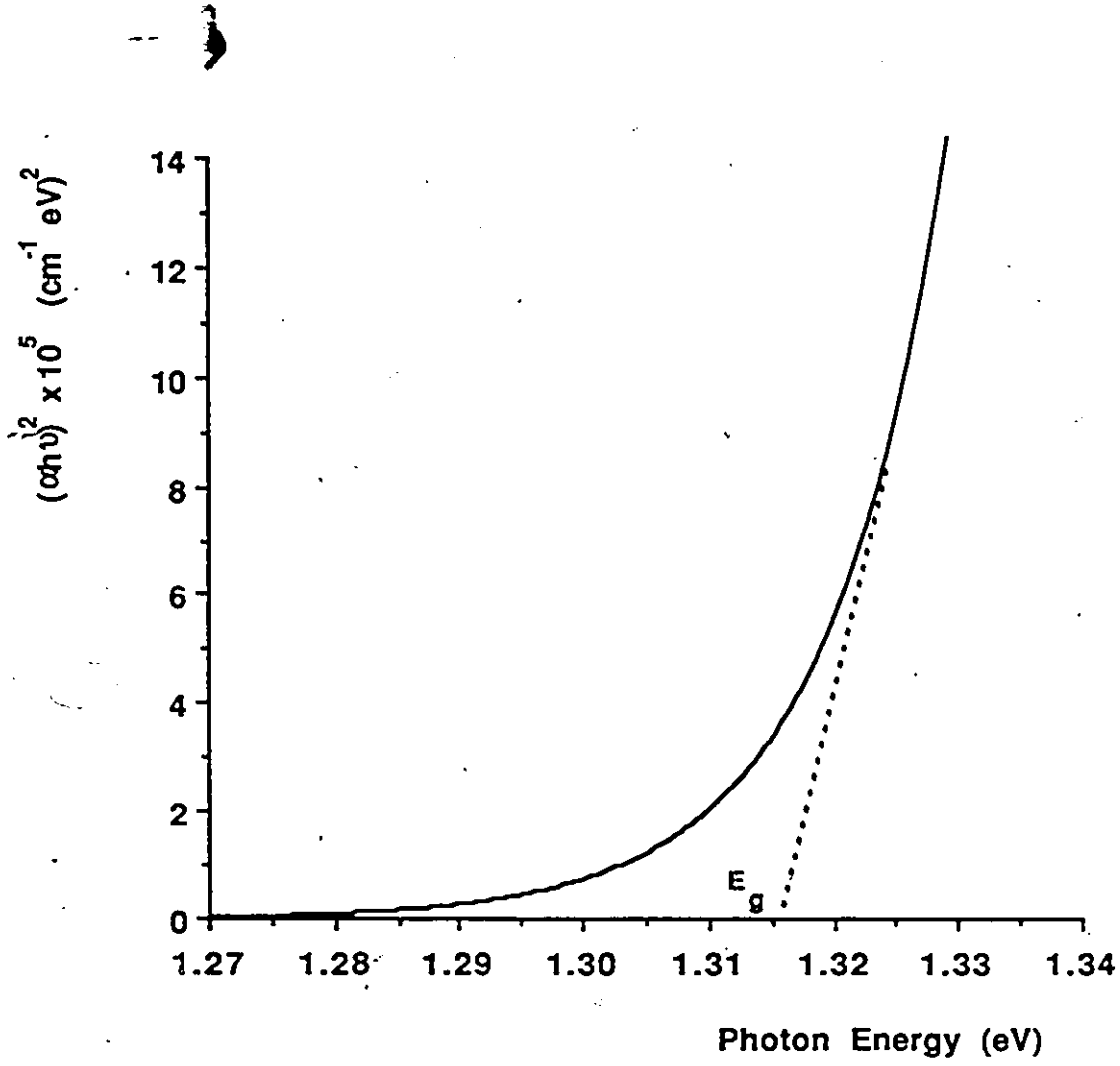

Fig (3.4) Variation of $(\alpha h\upsilon)^2$ with Energy for x=y, z=0.1

in Fig (3.5) and E_g with y for various z values in Fig. (3.6). The top line and the bottom line represent the energy variation on the two edges y = 0 [$Zn_{1-z}Mn_zTe$] (10) and x=0 [$(CuIn)_{1-z}Mn_{2z}Te_2$] (11). It is seen that over most of the range of z the energy gap varies linearly with z for each line. It is also seen in Fig. (3.5) that the lines for f = 0.125 ($z \geq 0.4$), f = 0.25 ($z \geq 0.2$), f = 0.5 ($z \geq 0.05$), f = 0.75 ($z \geq 0.05$), f = 0.875 ($z \geq 0.05$) and f = 1 ($z \geq 0.25$) intersect at the single point of 1.9 ev at z=1.0 agreeing with a similar value obtained by Quintero for the $Cd_{2x}(CuIn)_yMn_{2z}Te_2$ and $Cd_{2x}(AgIn)_yMn_{2z}Te_2$ (11). This is thus the extrapolated value of E_g for a hypothetical MnTe with the ordered structure. The lines which represent f = 0, f = 0.125 ($z \leq 0.3$), f = 0.25 ($z \leq 0.05$), f = 0.5 ($z \leq 0.05$) and f = 0.75 ($z \leq 0.05$) extrapolate to a value of 2.83ev at z = 1 indicating the value which a hypothetical zinc blende MnTe would have as previously obtained by Donofrio for $Cd_xZn_yMn_zTe$ alloys (10). Another significant feature of the variation in energy gap with z is that for f = 0.875 ($z < 0.2$) and f = 0 ($z < 0.3$), i.e. the chalcopyrite field, the values of E_g extrapolate at z = 1 to E_g=1.36eV, a value in agreement with the results obtained by Quintero (11).

The reason for obtaining two different aiming points for zinc blende can be explained in the following way. The line representing f = 0.125 shows a drastic change in energy gap between z = 0.3 and z = 0.4. This change suggests that there is a change in the structure (phase change) between the two points. Since enough information is not available, it is not possible to say whether this is a sudden change or a gradual change in the structure. The other lines also had this property but it is difficult to observe since the change is small. It is clear that the aiming point of the E_g versus z lines varies with structure concerned and this fact can be used to give a fairly good estimate of the

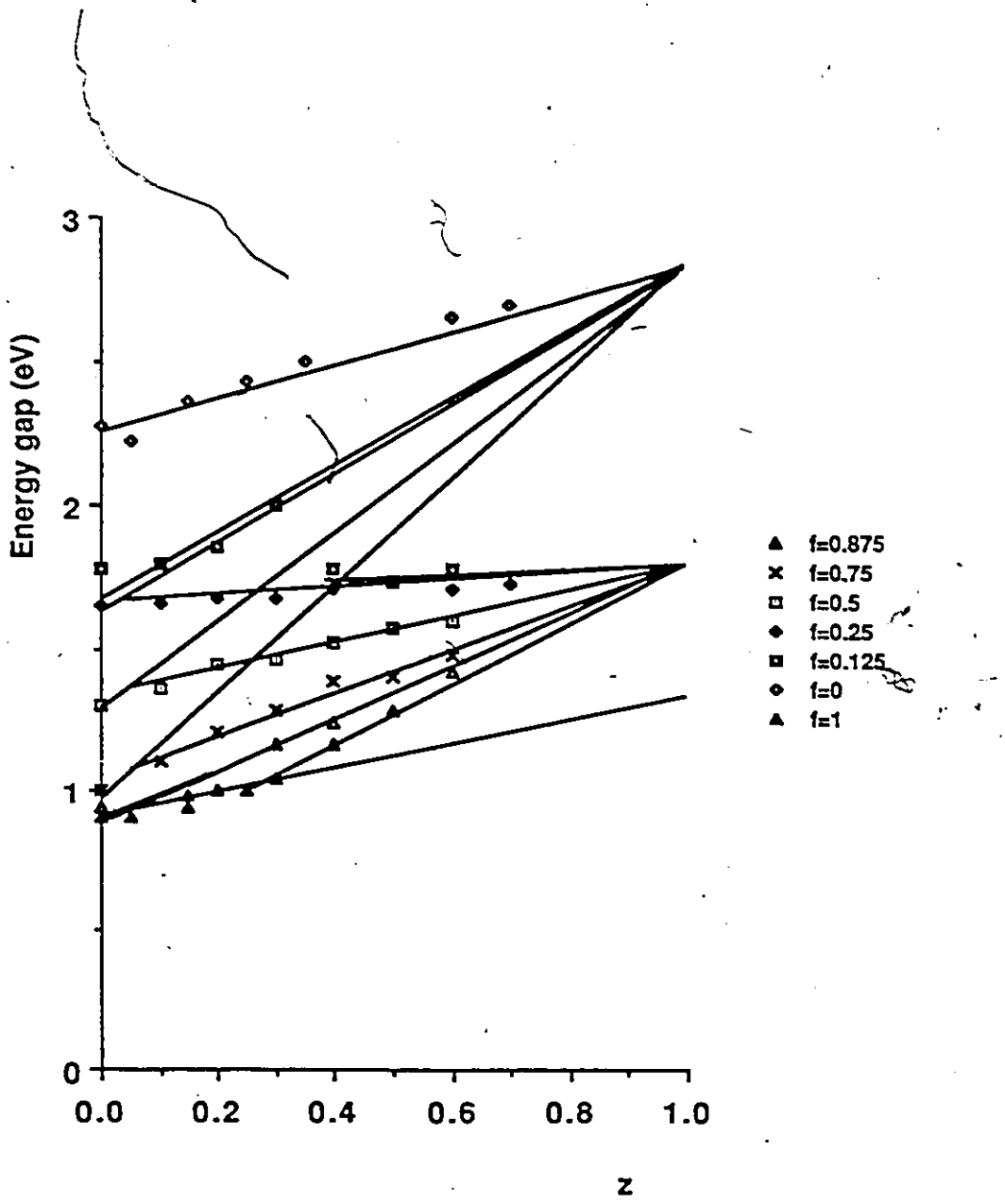

Fig (3.5) Variation of energy gap with z for different f=y/(x+y)

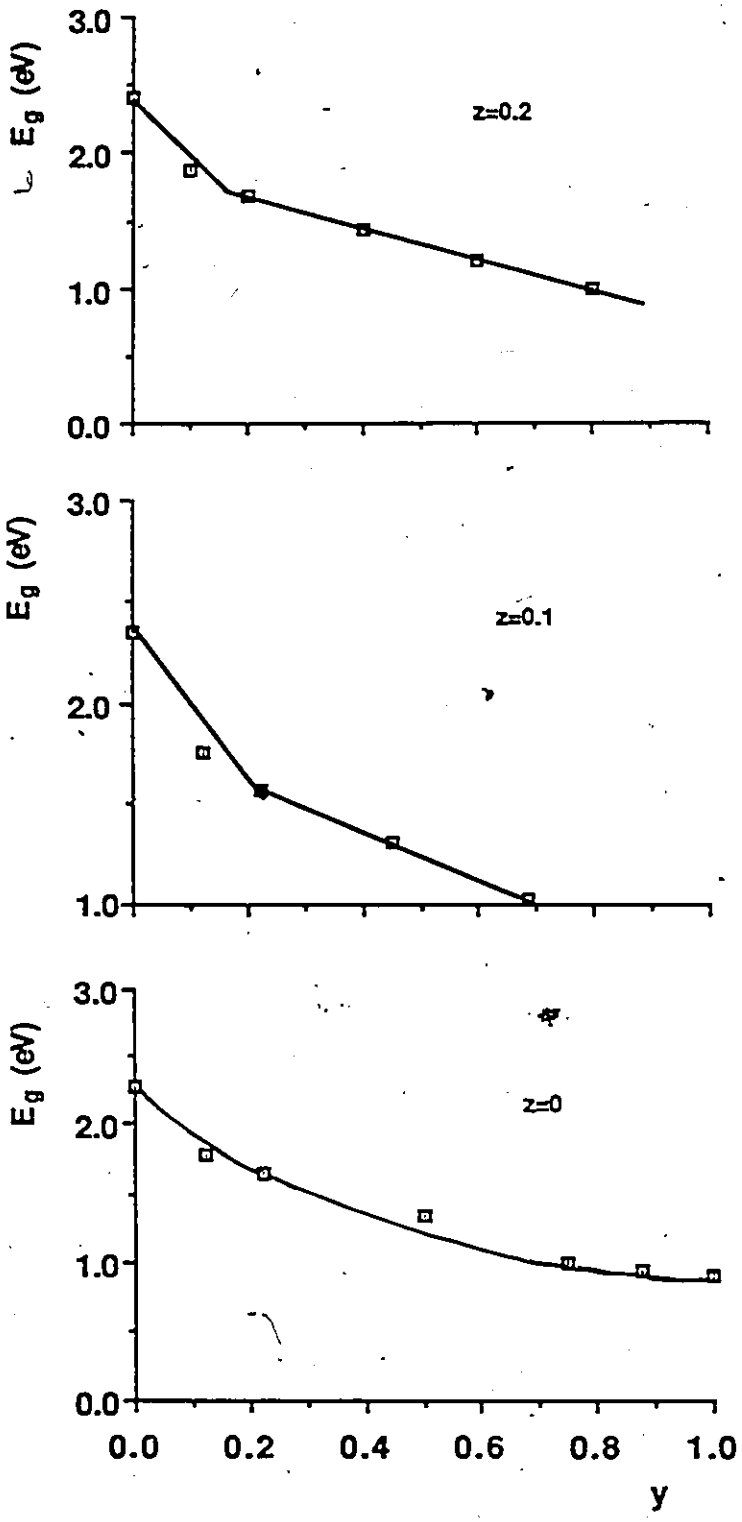

Fig (3.6a) Variation of energy gap with y for Constant z

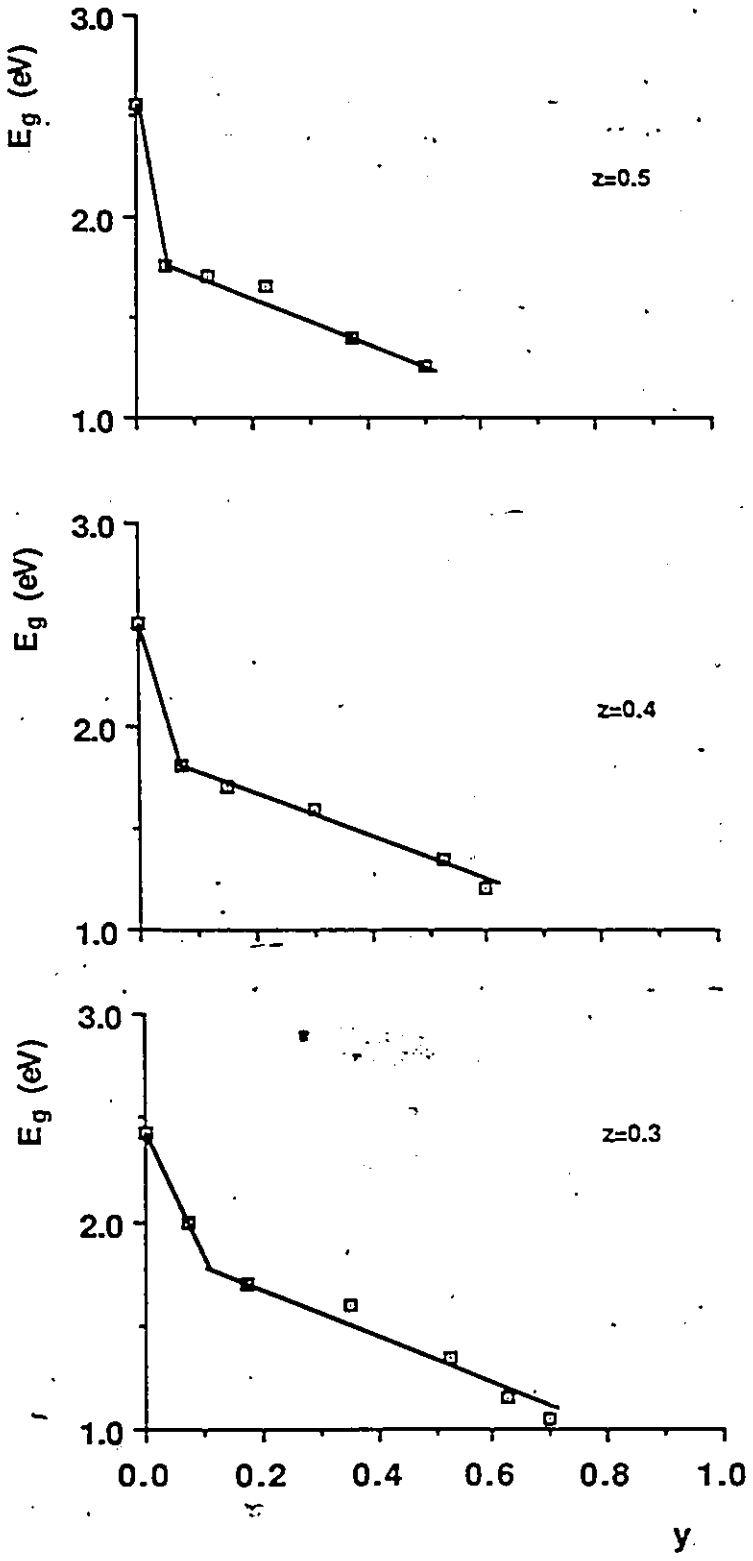

Fig (3.6b) Variation of energy gap with y for Constant z

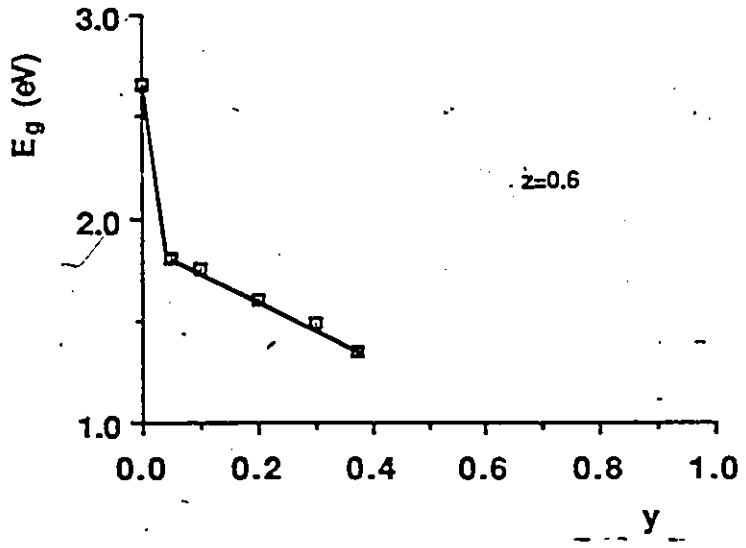

Fig (3.6c) Variation of energy gap with y for Constant z

boundaries of the various fields. Thus in Fig. (3.5) each value of E_g on the $z = 0$ line has been joined to the zinc blende value of 2.83ev at z=1.0. The points of intersections of these lines with the corresponding ones through the experimental values for $z \geq 0.4$ (f=0.125), $z \geq 0.2$ (f = 0.25), $z \geq 0.08$ (f = 0.5), $z \geq 0.08$ (f = 0.75), $z \geq 0.15$ (f=0.875) and $z \geq 0.25$ (f = 1) give a reasonable estimate of the boundary between the zinc blende and the ordered cubic fields.

Fig. (3.6) shows the variation of the energy gap with y for constant z. It is seen that for $z = 0$, the variation is not linear. However, the variation of E_g with y for z=0.1, 0.2, 0.3, 0.4 and 0.5 shows a linear relation within the limits of experimental scatter. Each line has a change in slope (except the line with $z = 0$) which indicates the presence of the phase change seen in Fig. (3.5). Other than that, beyond the point at which the change in slope occurs, the lines are parallel to one another within the experimental limits. A similar construction has been carried out in Fig. (3.6) to give an estimate of the ordered field boundary. In this diagram, the boundary limit is indicated by the point at which the change in slope occurs on each line. The approximate form of this ordered phase boundary is shown in Fig. (3.7)

3.5 Calculation of Constant Energy Gap Contours.

Since in the ordered range, the energy gap varies linearly with z and y, constant energy gap contours can be drawn easily using the same process as for the lattice parameter. The empirical formula describing the variation of energy gap with z and y for this phase may again be written as

$$E_g = A + By + Cz \qquad (3.8)$$

Using a least square fit for all the experimental values of energy gap in the ordered field, the

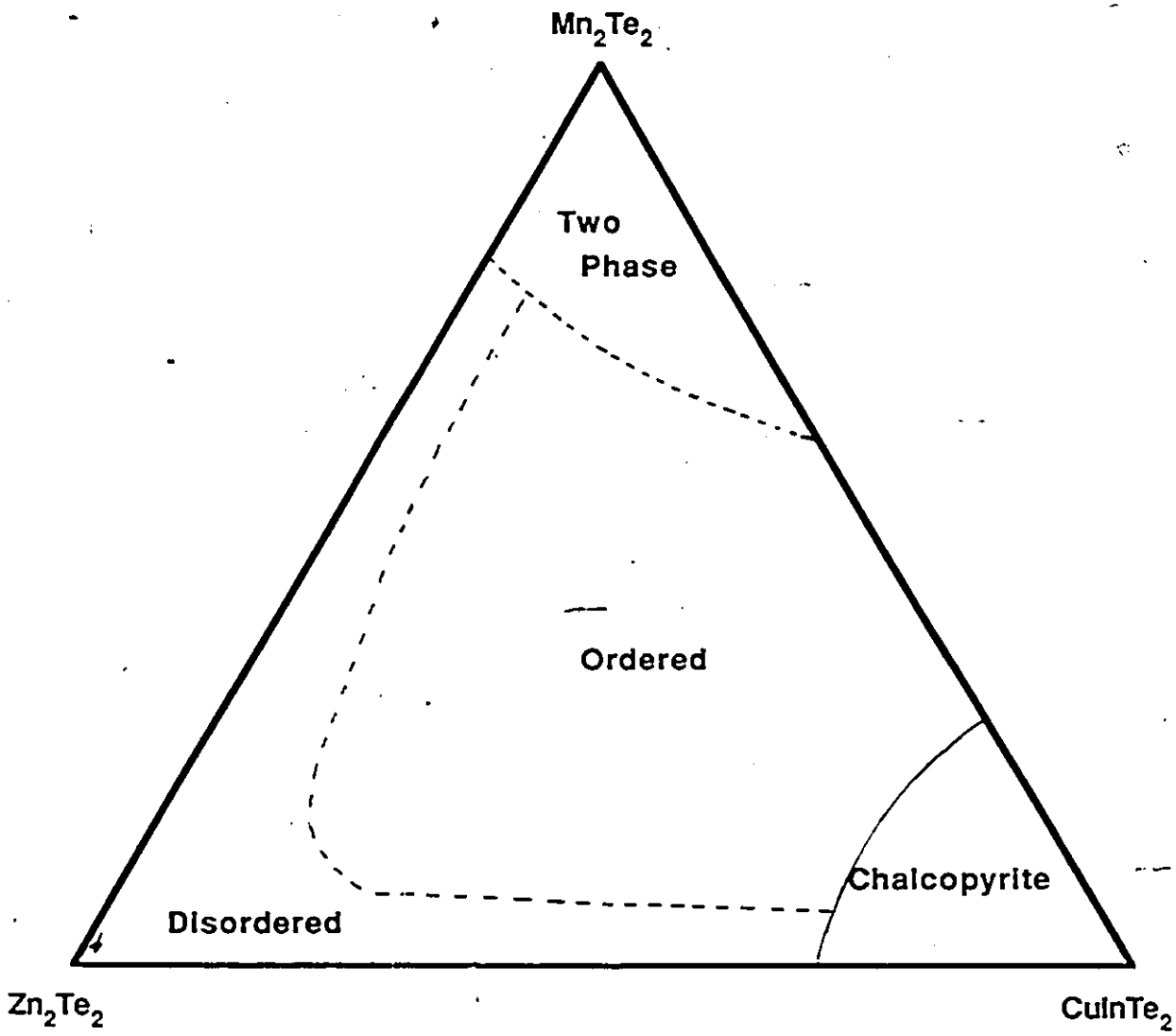

Fig (3.7) Illustration of the different phase fields involved in the system

three unknown constants were obtained as

$$A = 1.8959ev$$

$$B = -1.155ev$$

$$C = -0.0842ev$$

This gives the relation

$$E_g = 1.8959 - 1.155y - 0.0842z \text{ ev} \qquad (3.9)$$

with a standard deviation of $\sigma = 0.035$ev. The energy gap contours for the ordered phase field shown in Fig. (3.8), were obtained by numerical solution of equation (3.9).

In fig. (3.6), since the energy gap shows a non-linear variation with y for z =0, which lies in the disordered phase field, a more complicated expression would be needed for this range. There are insufficient points in the present work to justify making such an analysis. Since in Fig. (3.5), the phase change where the break occurs between ordered and disordered is fairly small for all lines except for f = 0.125, therefore by looking at the graph (3.6), the variation of energy gap vs y for z = 0, one can estimate the energy contours between the lines y = 3x and x = 3y. This can be described as follows. Using the curve E_g vs y for z = 0 {Fig. (3.6)}, we can find the y values for equal energy increments such as 1.1ev, 1.2ev, 1.3ev etc. For example, when E_g = 1.1ev, y = 0.68 and when E_g=1.2eV, then y = 0.42. These estimated constant energy gap contours in the disordered field are found to occur at the same positions as in the ordered field and these are illustrated in Fig. (3.8). However, the energy gap contours for the samples with y < 0.15 in the disordered field do not meet the energy gap contours in the ordered field because of the discontinuty in the energy gap values shown for the line f = 0.125 in Fig.(3.5). In this case

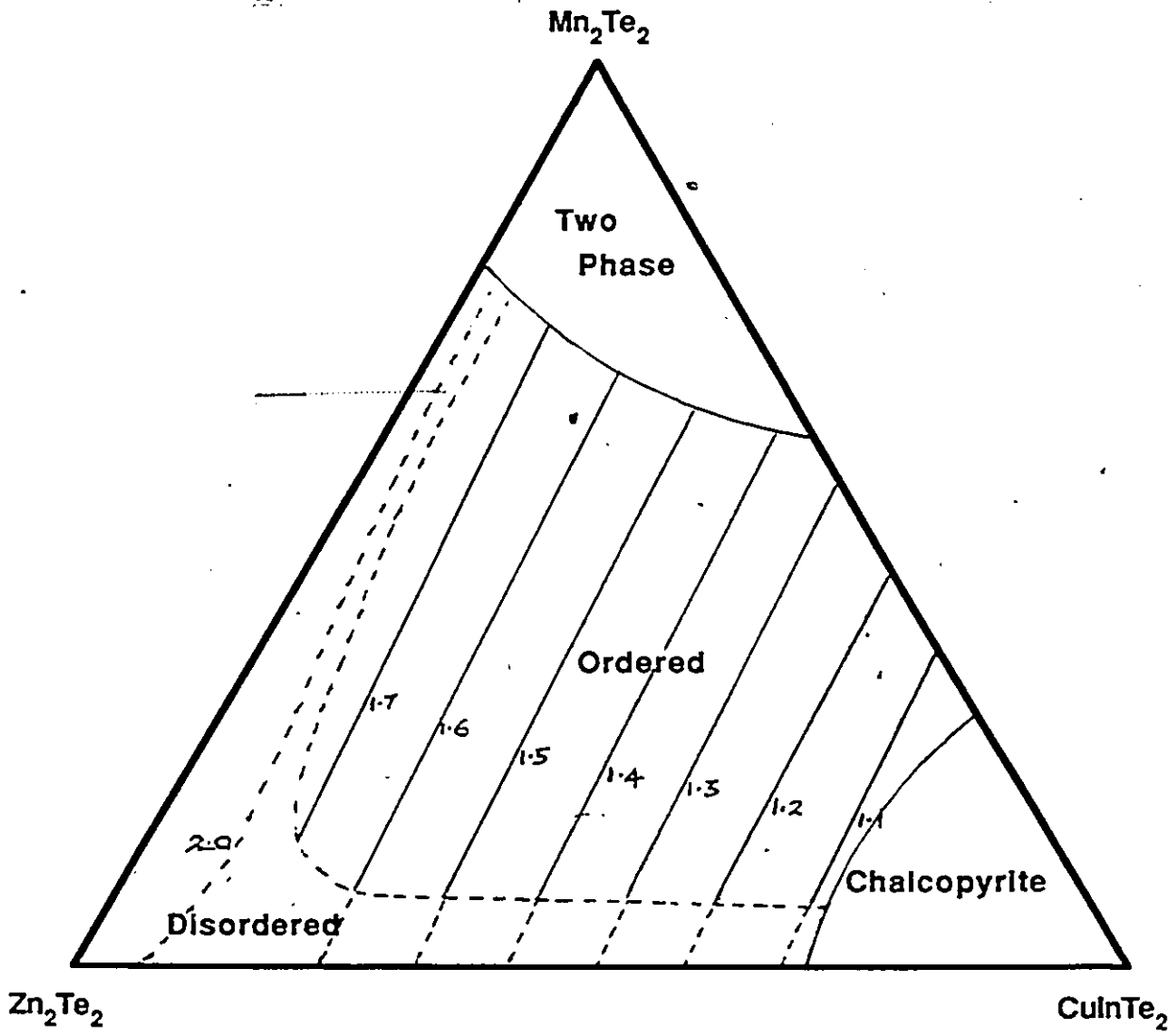

Fig (3.8) Values of constant energy gap.
The values indicated are in units of eV

only one contour for E_g = 2.0 eV has been roughly estimated.

Turning to the chalcopyrite materials, as mentioned earlier, the system has only a small region of chalcopyrite and hence little information on the energy gap variation has been obtained in this region. It is therefore not possible to give any significant constant energy gap contours for that region.

3.6 Discussion

To carry out the analysis of the type of transition occurring in these alloys any further, thinner samples are required, so that higher values of the absorption coefficient can be obtained.

With regard to the variation of E_g vs composition in this system, it can be seen from Fig. (3.5) that the alloys inside the composition diagram have different aiming points for different structures. In the range of single phase behavior, there is a field in which the chalcopyrite structure occurs, a normal zinc blende field in which the Mn atoms substitute for non - magnetic cations in a random manner and a large field in which the Mn atoms tend to order on the cation lattice. All of these phases are semiconductors and it is found that the value of the optical energy gap E_g and its variation with composition depend upon the structure concerned. The ordered field occurs because in these alloys the paramagnetic Mn ions order on the cation sub-lattice. It is to be noted that the ordered field extends to near the $Zn_{1-z}Mn_zTe$ edge so that more experimental work is required to determine the exact position of the boundary.

With regard to chalcopyrite samples, because of the limitations of the present experimental system, no measurements could be made on samples with values of $z \leq 0.15$. For these samples, the energy gap is relatively small (about 1.0eV) and hence either very thin samples or a more sensitive detector would be needed. As mentioned earlier, since the

alloys are polycrystalline, they tended to crumble while being removed from the rod and very thin samples were not possible for the chalcopyrite alloys. As a result, in these cases, the background absorption is so high that no absorption edge could be observed. Since the present chalcopyrite region is small, only a few energy gap measurements were made. Because of the non - linear variation of the energy gap with y for z = 0, a linear expression can not be used to represent the variation of energy gap with composition in this range. All of these alloys have Mn distributed through the cation sub-lattice and so show behavior typical of semimagnetic semiconductors. The occurrence of these ordered and disordered structure will be discussed in chapter 4 and 5 which describes the magnetic behavior of these alloys.

With regard to the accuracy of the various points shown in Fig. (3.5) and Fig. (3.6), a similar consideration appears as discussed in page 28 for lattice parameter values. For any given sample, the accuracy in E_g should be no worse than $\pm$ 0.05eV. (see Fig. (3.4)). However as shown on page 28 the accuracy in z etc. is approximately $\pm$ 0.02 and hence both parameters have about equal effect in producing experimental scatter in the E_g vs composition graphs.

Chapter 4

Magnetic Susceptibility Measurements

4.1 Introdution

The presence of the magnetic atoms is responsible for the magnetic properties of these semimagnetic semiconductors and in most cases these magnetic ions are randomly distributed over one or more cation sub-lattices. The properties seen in susceptibility and ESR measurements are determined by the interaction between the magnetic ions, which in the case of manganese have a magnetic moment of five Bohr magnetons since the half filled $3d^5$ shell of the ion contains five electrons with aligned spins. Atomic theory has shown that the magnetic dipole moments observed in bulk matter arise from two origins, one is the motion of electrons about their atomic nuclei (orbital angular momentum) and the other is the rotation of the electron about its own axis (spin angular momentum). According to quantum mechanics, the magnetic moment associated with these two momenta of an atom can be written as

$$\mu_J = - g\mu_B J \qquad (4.1)$$

where g is the splitting factor which is given by the Landé formula

$$g = 1 + \frac{J(J+1) + S(S+1) - L(L+1)}{2J(J+1)} \qquad (4.2)$$

μ_B is the Bohr magneton $\{e\hbar/2mc\}$ and J is the additional quantum number which determines the total angular momentum due to the vectorial combination of the orbital and spin angular momenta. The vector addition of the quantum numbers results in only partially

filled electronic levels possessing a non-zero resultant momentum. The five unpaired 3d electrons of manganese results in a value of spin momentum, S,equal to 5/2. In a solid, the orbital angular momentum may not contribute anything to the total angular momentum because it is quenched by the crystal field. Therefore eq.(4.2) can be simplified by using this result, which then gives g = 2.

Since the manganese ions give a net magnetic moment, the solid shows a magnetic behavior which depends upon the type of interaction between the magnetic moments. One useful way to investigate this magnetic behavior is to measure the magnetic susceptibility χ which is defined as the ratio of the magnetization M (magnetic moment per unit volume) to the applied field H

$$\chi = \frac{M}{H} \qquad (4.3)$$

All magnetic materials can be categorized into three main groups. For the first one, diamagnetic materials, the susceptibility is negative and the temperature T does not enter explicitly into the formulation. Since all matter contains electrons moving in orbits, diamagnetism occurs in all substances. For the second group, which are known as paramagnetic materials, Curie (22) showed that the susceptibility is temperature dependent and field independent. The susceptibility of a paramagnetic material is positive and according to Curie' s Law, is given by

$$\chi = \frac{C}{T} = \frac{N g^2 \mu_B J (J+1)}{3 k_B T} \qquad (4.4)$$

where C is the Curie constant, N is the number of magnetic atoms, k_B is the Boltzman

constant, T is the temperature in Kelvin and g is given by eq. (4.2). Paramagnetism is due to the existence of permanant magnetic dipoles which are randomly oriented. In these materials the interaction between the spins is negligible. There is no net magnetization in the absence of a field. When a magnetic field is applied there is net dipole moment in the direction of the field giving rise to a weak magnetization or paramagnetism. When dipole-dipole interaction is negligible experiments showed that paramagnetic materials obey Curie's Law as defined by eq. (4.4).

However, some materials have susceptibilities that can be fitted to the equation

$$\chi = \frac{C}{T - \theta} \qquad (4.5)$$

where θ is a constant which depends on the interaction between the atomic magnetic moments. This may result in some kind of alignment or correlation among these various moments or spins in the lattice at low temperatures. This third category includes three important classifications. If the atomic moments are aligned parallel, then the substance is said to be ferromagnetic. As a result, at low temperatures a spontaneous magnetization exists in the material. Above a critical temperature T_C which is known as the ferromagnetic Curie temperature, the spontaneous magnetization vanishes. In this type of material, the paramagnetic temperature θ is positive. An antiferromagnetic material is a substance in which an antiparallel arrangement of the srongly coupled magnetic dipoles are favoured. The Curie temperature T_C of ferromagnetism has its counterpart, the Neel temperature, that is, T_N is the temperature above which the antiparallel arrangement of the dipoles disappears. This behavior can be described by equation (4.5) with $\theta < 0$. An antiferromagnet can be

illustrated simply by a body centered cubic lattice which can be divided into two sub-lattices, one represented by the body center site and the other by the corner sites. Each sub-lattice contains an internal parallel alignment but the direction is opposite to the other sub-lattice. The final classification that falls into the third category is ferrimagnetic materials. These are materials which below a certain temperature possess a spontaneous magnetization that arises from an antiparallel arrangement of the strongly coupled atomic dipoles. In this case, the sub-lattice magnetizations are not equal and there will be a net magnetic moment.

Over the last two decades another distinct magnetic state known as spin glass has been recognized. Spin glass behavior was first observed in fairly concentrated alloys of iron in gold (AuFe) and manganese in copper (CuMn). In these materials the spins interact with each other in a such a way that when the temperature is low enough, for this interaction to overcome the thermal agitation, the spins freeze into a completely random configuration (3). To explain the behavior in spin glass materials, a new concept "frustration" was suggested by Toulouse (23). Frustration occurs when there is a conflict in the interaction between spins. In the typical SMSC, magnetic ions distributed at random over the f.c.c. sub-lattice interact antiferromagnetically with each other. For any given magnetic ion, these interactions result in contradicting demands concerning the spin direction of the magnetic ions. Consequently at $T < T_{spin\ glass}$, all magnetic ion spins are frozen in random orientation. In spin glass materials the magnetic susceptibility measurements show a cusp like peak at a well defined temperature T_g, the spin glass temperature and the behavior is similar to an antiferromagnetic (24). The random freezing of spins at T_g was confirmed by Mossbauer effects (25) and neutron diffraction (26) experiments.

In order to understand this spin glass behavior one has to know the nature of the

interaction between the spins. Before developing a theory of spin glasses, it is important to construct a reliable model for the form of the interaction between spins. The interaction can be described in terms of the Heisenberg Hamiltonian

$$H = -\Sigma J_{ij} S_i S_j \qquad (4.6)$$

Here J_{ij} is the exchange interaction between the i^{th} and j^{th} spin. The exchange interaction can be classified into two forms, direct and indirect. In direct exchange interaction the exchange energy appears from the above equation as though there existed a direct coupling between the two spins (S_i and S_j) and this is illustrated in Fig. (4.1a). The sign of the exchange integral J_{ij}, which depends amongst other things on the distance between the interacting spins, determines the kind of alignment of the spins. If the exchange interaction is positive, then it leads to a ferromagnetic state and if it is negative it gives an antiferromagnetic behavior. Indirect interaction occurs through an intermediary such as through the outer p electrons of a diamagnetic ion. An example of this type of exchange, which is known as superexchange, would be MnO. In this compound manganese ions are coupled together through an oxygen ion.

In dilute solid solutions of a magnetic metal crystal (such as Mn in Cu, Mn in Au) the exchange coupling between the ion and the conduction electrons has important consequences. The conduction electrons are polarized in the vicinity of the magnetic ion and this causes an indirect exchange interaction between two magnetic ions. The interaction is known as the RKKY interaction (Ruderman - Kittel - Kasuya - Yosida). In this mechanism, the variation of $J_{ij}(r)$ with distance is illustrated in Fig.(4.1b). It can be seen that the exchange interaction, $J_{ij}(r)$ oscillates with the distance and dies away rather slowly as the

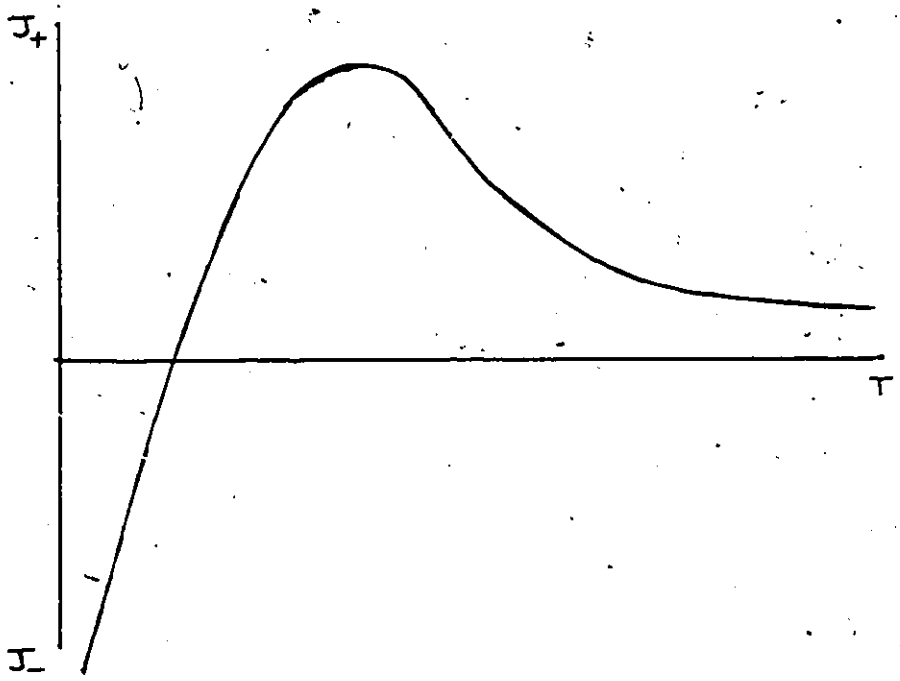

Fig. (4.1a) Direct Exchange Interaction

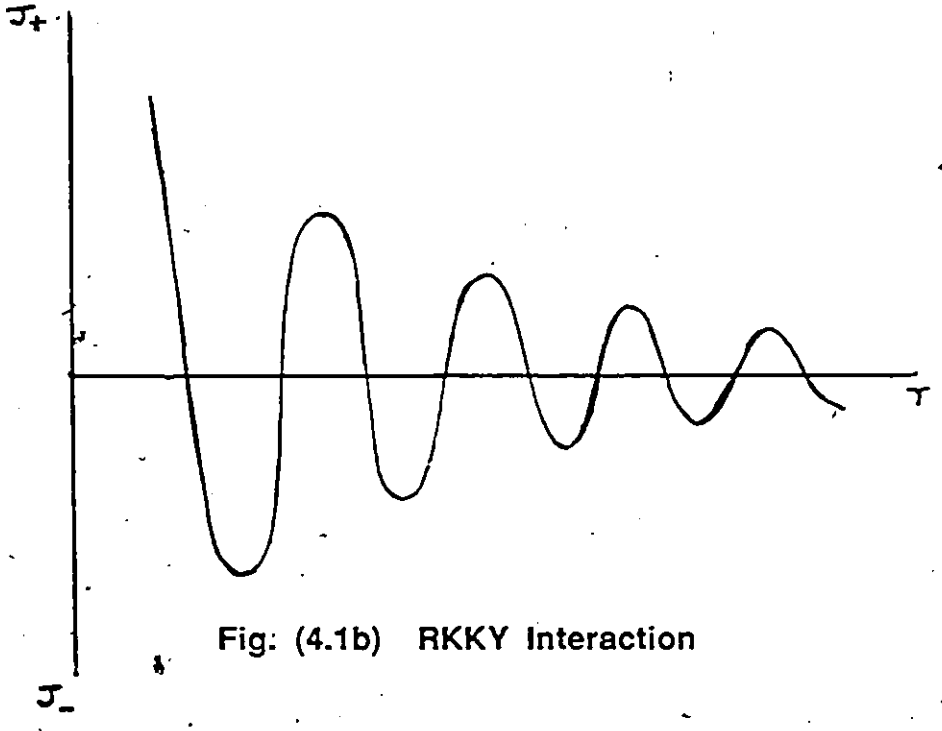

Fig: (4.1b) RKKY Interaction

inverse cube of the distance from a given spin. This oscillatory interaction is important for understanding spin glass behavior in metals (3). The coupling between the magnetic moment of spins can be either ferromagnetic or antiferromagnetic depending upon their separation. This results in a competition between ferromagnetic and antiferromagnetic interaction among the randomly distributed magnetic spins. This leads to frustration which requires these spins to freeze in a disordered fashion in order to minimize the energy of the system.

The RKKY interaction occurs in metallic spin glasses such as CuMn etc., since they have a high carrier concentration (27). However, the present system belongs to the group of materials which behave like insulators at low temperatures because of its large electronic energy gap and low carrier concentration. It was pointed by De Seze (28) and discussed by Villan (29) that a frustrated disordered system with only antiferromagnetic interaction can give an insulating spin glass. The present system is one of the examples of insulating spin glass with a zinc blende lattice where manganese atoms are distributed randomly. Furthermore, in semimagnetic semiconductors, since manganese ions interact only antiferromagnetically, the observed spin glass phase cannot be ascribed to a competition between ferro and antiferromagnetic interaction. Therefore a spin glass regime with only antiferromagnetic interaction was predicted for an f.c.c. lattice due to frustration (21).

A possible superexchange mechanism that has been suggested by various theoretical work is known as the Bloembergen-Rowland interaction (30). In this mechanism, the exchange interaction is a result of a virtual transition between the filled valence band and the empty conduction band. Recently, this aspect has received considerable theoretical attention in SMSC literature. Another theory which is known as Anderson - type superexchange was proposed by Goncalves de Silva and Falcov (32) to explain the magnetic properties of rare earth compounds and this theory was extended by Geertsma et al (33) to describe the

exchange mechanism in transition metal compounds. This will be discussed later in some detail. One of the main objects of our investigation of the magnetic susceptibility is to try to identify which exchange mechanism is dominant in our alloys.

4.2 Experimental Procedure

Magnetic susceptibility was obtained by magnetization measurements as a function of temperature in the range 4.2 - 250 K. A superconducting quantum interference device (rf SQUID) was used to measure the magnetization. The magnetic flux sensor of such a magnetometer is a pair of oppositely wound superconducting coils coupled to an rf SQUID. This instrument may be used to measure small magnetic fluxes (10^{-11} gauss.cm^2) very accurately. For this set up only a small amount of sample (~20 mg) is needed and small magnetic field would be enough to cause the required induced magnetization. If the sample is placed inside one of the two coils, a change in its magnetic flux is sensed by the SQUID which produces a change in the output of the magnetometer. Fig. (4.2) shows a schematic cross-section of the apparatus used to investigate the magnetic susceptibility in the present work. This set up was mainly designed by Dr. Gilles Lamarche in Ottawa University. In this set up, an inside-out Dewar arrangement allows samples to be inserted through the pick up coils. The inner dewar was filled with liquid helium while the outer one contained the liquid nitrogen. Surrounding the lower portion of the inner dewar which contained the sample was a lead shield which prevented external stray fields from reaching the pick up coil region. Inside the lead shield the magnetic field in a range between 25 -30 gauss was supplied through the solenoid. A superconducting cylindrical niobium shield was interposed between the solenoid and the pick up coils. This shield traps the field when helium is transferred to the dewar as well as providing additional magnetic shielding.

The magnetometer was a commercial rf pumped SQUID (system 330 S.H.E.

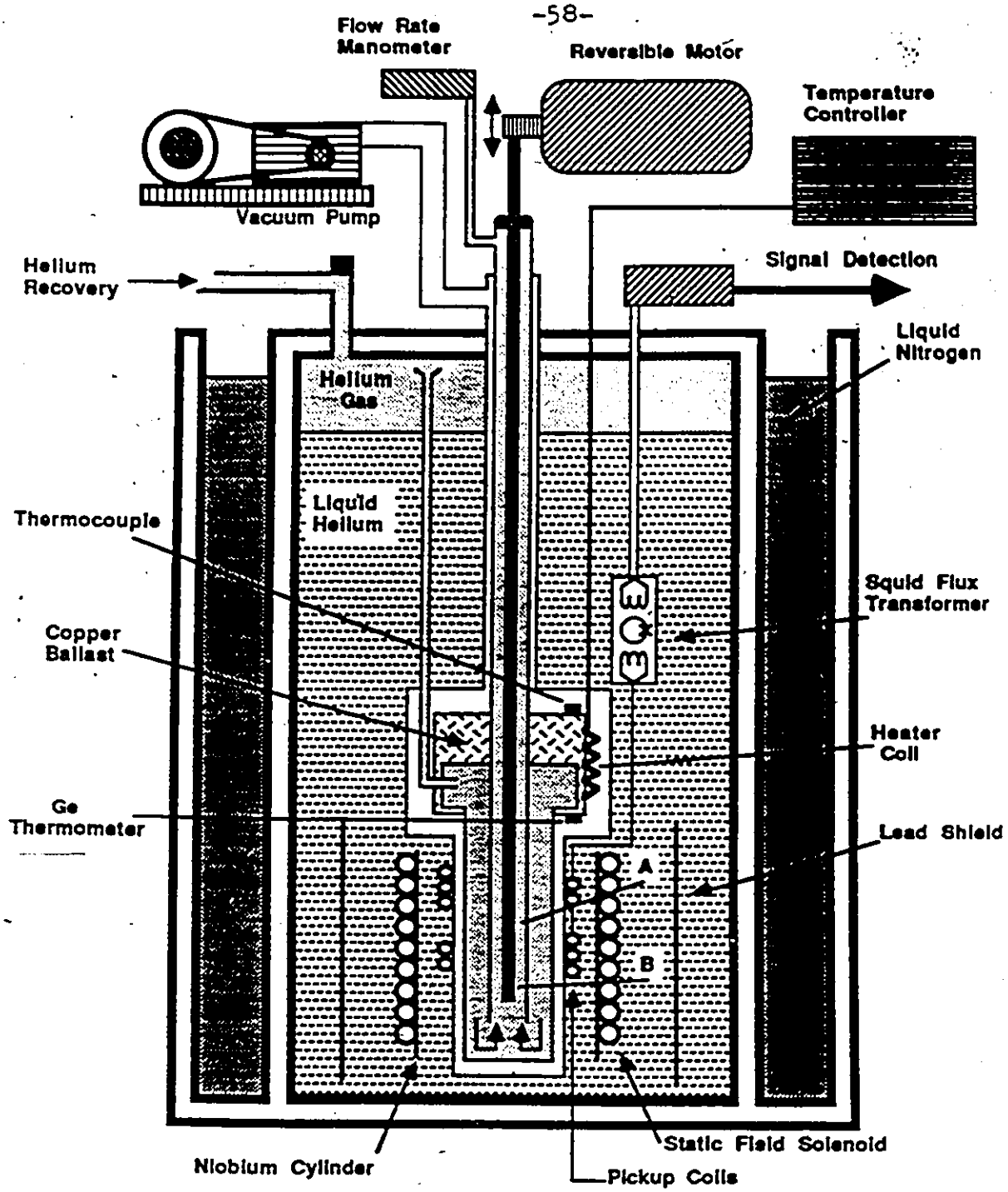

FIGURE 4.2 Magnetic Susceptibility Apparatus. A sample is placed in position B. A second sample or a paramagnetic salt is placed in position A.

Co-op). The vacuum container and the exchange helium gas chamber as well as the sample holder were made of pure copper. This helped in preventing interference of the magnetization of the holder with the measurements of the samples. It was noticed that the whole system needed to be opened to insert the different samples. To overcome this problem and for the sample to move through the pick up coil properly, the holder was attached to a long plastic rod. A reversible motor was attached to the other end of the rod, and it was extended outside the cryostat. As mentioned earlier, two sets of oppositely wound superconducting coils provided two consecutive measurements of the magnetization of the sample as it passed through each of the sets of coils. Thus the average magnetization was obtained. It was essential to control the temperature in the system and this was done by disseminating helium gas around the sample. Helium gas from the upper part of the inner dewar, entered a tube and passed through the inner container. This tube was wrapped several times around a copper ballast which provided stability. Helium gas was heated by attaching a heating coil to the copper block. The gas was heated and it passed through this point. From there the gas entered a double concentric tube system which directed it around the sample and out of the dewar. A flow manometer was attached to the exit end of the tube to control the pressure.

To measure the temperature of the sample without interfering with the magnetic measurements, the following procedure was used. Three different thermometers at three different places were used. A chromel gold 7% iron thermocouple which [redacted] connected to the temperature controller was placed on the top of the copper block. This was used as a reference for controlling the temperature. A calibrated Ge thermometer was located near the bottom of the block. Finally a paramagnetic salt magnetic thermometer calibrated against the Ge thermometer was positioned on the sample holder about 10 cm above the sample. The measuring system was calibrated by Dr. Gilles Lamarche using small lead spheres. The

following calibrated expression was used to calculate the susceptibility.

$$\chi = \frac{(1.25 \times 10^{-5})\,V}{(i/2 + 0.23)\,M} \quad \frac{emu}{gm} \qquad (4.7)$$

The SQUID voltage is represented by V and the mass of the sample in grams by M and i represents the current through the solenoid in mA.

4.3 Results

Magnetic susceptibility measurements were made as a function of temperature to obtain the spin glass transition temperature T_g and the Curie-Weiss paramagnetic temperature θ for the alloys. These measurements were carried out only in single phase cubic and chalcopyrite materials. The values of magnetic susceptibility versus temperature for a wide range of magnetic compositions are shown in Fig. (4.3). When the samples were initially zero-field cooled, cusp like peaks were observed at the spin glass transition temperature for compositions $0.2 \leq z \leq 0.6$. For samples with $z < 0.2$, it was impossible to determine transition temperature values since they occur below 4.2 K which is the limit of the present equipment. Fig. (4.4) and Fig. (4.5) show the reciprocal susceptibilities of some samples as a function of temperature. Two features worthy of note are apparent at $T > T_g$ in these two figures. The high temperature portion clearly indicates Curie-Weiss behavior providing a reliable measure of the Curie-Weiss temperature θ. This can be obtained by extrapolating the line which represents the Curie-Weiss behavior to the temperature axis. Below about

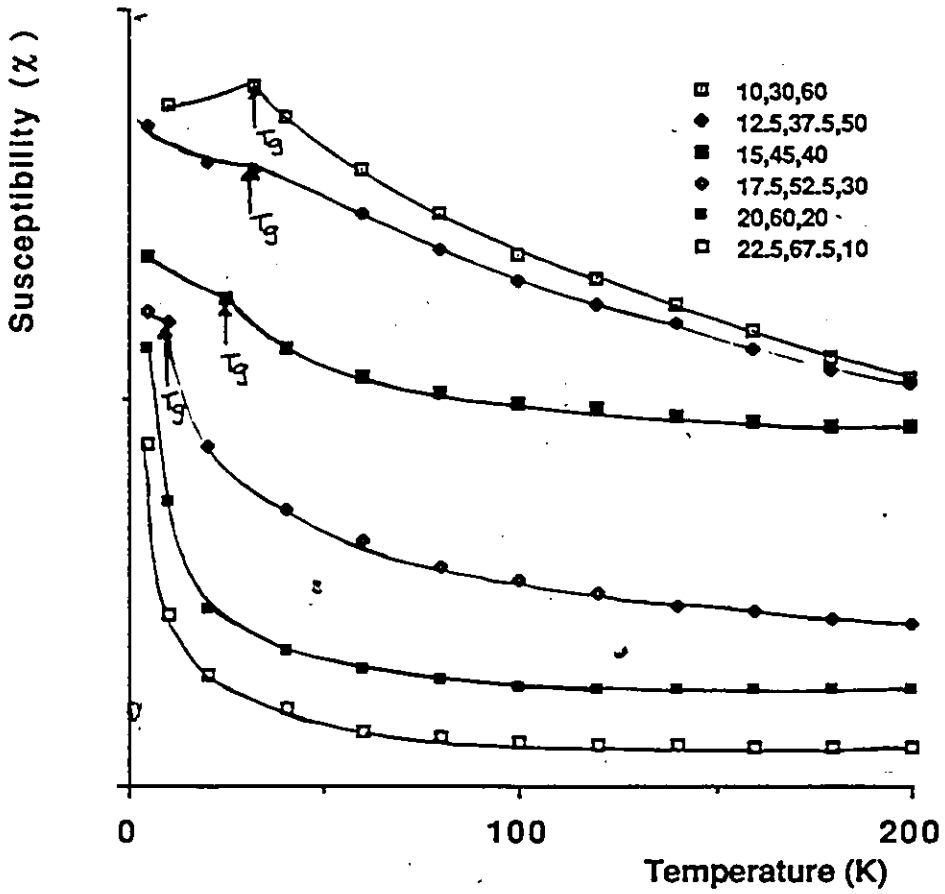

Fig (4.3) Plots of susceptibility vs temperature for various Mn concentration on y=3x line. The relative magnitude of the curves between the samples are not drawn to scale.

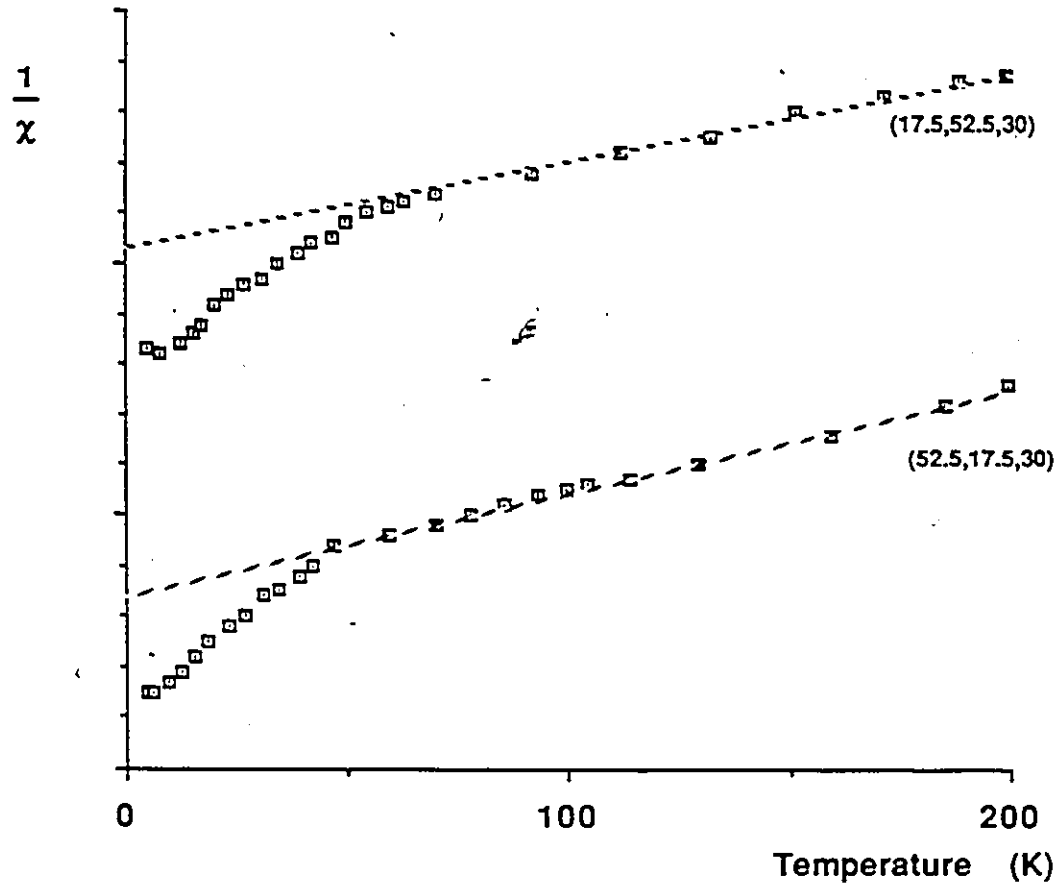

Fig (4.4) Plots of the Reciprocal Susceptibility vs Temperature. Arbitrary Units are used on 1/ χ Axis. The Broken Lines are Drawn to Fit the Linear Part

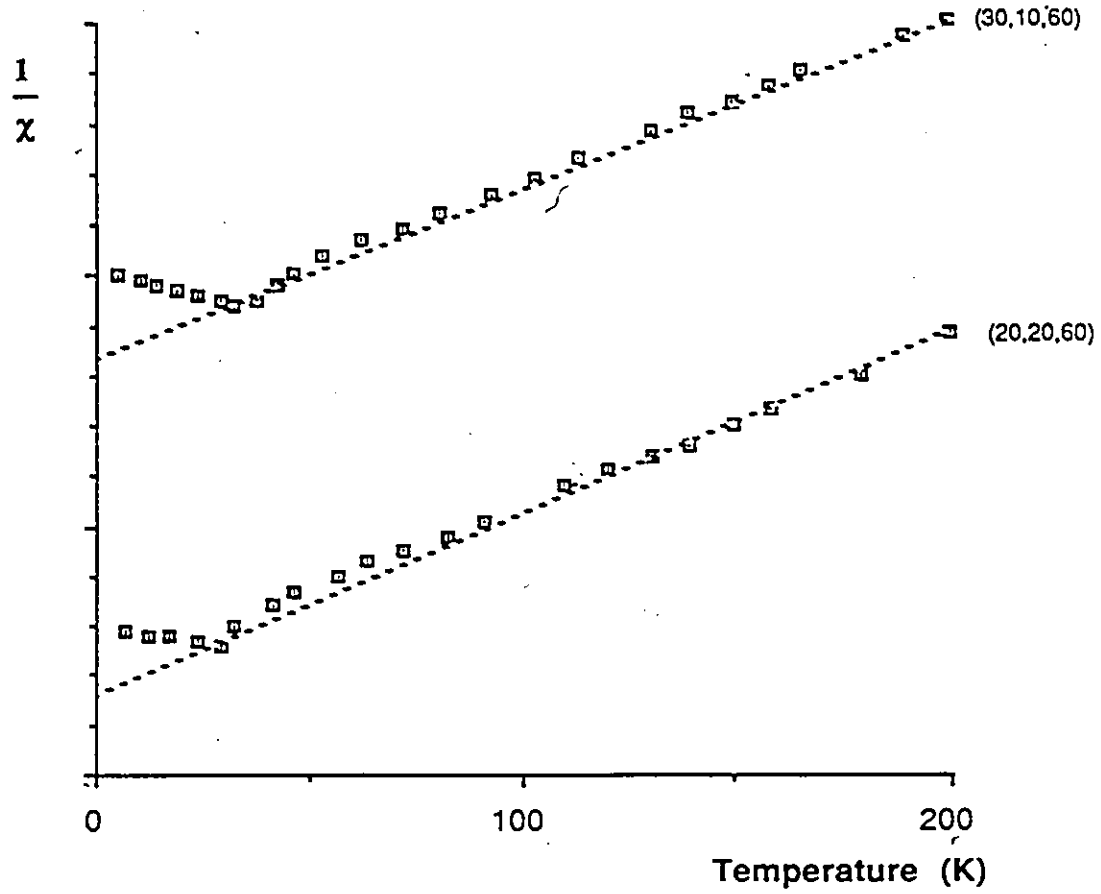

Fig (4.5) Plots of the reciprocal susceptibility vs temperature.
Arbitrary units are used on 1/ χ axis.
The broken lines are drawn to fit the linear part.

50K one also observes a characteristic downturn of χ^{-1} curve from the behavior predicted by the Curie-Weiss Law for $z<0.6$. Such enhanced paramagnetism is observed in all semimagnetic semiconductors above T_g. This can be explained by the possibility of the random orientation of the spins. At high temperature, the correlation between the spins is negligible. When the temperature is lowered the correlation of spins is enhanced and at T_g it becomes infinity. It is seen that for samples with higher manganese concentration show an upward deviation from the line which gives the Curie-Weiss temperature Fig. (4.5) while the samples with lower manganese concentration show a downward deviation from the line described above, Fig.(4.4). This deviation is due to the behavior of magnetic spins which begin to align as the temperature is lowered from higher values and this will be discussed in detail later in this chapter.

The values of T_g resulting from the magnetic susceptibility measurements for all samples in the cubic single phase are represented in Fig. (4.6). As illustrated in Fig. (4.3), it was noticed that for all cases , one fairly strong peak was observed corresponding to the spin glass transition temperature. But for some samples with $z \geq 0.3$ a second smaller peak was found. The relative amplitudes of these peaks depended upon how the samples were cooled from the annealing temperature. The χ vs T curve for a sample with the second peak is shown in Fig. (4.7). Despite these magnetic effects, as indicated above, the x - ray photographs showed the presence of a single chalcopyrite or cubic phase in each case (11). Because of this and bearing in mind the faint ordering lines observed for some $Cd_{2x}(AgIn)_yMn_{2z}Te_2$ (11), it would seem that the difference between the two phases observed is the crystallographic order or disorder of the manganese atoms on the appropriate

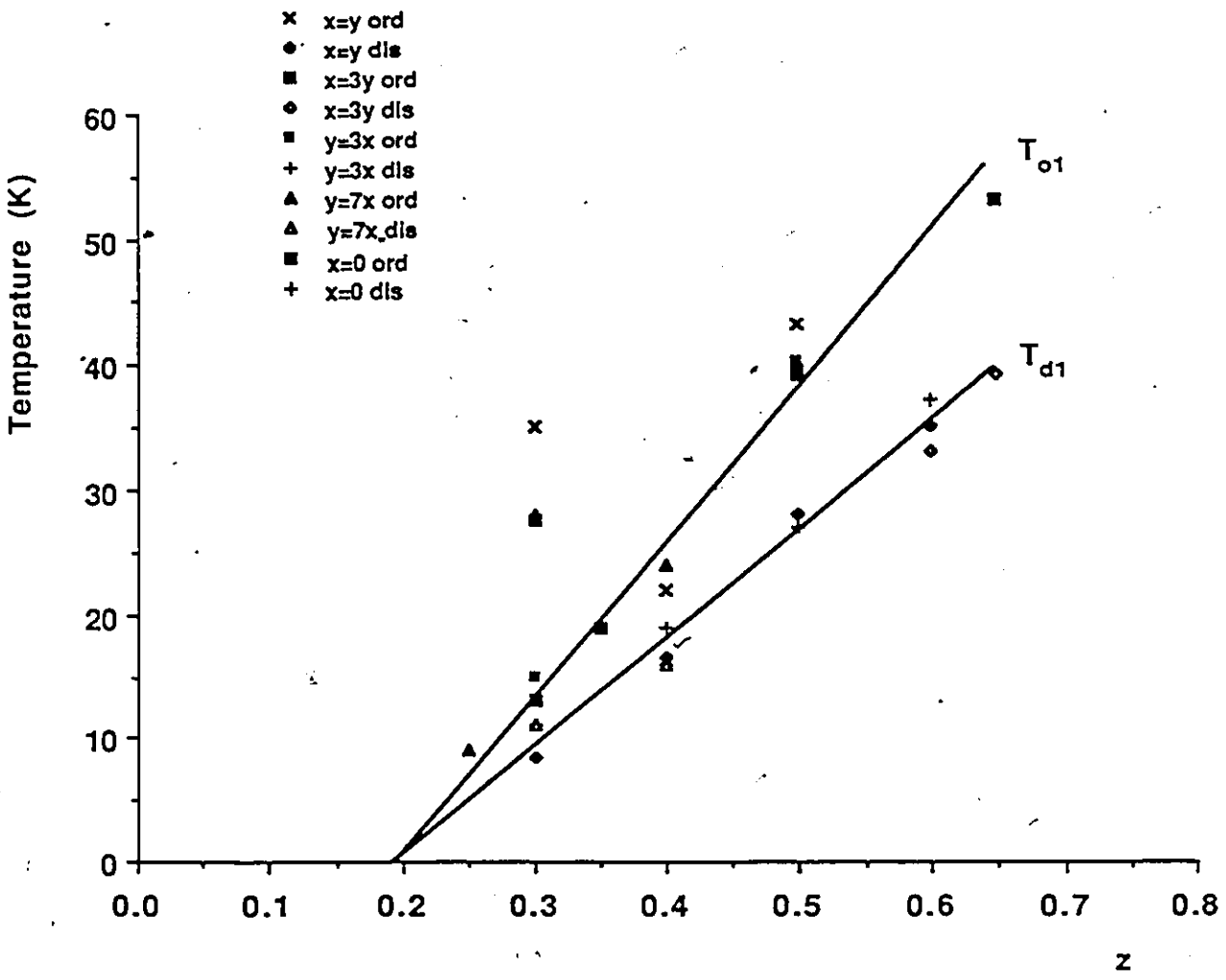

Fig (4.6) Spin glass transition temperature vs z
for ordered (T_{o1}) and disordered (T_{d1}) cubic samples

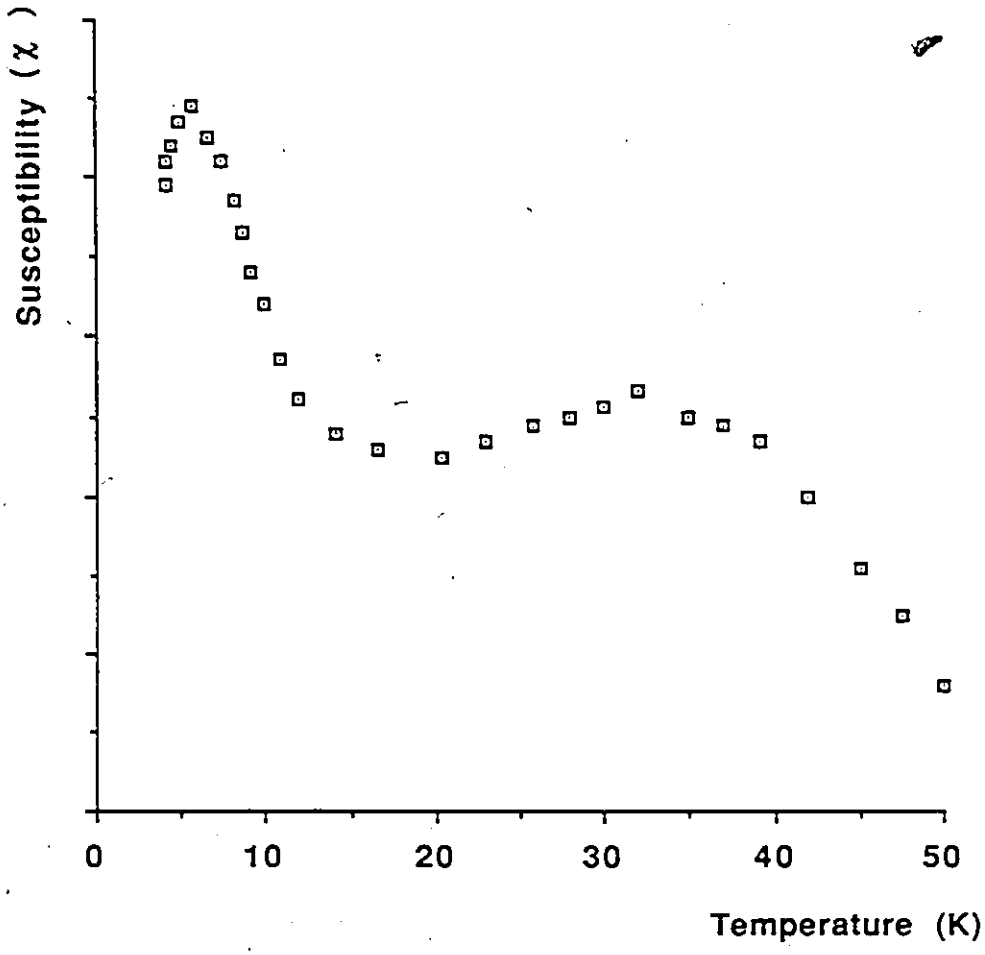

Fig (4.7) Temperature Dependence of the Magnetic Susceptibility for the Sample x=y z=0.3

Arbitrary Units are used on χ Axis

lattice. The effects of cooling rate etc. indicate that the low transition temperature T_d corresponds to the disordered structure in which the manganese ions are distributed randomly on the cation lattice. The higher transition temperature T_o correspond to the ordered structure with the crystallographic order of manganese ions. In Fig. (4.6), the lower line T_{d1} indicates the disordered structure and the upper line T_{o1} shows the transition temperature for the ordered sructure for the cubic phase. Both of these lines appeared to be straight except the transition temperature for samples with z = 0.3. For these samples points are scattered and this is probably due to the variation in the degree of order in the sample rather than to chemical composition. Similar results have been obtained for the chalcopyrite samples and these are shown in Fig. (4.8). Since the present system has only a small region of chalcopyrite, it is useful to quote the results from similar systems obtained by the members of the present research group. In the chalcopyrite region, the lower line T_{d2} represents the transition temperature corresponding to the disordered chalcopyrite with a completely random manganese distribution on the cation lattice while the upper line T_{o2} shows the transition temperature corresponding to chalcopyrite with the crystallographic order of manganese. As mentioned earlier, the scatter in the values may be due to the variation in the degree of order. The results for most of the chalcopyrite samples for all systems (11-12-13) show that the Mn atoms order relatively easily and only for the AgGa alloys were results for the disordered state obtained for rapidly quenched samples (13). In Fig. (4.6) the extrapolation of T_{d1} and T_{o1} at T=0K correspond to a z value close to 0.19. This value agrees with the nearest neighbour percolation limit for f.c.c. lattice as calculated by various people (10-11). The percolation limit represents Mn concentration below which the remaining manganese ions are too few to support a long range order or freezing through

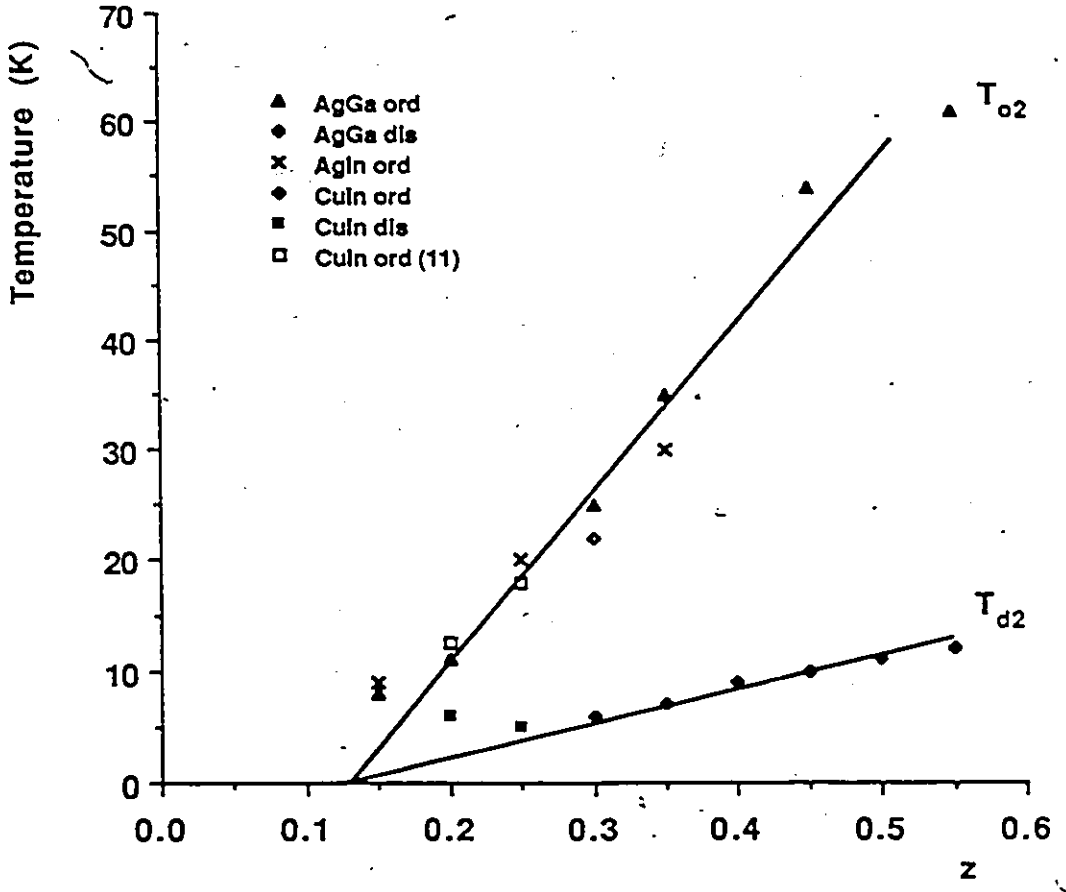

Fig (4.8) Spin glass transition temperature vs z for ordered (T_{o2}) and disordered (T_{d2}) chalcopyrite samples

nearest neighbour interaction only. For chalcopyrite samples the corresponding percolation limit was found to be 0.12.

The Curie-Weiss paramagnetic temperature was obtained for a range of alloys with manganese concentration of $0.1 \leq z \leq 0.65$ by plotting the inverse susceptibility vs temperature and extrapolating the Curie-Weiss line back from high temperature to zero. The variation of θ with manganese concentration for all samples is shown in Fig. (4.9). However, it is to be noted that the value of θ will be the weighted average of those for the ordered and disordered phases and thus the values obtained lie between two limits, the upper corresponding to the crystallographic order of manganese and the lower limit to completely random Mn distribution. It is to be noted that for all cubic samples, the values lie closer to the disordered limit while for chalcopyrite samples, the results lie nearer the ordered limit.

4.4 Analysis

It is observed that in the low temperature magnetic susceptibility measurements, samples with a concentration $0.25 < z < 0.65$ were found to have fairly sharp cusps which have been ascribed to spin glass freezing temperature. Other measurements such as neutron diffraction (26) show that there is no ordered spin arrangement below this critical temperature. At high temperatures, spins of manganese ions interact weakly. This interaction between Mn^{+2} ions is paramagnetic which obeys the Curie-Weiss law and we can see this in the linear variation of χ^{-1} vs T curve.

Turning to the curves of χ^{-1} vs T, since the extrapolation of the linear section of χ^{-1} vs T intersects the negative T axis, one concludes that the interaction between the magnetic ions is antiferromagnetic. Therefore the magnetic susceptibility in the high temperature

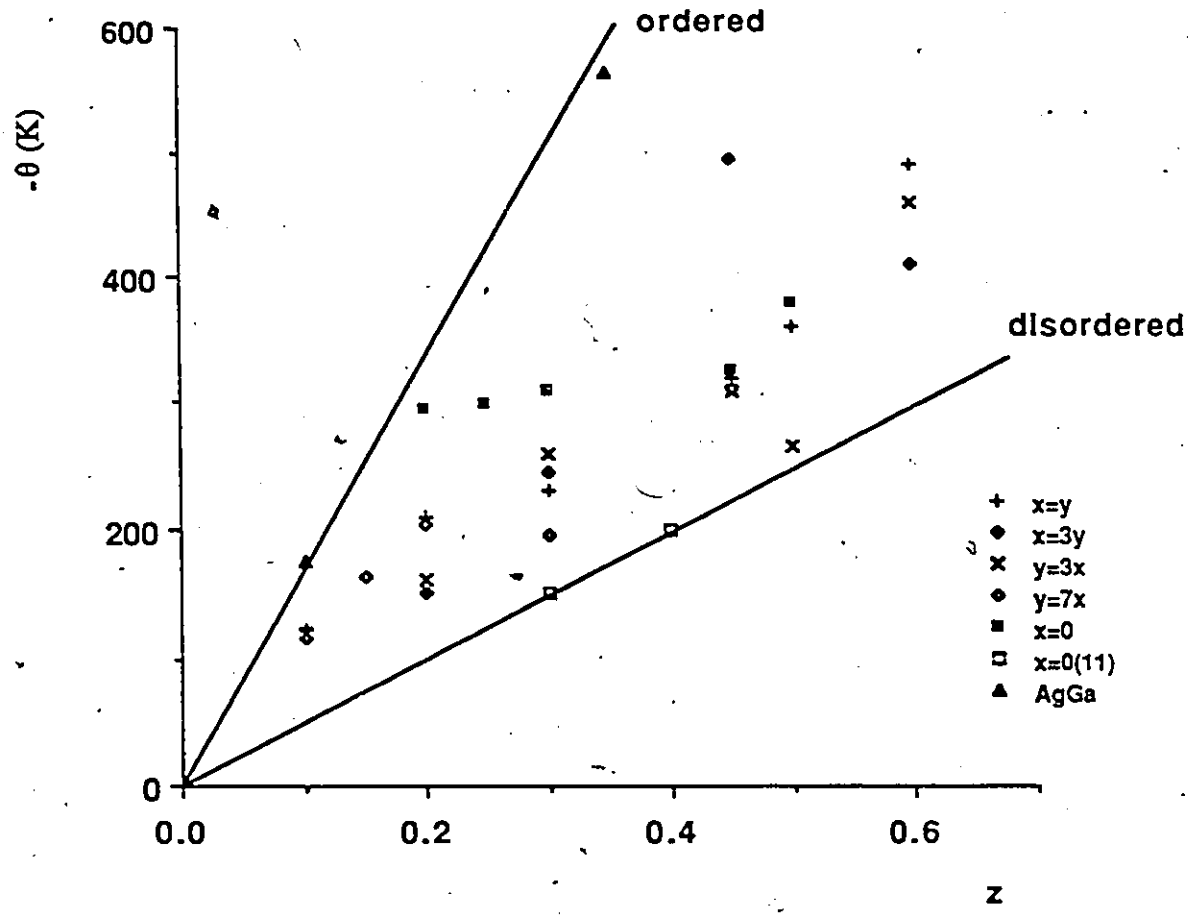

Fig (4.9) Variation of $-\theta$ with z.

The two lines represent the limits of completely ordered and completely disordered systems as described in reference 48.

region can be given by

$$\chi(T)_{\text{per mole}} = \frac{zN_A \mu_B^2 g^2 S(S+1)}{3k(T-\theta)} \qquad (4.9)$$

where z is the manganese concentration , N_A is Avogadro number and θ is negative. As the temperature is lowered, the correlation of the spins tends to align them antiferromagnetically in small clusters for larger time intervals. As the temperature keeps falling, the manganese clusters show greater correlation and longer range of the interaction. As a consequence, the correlation is enhanced at T_g and it becomes infinity. In the range above T_g a superparamagnetic effect occurs and the susceptibility is increased and hence the slope of χ^{-1} vs T changes. As a result, the χ^{-1} curve falls below the Curie-Weiss line which is represented by Fig. (4.4). This downward behavior occurs for the samples with low manganese concentration. The concept of superparamagnetism was suggested by Néel (3-4) which helped to explain some unusual effects seen in rock magnetism. This superparamagnetic effect or enhanced paramagnetism is believed to be due to the presence of uncompensated spins at the surface of the finite independent clusters and also the presence of isolated spins giving a paramagnetic contribution. For samples with higher manganese concentration, the χ^{-1} vs T curve shows an upward deviation and this can be interpreted as follows. Since the manganese concentration is high, it is possible to form bigger Mn clusters. For the large clusters, the ratio of surface to volume is small and this will reduce the number of uncompensated spins relative to small clusters in the samples with lower manganese concentration. As well, the possibility of finding isolated spins will be less and this diminishes the superparamagnetic effect. The spins in these big clusters tend to align

antiferromagnetically for a longer time over a range of temperature and consequently decreases the susceptibility below the Curie-Weiss behavior and hence the upward deviation in the χ^{-1} vs T.

The values and variation of T_g can give insight into the type of exchange interaction occurring between the magnetic ions in these semimagnetic semiconductors alloys. It has been suggested by Escorne et al.(9) that in this type of materials, the exchange integral $J(R_{ij})$ can be expressed in an exponential form

$$J(R_{ij}) = J_O e^{-\alpha R_{ij}} \qquad (4.11)$$

We can expect that the spins will be frozen at a temperature T_g such that

$$A|J(R_O)| \sim k_B T_g \qquad (4.12)$$

where R_o is the mean distance between Mn ions and A is a constant. Considering the mean volume occupied by manganese for a concentration z, the mean exchange interaction between the Mn ions is given by

$$J_m = J_O \exp(-\alpha d z^{-1/3}) \qquad (4.13)$$

In the f.c.c. case, d is related to the lattice parameter a, as $d = a/2^{1/2}$. This leads to the phenomenological law

$$\ln T_g = -\alpha d z^{-1/3} + \ln \frac{-AJ_O}{k} \qquad (4.14)$$

Here the second term on the RHS is obtained by considering eq. (4.12) and the constant A is

positive and z independent. The validity of this relation can be tested by plotting a graph of ln T_g vs $dz^{-1/3}$ using the disordered values of T_g. In Fig. (4.10) the plot of ln T_g vs $dz^{-1/3}$ is illustrated for the present system. The values of d were calculated using the values of lattice parameter obtained from chapter 2. It is seen that the variation is linear within the experimental limits.

Considering the limits of experimental error one can conclude an important feature of this result. The parameter α is a constant independent not only of manganese but also x and y compositions. As we have seen in chapter 3, the energy gap varies with the composition and hence α is independent of energy gap too. The final conclusion that one can obtain is that first of all eq. (4.8) shows that there is an indirect antiferromagnetic exchange interaction between the magnetic ions. This interaction varies with the distance exponentially and is independent of the magnetic ion concentration and hence the other composition dependent parameters.

A mechanism was proposed by Geertsma et al (33) based on the work of Goncalves de Silva and Falicov (32). This is similar in concept to the virtual interband transition model (Bloembergen-Rowland interaction). This virtual transition occurs between the valence band and 3d states in the delocalized band. In the analysis of Geertsma et al, the exchange that takes place can be given in a modified way with an additional R^{-2} factor compare to eq. (4.11)

$$J(R) = I_0 R^{-2} \exp(-\alpha R) \qquad (4.15)$$

with

$$\alpha = 2(2m^{*}\epsilon/\hbar^{2})^{1/2}$$

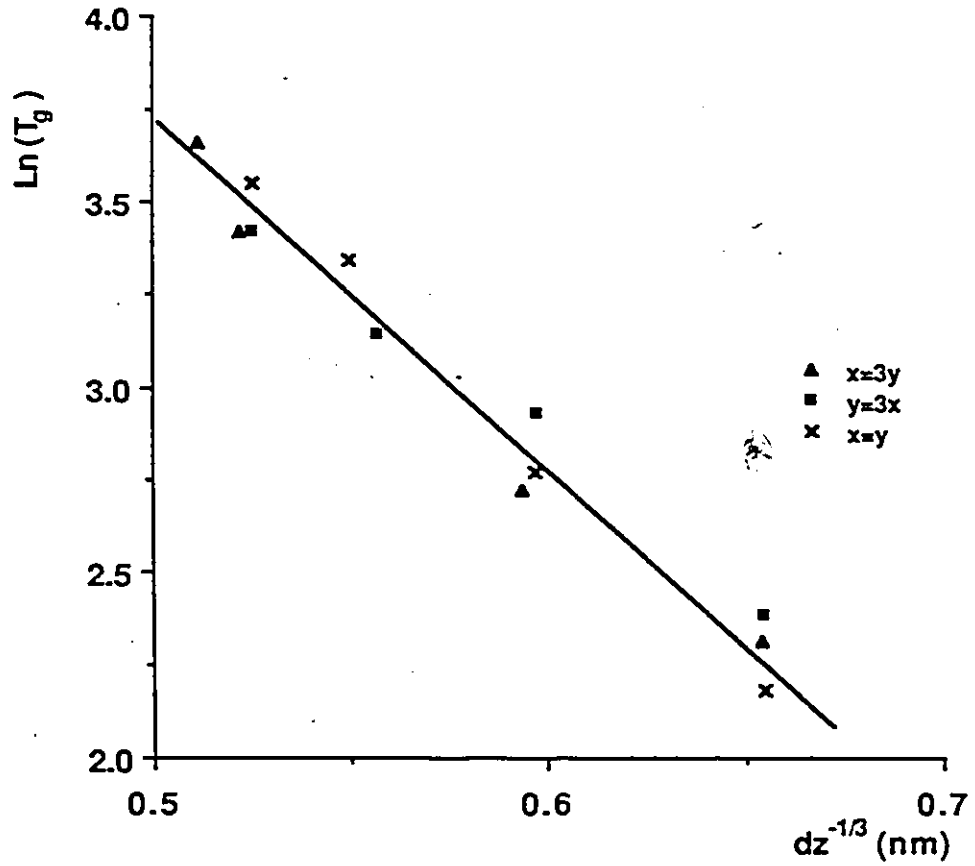

Fig (4:10) Variation of Ln (T_g) with $dz^{-1/3}$ for Disordered Cubic Samples

where m* is the valence band effective mass, ϵ is the energy difference between a full valence band with a Mn $3d^5$ level, and a valence band with a hole along with a $3d^6$ level. The important feature in this exchange interaction is that the exponential term is a function of the effective mass of the valence band and the energy difference ϵ involved in the virtual interaction. Since for the zinc blende and other types of semimagnetic semiconductors the valence band is insensitive to changes in composition, it appears reasonable that this exponent should have a constant value as described above. Thus this exchange would appear to have the form required to explain the present results.

As mentioned earlier, other candidates for the exchange mechanism are direct, RKKY, superexchange and Bloembergen-Rowland. In the present system, the distance between Mn^{2+} are relatively large and to explain the exchange mechanism in spin glass behavior, direct exchange interaction can be eliminated. A low carrier concentration means that the RKKY interaction can also be neglected for the present system. The possible exchange mechanism responsible for the spin glass behavior might be explained by superexchange. The kind of exchange could occur in the presence of materials with anion p orbitals, for example, tellurium. These p electrons of the sp^3 hybridized valence conduction band play a main role in this mechanism. Another interesting model which mainly depends on the energy gap was suggested by Bloembergen and Rowland (30) and is discussed by various other authors (49). This exchange mechanism occurs through a virtual transition from valence band to the conduction band. According to this model, the exchange interaction has an exponential variation with distance given by

$$J(r) \;\alpha\; \exp\{\frac{-2mE_g}{\hbar^2} r\} \qquad (4.16)$$

Here the exponent is a function of the band gap E_g and m is the effective mass at the bottom of the conduction band. However, this model appears to be successful only for the case of low energy gap materials. [Eg. $Hg_{1-z}Mn_zTe$] Because for this case α would not be independent of composition, it appears that this not the dominant mechanism in the present case.

Coming back to the Geertsma analysis, when the additional R^{-2} factor is included in the present analysis, eq. (4.14) can be rewritten as

$$\ln T_g d^2 z^{-2/3} = \ln \frac{-AI_o}{k} - \alpha dz^{-1/3} \qquad (4.17)$$

Fig. (4.11) summarizes the modified Escorne plot of disordered values for $Zn_{2x}(CuIn)_yMn_{2z}Te_2$ alloys. It is found that within the experimental errors the plot shows a linear form. The reason for obtaining a linear variation in Fig. (4.10) and Fig. (4.11) is that d varies only slightly and hence has little effect on the shape of graph. Having plotted the modified Escorne relation, one can calculate the values of α and AI_o/k from the slope and intercept respectively. For disordered zinc blende the following values were obtained.

$$\alpha = 5.62 \pm 0.4 \text{ nm}^{-1}$$

$$\frac{AI_o}{k} = (1.73 \pm 0.5) \times 10^{-2} \text{ Knm}^2$$

It was suggested by Anderson (34) that for antiferromagnetic materials $kT_n = S(S+1)J$, where T_n is the Neel temperature. For alloys we are working on, the interaction is antiferromagnetic, so that the constant A can be replaced by S(S+1) and S can be determined

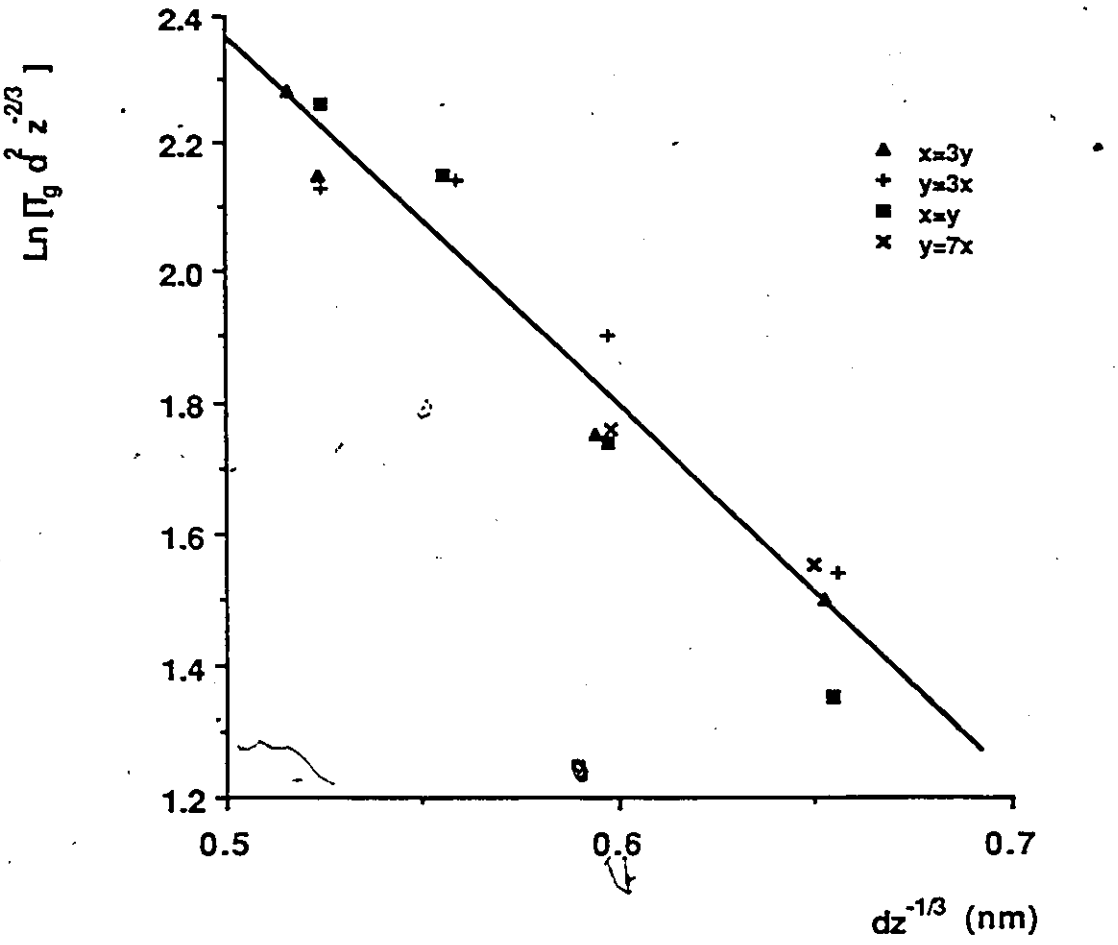

Fig (4.11) Variation of Ln [$T_g d^2 z^{-2/3}$] with $dz^{-1/3}$ for Disordered Cubic Samples

from the slope of the χ^{-1} vs T graph. The value obtained for S was 5/2 for these materials. A value of (19.8 ± 6) Knm^2 was thus obtained for I_o/k. This result is important because it can give useful information about the exchange interaction between nearest and next nearest neighbours (J_1 and J_2) which can be compared with particular values quoted in the literature.

Calculation of J_1/k and J_2/k

For the case of $Zn_{0.95}Mn_{0.05}Se$, the value of J_1/k was found to be -12.7 ± 0.9 K (35) while for $Cd_{0.95}Mn_{0.05}Te$ the values of J_1/k and J_2/k were -6.8 ± 0.4 K and -1.1 ± 0.05 K (35). For the present system, the lattice parameter at z =0.05 and y =0.48, a=0.6159nm gives d = 0.4355nm which is equal to R in eq. (4.15). This gives J_1/k=9.3±0.5 K. For J_2/k, the appropriate R is $\sqrt{2}$d = 0.6159nm and this gives a value of J_2/k = 1.6 ± 0.04 K. It can be seen that the value of J_1/k for the present system is much less than the value of J_1/k for $Zn_{1-z}Mn_zSe$ and greater than the value of J_1/k for $Cd_{1-z}Mn_zTe$ and this is prabably due to the lattice parameter. In $Zn_{2x}(CuIn)_yMn_{2z}Te_2$, the lattice parameters are less than the lattice parameters in $Cd_{1-z}Mn_zTe$ and greater than the values in $Zn_{1-z}Mn_zSe$. Some errors in the present values for J_1/k may occur due to the experimental scatter in the plot of $\ln T_g dz^{-2/3}$ vs $dz^{-1/3}$.

4.5 Discussion

The magnetic susceptibility measurements and results deduced from them have proved to be very useful in giving valuable information on the magnetic behavior of the $Zn_{2x}(CuIn)_yMn_{2z}Te_2$ alloys and hence all the materials belonging to the same group. When the curves of magnetic susceptibility χ vs temperature were studied, it was seen that for all cases the cusp corresponding to the transition temperature was observed. For some cases it is seen that a second peak was found. As mentioned earlier, the amplitude of these peaks depend on the cooling process. It is seen that (48), if the sample is quenched from annealing temperature in water, then both peaks can be seen. If the sample is left in the furnace and the furnace is switched off so that cooling to room temperature took several hours then only the higher temperature peak could be seen. It was found that the ESR curve was more sensitive to the presence of two phases and this will be discussed in detail in chapter 5.

Despite magnetic effects mentioned above, the x-ray powder photographs showed the presence of a single cubic or chalcopyrite phase in each case. Because of this, and bearing in mind, the faint ordering lines observed in some alloy systems (11) it would seem that the difference between the two phases observed correspond to the crystallographic order or disorder of the Mn atoms on the appropriate lattice. This effect of cooling rate indicates that the low transition temperature corresponds to the disordered T_d and the higher to the ordered state T_o. It is seen that all these values of transition temperature fall into four sets, T_{d1} and T_{o1} for the zinc blende and T_{d2} and T_{o2} for the chalcopyrite.

For $(CuIn)_{1-z}Mn_{2z}Te_2$ alloys, the structure changes to cubic from chalcopyrite at

0.27 and this change is observed in the T_o values. The values of transition temperature T_{d1} obtained for cubic structure is higher than that of T_{d2}. The results indicate that for both the chalcopyrite and cubic materials at high temperatures, the manganese atoms are distributed at random on the cation sites. Strictly speaking,of course,in the ordered case the Mn atoms will still be arranged at random but on a particular sub-lattice of the cation sites. So perhaps the term used should be partially ordered. To consider what the ordered structure might be, looking firstly at the cubic case, the relative value of T_d and T_o would indicate a different structure consistent with the ordering lines in the $Cd_{2x}(AgIn)_yMn_{2z}Te_2$ (11) alloys. A slight distortion along a preferred [111] axis has been reported (36) for $Cd_{1-z}Mn_zTe$ alloys resulting in trigonal symmetry. Such trigonal behavior in the present cubic alloys could result in Mn ordering and be responsible for the T_{o1} values observed. No analysis of these ordered structure has been completed at present but neutron diffraction measurements are planned. For the chalcopyrite case, the value of z for a given value of T_g (T_o or T_d) tend to indicate that the Mn atoms occupy one half of the cation lattice sites. Since no extra ordering lines have been observed, one obvious possibility is that Mn occupy only the I or III sub-lattice, the displaced atoms entering the other sub-lattice. The effective density of Mn on the particular sub-lattice would then be 2z and could account for the larger transition temperature. The question of lattice frustration and hence spin glass behavior is involved here as can be seen in Fig. (4.12). If the Mn enter all cation sites, the usual face centered cubic lattice frustration occurs and a spin glass results. However from Fig. (4.12) if all Mn atoms enter, say the III sub-lattice , no frustration condition occurs, and hence an antiferromagnetic ordering could exist , consistent with the comments above.

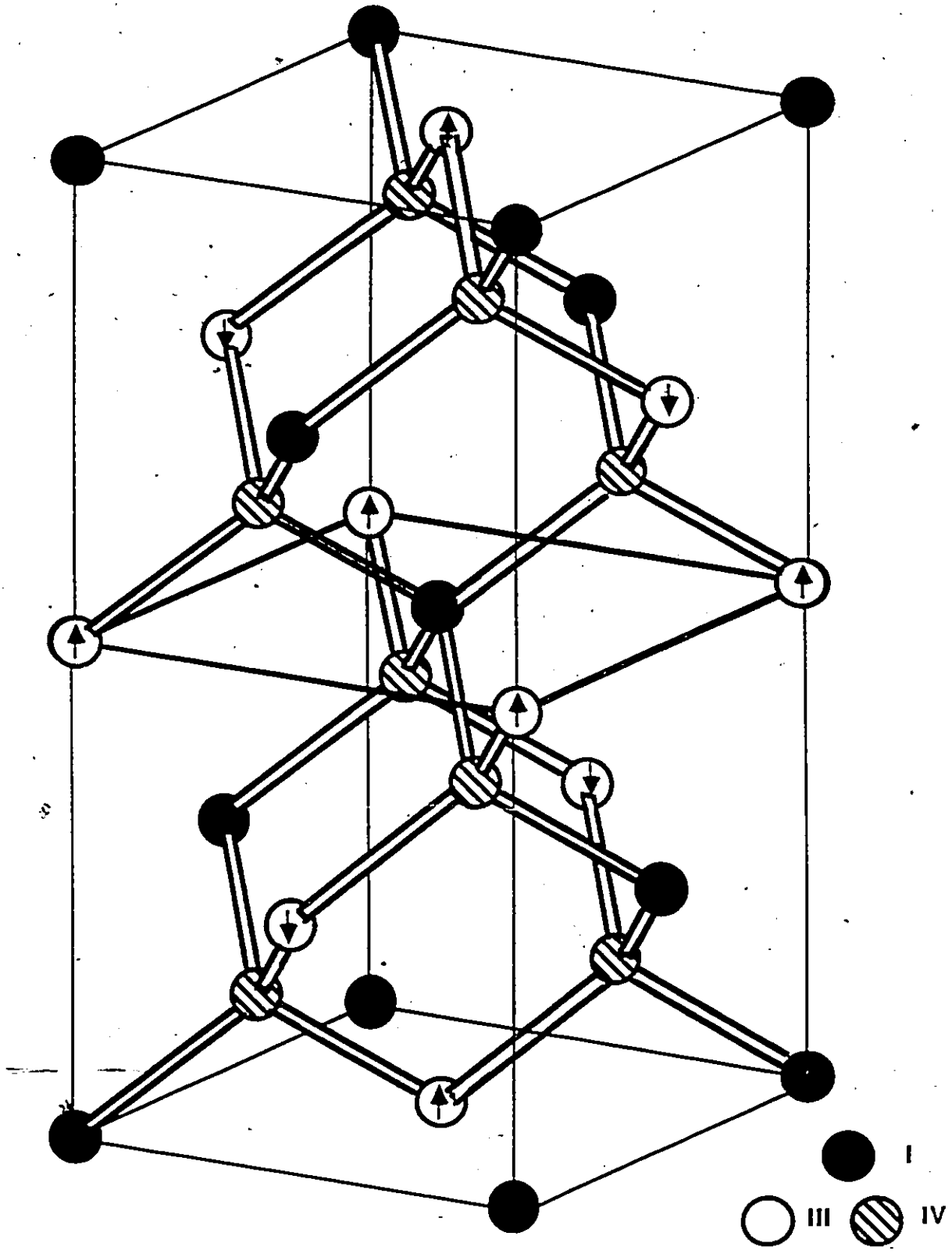

Fig (4.12) Chalcopyrite structure showing the constituent sublattices and possible Mn spin alignment assuming all the Mn atoms go to one cation site.

Chapter 5

Electron Spin Resonance

5.1 Introdution

Consider a free ion with a permanant magnetic moment. If this ion has a resultant angular momentum quantum number J, which is the vectorial combination of angular momentum L and spin quantum number S, the application of a static field will split this level into $2J + 1$ levels. The effect is known as Zeeman splitting and these levels have the energy of $M_J g\mu_B H$. Here M_J is the magnetic quantum number, g is the splitting factor given by the Lande' formulae eq. (4.2). If the ion forms part of a crystalline solid and is not free, the spin quantum number S can be used to describe its angular momentum. Then the application of a field H will produce a splitting of the 2S + 1 levels with the energy of $M_S g\mu_B H$. This is the same as above except g is the splitting factor that makes the energy difference between levels come out correctly. Since the crystalline field has an effect on the orbital angular momentum of the ion, the g value is different from the Lande value. According to Quantum Mechanics, a selection rule operates so that for magnetic dipole radiation only the transition between adjacent levels for which $\Delta M_S = \pm 1$ are possible. Transitions between levels can be induced by the application of an electromagnetic oscillating field whose frequency ω is

$$\hbar\omega = -g\mu_B H \qquad (5.1)$$

$$\text{or} \quad \omega = \frac{ge}{2mc} H \qquad (5.2)$$

The eq. (5.2) is same as the equation that represents Larmor frequency (22) including the additional g factor due to the effect of the spin. If a system of ions are at thermal equilibrium, the greatest population will occur in the lowest energy state. Consequently even though individual transitions for absorption or emission have the same probability, there is a net absorption of energy from the radiation field that can be observed experimentally. This can be illustrated for the simplest system with two Zeeman levels. Transitions between these two levels can be induced by a magnetic field of the appropriate frequency ω. If the photon energy $h\omega$ matches the energy level separation, then eq. (5.1) meets the resonance condition and this is shown in Fiq. (5.1) where H_r is the magnetic field at which the resonance condition is met. Since the absorption occurs only for the frequencies at or near the Larmor frequency, the phenomenon is called paramagnetic resonance or electron spin resonance (ESR).

Electron spin resonance has been found to be a very useful technique to study spin-spin interaction as well as different relaxation processes such as exchange interaction. These interesting properties can be observed by studying the position as well as the width of the resonance line. Also the kind of information described above are revealed by the change of the position or the width of the resonance line when the temperature is changed. From eq. (5.1) one may infer that there are two approaches to the detection of resonant absorption by a paramagnetic sample. In the first case the separation of the Zeeman levels is fixed by holding the magnetic field constant. The microwave frequency is then varied until a resonant absorption is found. In the second case, the microwave frequency is fixed and the magnetic field is then varied. Since the radiation sources are operated only over a limited frequency range, it is customary to carry out paramagnetic resonance experiments at a fixed

frequency and by varying the magnetic field. For the alloy systems being investigated in our research group, J = S and g can be considered to be close to 2 (the ground state for Mn^{2+} is a S state with L = 0). Using these results one can illustrate the splitting situation as in Fig. (5.2). In this illustration, since the selection rules are such that only transitions between adjacent levels are allowed, a single resonance can be observed.

As mentioned before, the general effect of the crystalline field is to cause some shifting of degenerate levels. This can be explained as follows. The ground state of the free ion Mn^{2+} is sixfold degenerate which is given by (2S+1)(2L+1) = (2.5/2+1)(0+1) = 6 the classification being $\{^6S_{5/2}\}$. If such an ion is placed in a crystal environment, the electron paramagnetic resonance of the system shows that, because of the environment, the free ion ground state sixfold splits into two levels, the upper fourfold degenerate and the lower twofold degenerate. In the presence of a magnetic field , the Zeeman interaction lifts the degeneracy of the quartet and the doublet. Therefore, instead of a resonant line, multiple resonance points will occur resulting in the observation of more than one line. The fine structure splitting in a cubic crystal field plus an external magnetic field is illustrated in Fig. (5.3).

The first additional interaction to be considered is that of the electron spin magnetic dipole with nuclei in its vicinity since these nuclei possess an intrinsic spin angular momentum. The spin quantum number I of these magnetic nuclei takes one of the values 1/2, 1, 3/2,2.....etc. with a corresponding multiplicity of nuclear spin states given by (2I+1). For example, nearly all Mn^{2+} isotopes have nuclear spin I = 5/2. The interaction of an unpaired electron and a magnetic nucleus is called nuclear hyperfine interaction. The term hyperfine splitting was used in atomic spectra to designate the splitting of certain lines which is given by (2I+1) as a result of interaction with magnetic nuclei. The splitting of the

$M_S = 1/2 \rightarrow -1/2$ fine structure line, for example, is shown in Fig. (5.4).

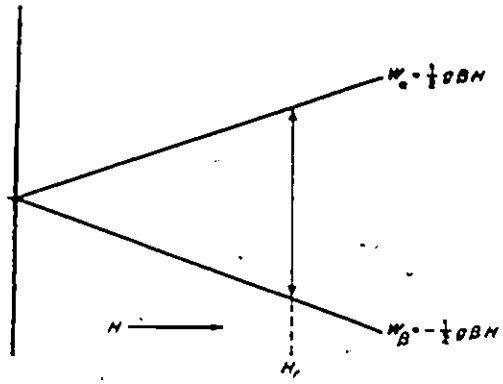

Fig (5.1) Energy Level Scheme for the simplest system showing ESR Absorption

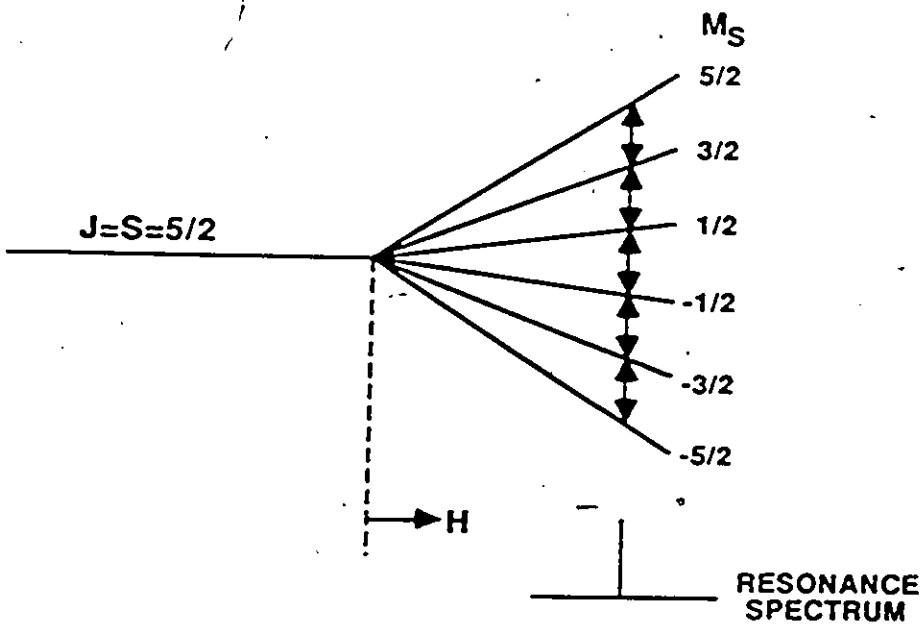

Fig (5.2) Zeeman Splitting of a $3d^5$ Level. In this example there is only one resonance line

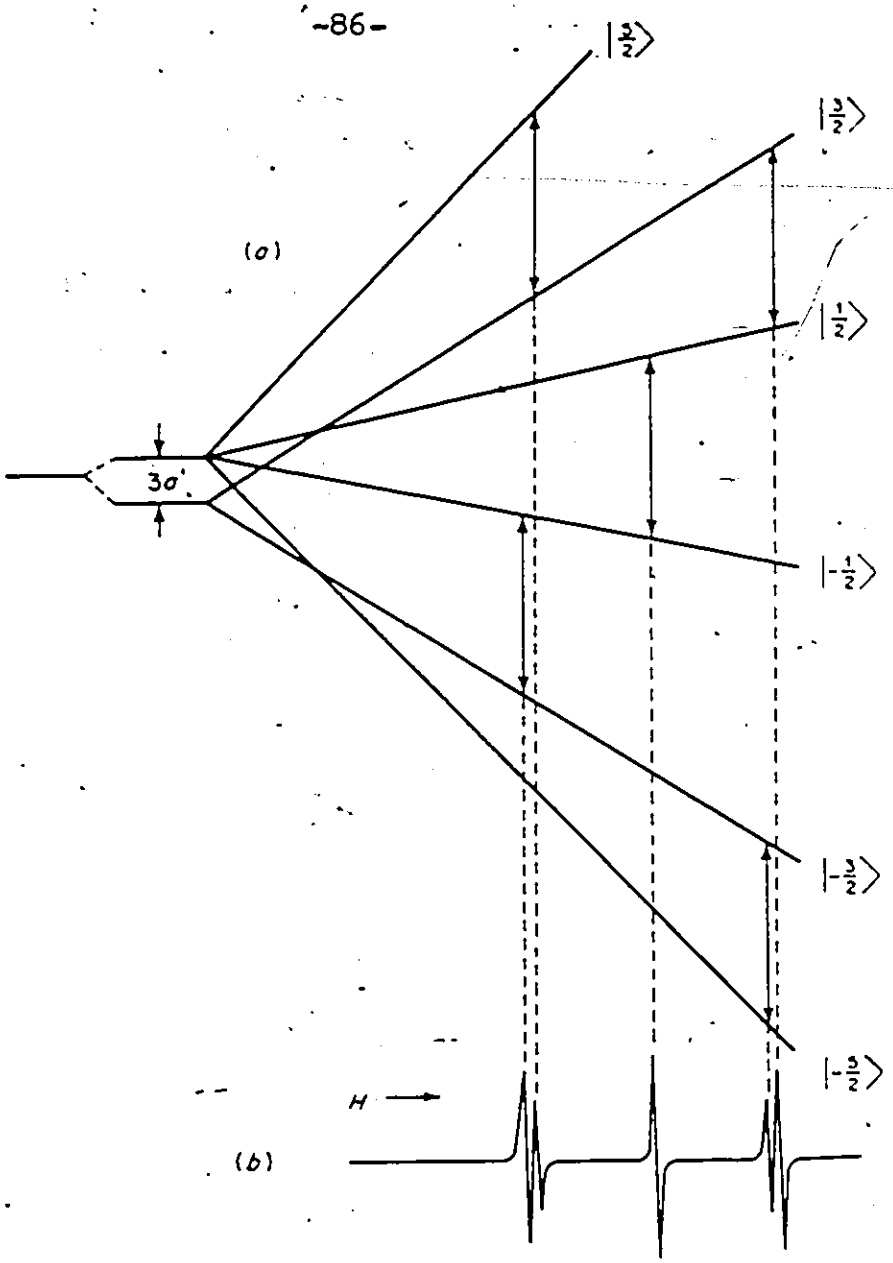

Fig (5.3) (a) Energy Level Diagram for a $3d^5$ Ion in Crystal Field
(b) The Allowed ESR Spectrum

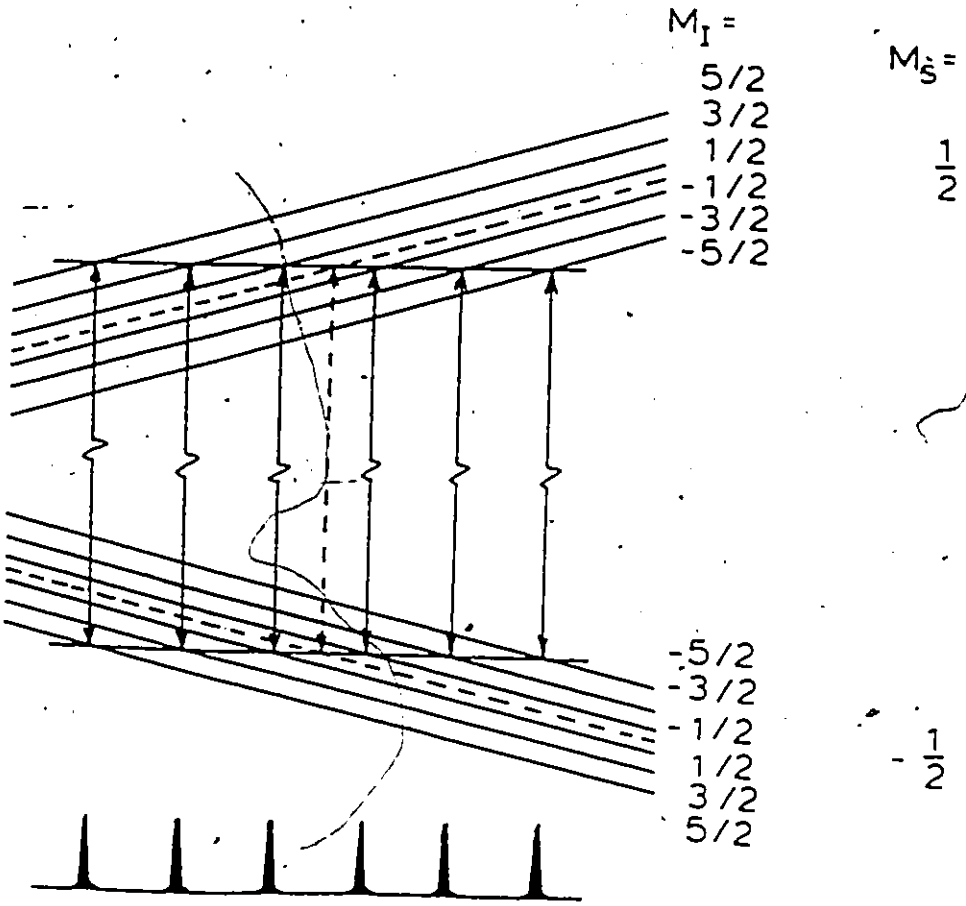

Fig (5.4) Hyperfine Splitting of the $M_S = 1/2 \rightarrow -1/2$ Fine Structure ESR Line of Mn^{+2}

According to the theory suggested by Abragam and Bleaney (38) the g value of free spin is very close to the free spin value of 2.0023. To a good approximation the g value would be the same for the free ion and the expected deviation Δg is only about 0.0004. This is confirmed by Watanabe (39) and experimentally the g value of Mn^{2+} was found to be , to a good approximation, the same as that of the free ion. Paramagnetic resonance absorption experiments were carried out on CdTe containing about 0.01% Mn^{2+} (40). In this system, the resonance lines were found at 4.2 K for the transition $M_S = 1/2 \rightarrow -1/2$. The g value obtainedwas 2.010 which is close to the value for the free ion. The ESR spectra of single crystal $Cd_{1-z}Mn_zTe$ has been studied by Oseroff (41). For a concentration $z \leq 0.005$ and at room temperature, a well-separated hyperfine structure was observed. Also, for the extended concentration range $0.005 \leq z \leq 0.6$, as the concentration was increased beyond $z \leq 0.005$, the hyperfine lines initially broadens due to the dipole-dipole interaction, eventually becoming a single broad line. Then the line narrows with further increase in z due to exchange narrowing via a short-range exchange interaction with the minimum line width corresponding to $z = 0.05$. For $z \geq 0.05$, the single line broadens monotonically with increasing concentration. These experiments were extended to $Cd_{1-z}Mn_zSe$ ($0.001 \leq z \leq 0.45$) as a function of magnetic field, temperature microwave frequency, etc. (8). Not only was a broadening and shift in the magnetic field of the electron paramagnetic resonance line with decreasing temperature was observed but also it was found to be independent of microwave frequency.

Generally the absorption does not occur at a sharply defined magnetic field. Instead it is spread out over a range H. The size of the spread or the linewidth ΔH may be due to various effects such as spin-spin interaction, exchange interaction. Another factor that may effect this linewidth ΔH is inhomogeneous broadening.

5.2 Experimental Procedure

The experimental set up that has been used for the ESR measurements is illustrated in Fig. (5.5). The main part of the spectrometer system is the Klystron which produces the microwave power at x-band frequency (9.2GHz) with the application of the appropriate voltage. The microwave bridge which is known as a 'magic T' is a four armed waveguide structure which allows the microwave power to feed into the sample cavity through one arm and the power reflected from the sample cavity travel through to the detection system. The power entering the detection system is controlled by the arm opposite the sample cavity. The sidescrew turner contains a pin which can be inserted into the path of the microwave, and can also be moved along the length of the waveguide comprising the sidescrew turner. An attenuator is attached to the end of this arm with a mica card. This card is covered with carbon so that it absorbs nearly all the microwave power reaching the attenuator. The amplitude of the microwave can be changed by the pin depth and the position of the pin along the turner changes the microwave phase. The isolators consist of ferrite magnets which allow the microwave to travel in only one direction and hence any reflection in the bridge system cannot pass them. In the waveguide, a crystal detector with a silicon rectifier detects the high frequency microwave power and changes it to direct current voltage. However, lower frequencies up to about several tens of megahertz are able to travel through the rectifier without being changed to direct current.

The microwave resonant cavity is a waveguide with two copper plates soldered on each end. One of these plates has a hole of 1/4" dia. in the center which allows the microwave to enter the cavity. In practice, the length of the cavity is taken to be one or two wavelengths. A phase sensitive detector (PSD) is employed and the signals are recorded on a chart recorder. The PSD produces the derivative of the ESR absorption lines on the chart recorder. The magnetic field is modulated at 200Hz by a signal obtained from the PSD and

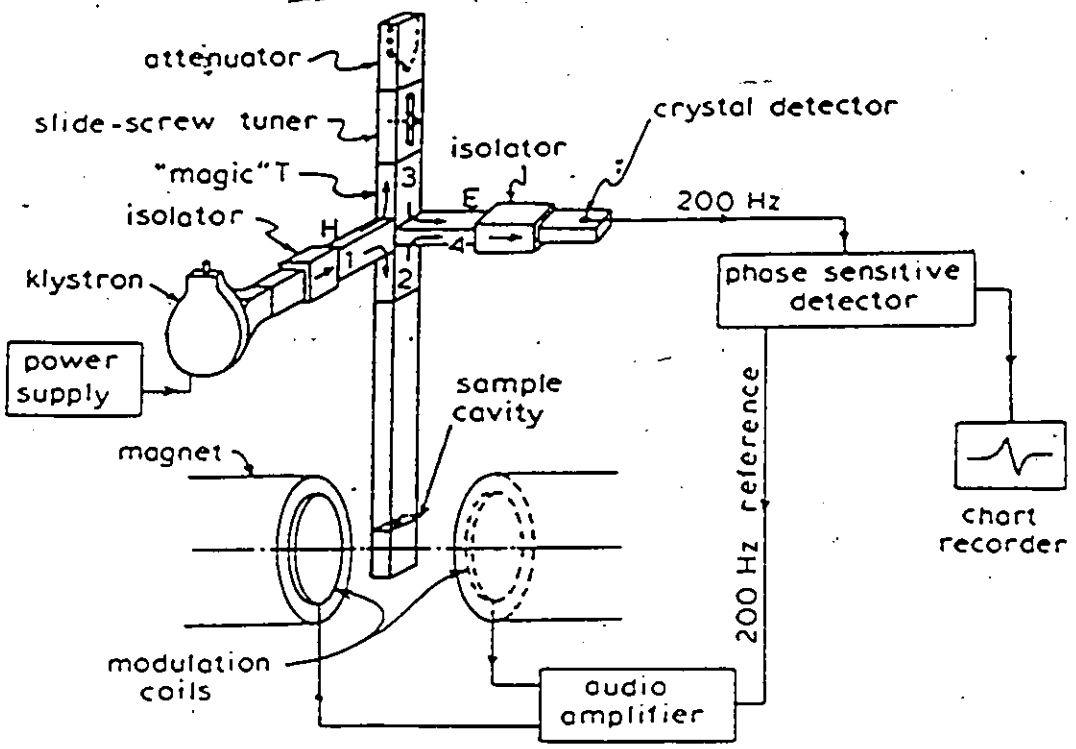

Fig (5.5) Electron Spin Resonance Spectrometer system.

then applied to a pair of Helmholtz coils mounted on the magnetic pole pieces. The derivative of the ESR absorption line is then produced on the chart recorder, and the peak to peak linewidth ΔH is measured with an NMR gaussmeter. The resonance field H_r is defined from the zero of the derivative curve and this is shown in Fig. (5.6).

The temperature of the sample is measured by a thermocouple which is in contact directly with the sample. The temperature below 300 K is measured by a gold-chromel thermocouple while the temperature above 300 K is measured by a copper-constantan thermocouple. Thus ESR measurements can be carried out at various temperatures. The samples used for the ESR measurements were in powdered form. For each sample, about 0.05g was required and thin glass tube was used to hold the sample inside the sample cavity.

5.3 Background to ESR in SMSC

ESR measurements were carried out on the alloy systems being investigated by the research group (10-14) in single phase regions. At room temperature all samples produced a single symmetric , broad line due to the manganese atoms. The broadening of the ESR line was proportional to the manganese concentration. The resonance field H_r was observed to be consistent with a g value of 2.0. The resonance linewidth ΔH, which is the linewidth of peak to peak of the derivative curve was measured as a function of temperature within the interval 10 to 500 K. In all cases, the linewidth increased with decreasing temperature. The results of the alloy systems $Cd_xZn_yMn_zTe$, $Cd_xZn_yMn_zSe$ etc., studied by other members (10-14) of the group, show that the shape of the resonance lines remained symmetrical at the higher temperatures. But at lower temperatures, where ΔH started to increase appreciably, the line shape was observed to broaden asymmetrically. In some cases, the line

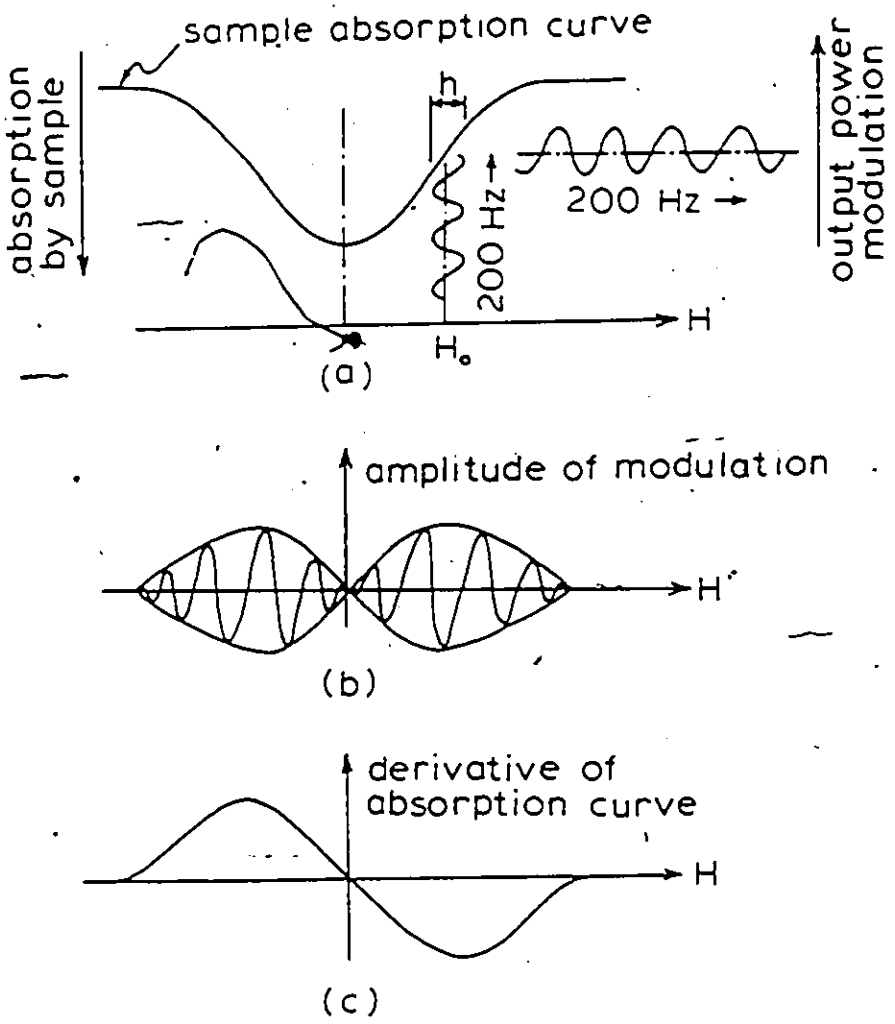

Fig. (5.6) Effect of the modulation on ESR absorption line.
(a) shows that the 200 KHz modulation field causes the microwave power in the cavity to be modulated at the same frequency when the sample absorbs power at resonance. As the steady field H is slowly swept through the absorption curve the amplitude of the modulation of the microwave power changes in proportion to the absorption curve as shown in (b). The modulated microwave power travels from the cavity to the crystal detector where it is demodulated and the 200 kHz signal passes to the PSD (Phase Sensitive Detector). The output signal from the PSD gives the first derivative pattern of the line on the chart recorder as shown in (c).

eventually split into two parts. The splitting of the line at low temperatures is similar to the behavior found by Searl et al. (42) on polycrystalline samples with uniaxial g value anisotropy.

When the variation of the linewidth ΔH with temperature was considered, it was noticed that there were a number of difficulties in the attempts to fit the experimental data of ΔH vs T to an expression which had a physical significance. This is because there has not been any theory developed yet for the interpretation of the dependence of the ESR linewidth with temperature for this class of materials. At first, the method used by Oseroff in his ESR work on $Cd_{1-z}Mn_zTe$ (41), where he analysed the ESR linewidth values in terms of Huber's expression, was used. This was developed for antiferromagnetics above the Neel-temperature, and ΔH is given by the equation

$$\Delta H = A\left[\frac{T_g}{T - T_g}\right]^{\alpha} + B \qquad (5.3)$$

where A is an empirical parameter, α the critical exponent, T_g the transition temperature and B is the high temperature linewidth taken to be constant. The main problem with this analysis was that even at temperatures well above T_g the line width ΔH continued to decrease with increasing temperature. To allow for this effect, the behavior of some alloy systems such as $Cd_{1-z}Mn_zTe$ and $Cd_{1-z}Mn_zSe$ have been analysed as a critical phenomena near the spin glass temperature by Oseroff et al (8-9) using the expression

$$\Delta H = A\left\{\frac{T_g}{T - T_g}\right\}^{\alpha} + B\left\{1 - \frac{\theta}{T}\right\} \qquad (5.4)$$

where the term $B\{1 - \theta/T\}$ represents a paramagnetic contribution to ΔH. Again A and B

are independent of temperature, T_g and θ the quantities discussed in the previous chapter and α the critical exponent. However, this analysis was not satisfactory for these materials because the results obtained for A and B and α suffered from an inconsistent variation with composition. Therefore, to analyse the behavior of the linewidth with the temperature, another approach was suggested by Bhagat et al.(43) and applied to the $Cd_{1-z}Mn_zTe$ alloy system by Webb et al.(44) and by Sayad et al.(45). The broadening mechanism considered in their work was attributed to an inhomogeneous distribution of local fields. For a periodic distribution of Mn in a lattice, each spin experiences the same local field. Diluting the lattice even by a small amount and hence producing a random distribution produced a shift and broadening of this distribution. As a consequence of the local field distribution, the spins do not experience the same field and so possess different resonance points. Therefore rather than getting one resonance line, a distribution of all the individual lines of resonance about the central point was obtained. This was known as an inhomogeneous distribution of local fields.

Through numerical calculations and modifications it was concluded (10-14) that the linewidth variation may be empirically described by the following equation

$$\Delta H = \Gamma \exp\{-\frac{T}{T_o}\} + \Gamma_o \qquad (5.5)$$

where Γ and T_o are empirical parameters associated with the freezing of the spins and the constant Γ_o is the high temperature linewidth. In the above equation, the first term indicated the inhomogenity effect while the second term represented a constant high temperature linewidth. Previous work (10-14) indicated that the high temperature

linewidth may be described by the paramagnetic term in eq. (5.4) which was $B\{1 - \theta/T\}$ rather than by a constant. However, in some cases because of its form, the paramagnetic term was found to overestimate its contribution, so that the rapid increase in linewidth appeared to be dominated by this term rather than by the exponential. As the temperature is lowered the number of free spins decreases because of the freezing process. Since the paramagnetic contribution is due to these free spins, eq. (5.5) should be modified so that it reflects this loss of spins. The final equation was then (10-14)

$$\Delta H = \Gamma \exp\{-\frac{T}{T_o}\} + B\{1-\frac{\theta}{T}\}\{1-\exp[-\frac{T}{T_o}]\} \qquad (5.6)$$

It was found that the way these parameters varied with composition seems to agree fairly well with their physical interpretation (10-14).

5.4 Results and the Discussion of the Present System

The linewidth ΔH of the Mn^{2+} resonance line with g = 2.0 was measured as a function of temperature in the range 10 to 500 K, at X band microwave frequency (~9.4 GHz). The first derivative pattern of the resonance line was recorded and the peak to peak linewidth ΔH measured with a gauss meter. From the variation of ΔH with the temperature, it was found that instead of obtaining one line, two lines, one broad and one narrow, were obtained. Fig.(5.7) shows the variation of the derivative spectrum with temperature for the sample x=3y, z=0.6 for the present system. Also for $Cd_{2x}(CuGa)_yMn_{2z}Te_2$ (12) and $Cd_{2x}(AgGa)_yMn_{2z}Te_2$ (13), similar results were obtained but in these cases the two lines are much better defined. For example, Fig.(5.8) shows the variation of the derivative spectrum with temperature for the chalcopyrite $Cd_{2x}(AgGa)_yMn_{2z}Te_2$ with z = 0.25 (13). These ESR results confirm the presence of the two phases, one disordered and one ordered,

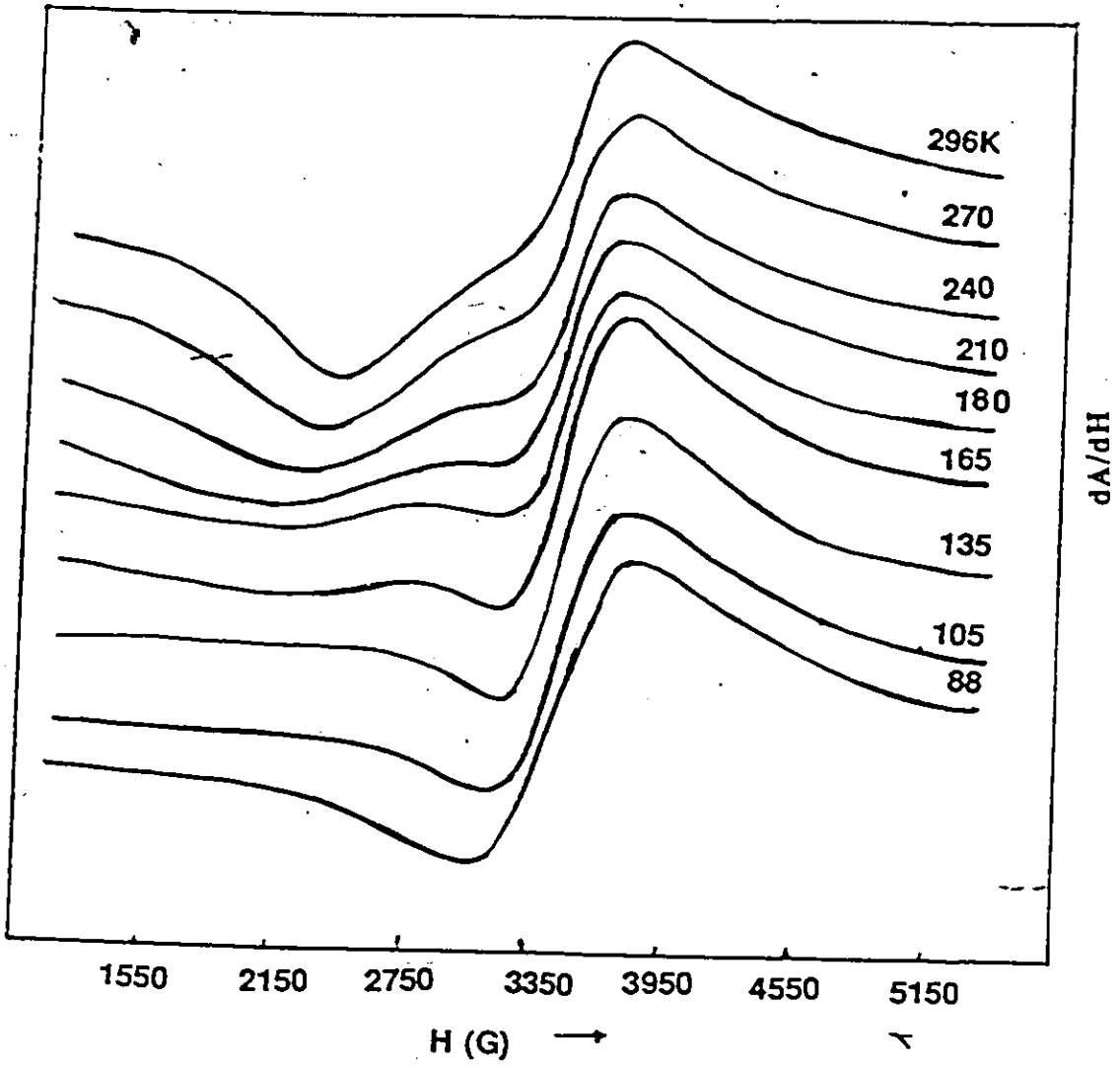

Fig (5.7) Temperature Dependence of the ESR Spectrum for the Sample x=3y, z=0.6.

dA/dH is the field derivative of the absorption.

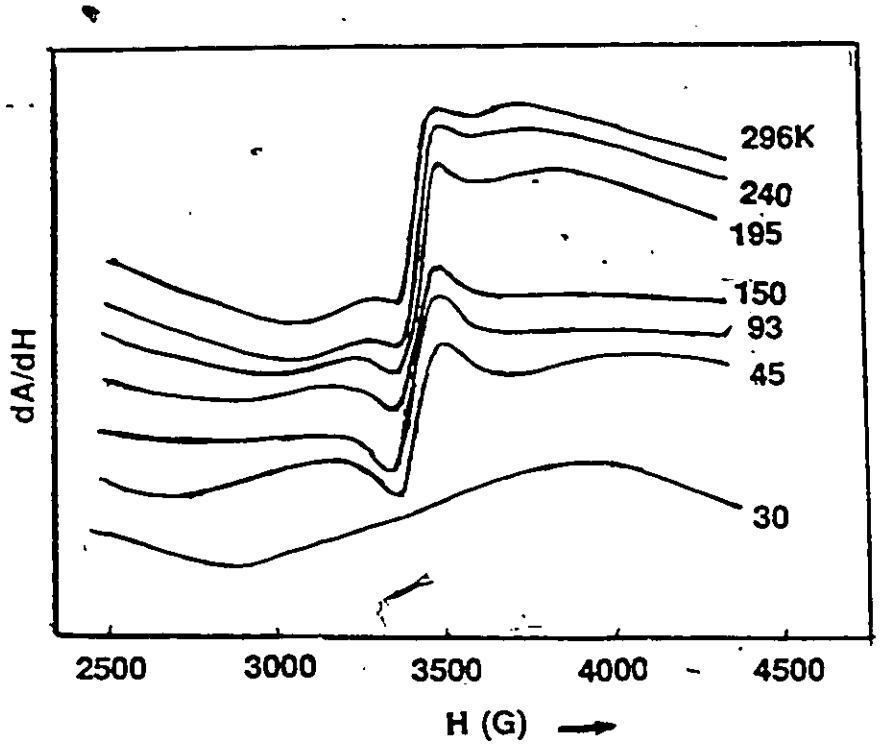

Fig (5.8) Temperature dependence of the ESR spectrum for the sample $(AgGa)_{1-z}Mn_{2z}Te_2$ with z=0.25

dA/dH is the field derivative of the absorption.

obtained in the magnetic susceptibility measurements. Also comparison with the susceptibility. measurements indicates that the broad line is from the disordered and the narrow line is from the ordered structure. Because of the presence of the mixture of the two phases, ΔH cannot be measured by taking the peak to peak line width especially for the disordered phase because, in most cases, only one of the peaks can be seen. Therefore because of the occurrence of the mixture of two phases, the normal analysis used by the members (10-14) of the research group for alloys which did not order, eg. $Cd_xZn_yMn_zTe$ (10) could not be applied for the present system. In most cases, the direct spectrum of ESR for ordered and disordered interfere with each other and thus the derivatives also interfere with one another. Therefore, in the general case it was not possible to determine the line width ΔH_o and ΔH_d separately. However, for a few samples, these values of ΔH_o and ΔH_d were sufficiently different that the effects of the two lines one upon the other could be considered negligible. In these cases, the variation of ΔH_o and ΔH_d corresponding to the ordered and disordered phases with the temperature could then be found. Typical resulting graphs of ΔH_o and ΔH_d vs T are shown in Fig. (5.9). The two curves are seen to be very different. ΔH_d starts at a high value and increases relatively slowly at temperatures well above T_d. This behavior is typical of that observed with a spin glass material where the value of ΔH is determined mainly by spatial inhomogeneity of the local fields seen by the manganese atoms and is almost independent of the critical phenomena at T_d. Thus it appears that the disordered state has a spin glass transition temperature $T_g = T_d$. However, the ΔH_o curve shows a low almost constant value until the temperature comes to a value T_a which is $T_a < T_o$ and then the value of ΔH_o increases rapidly and asymptotically. Earlier it

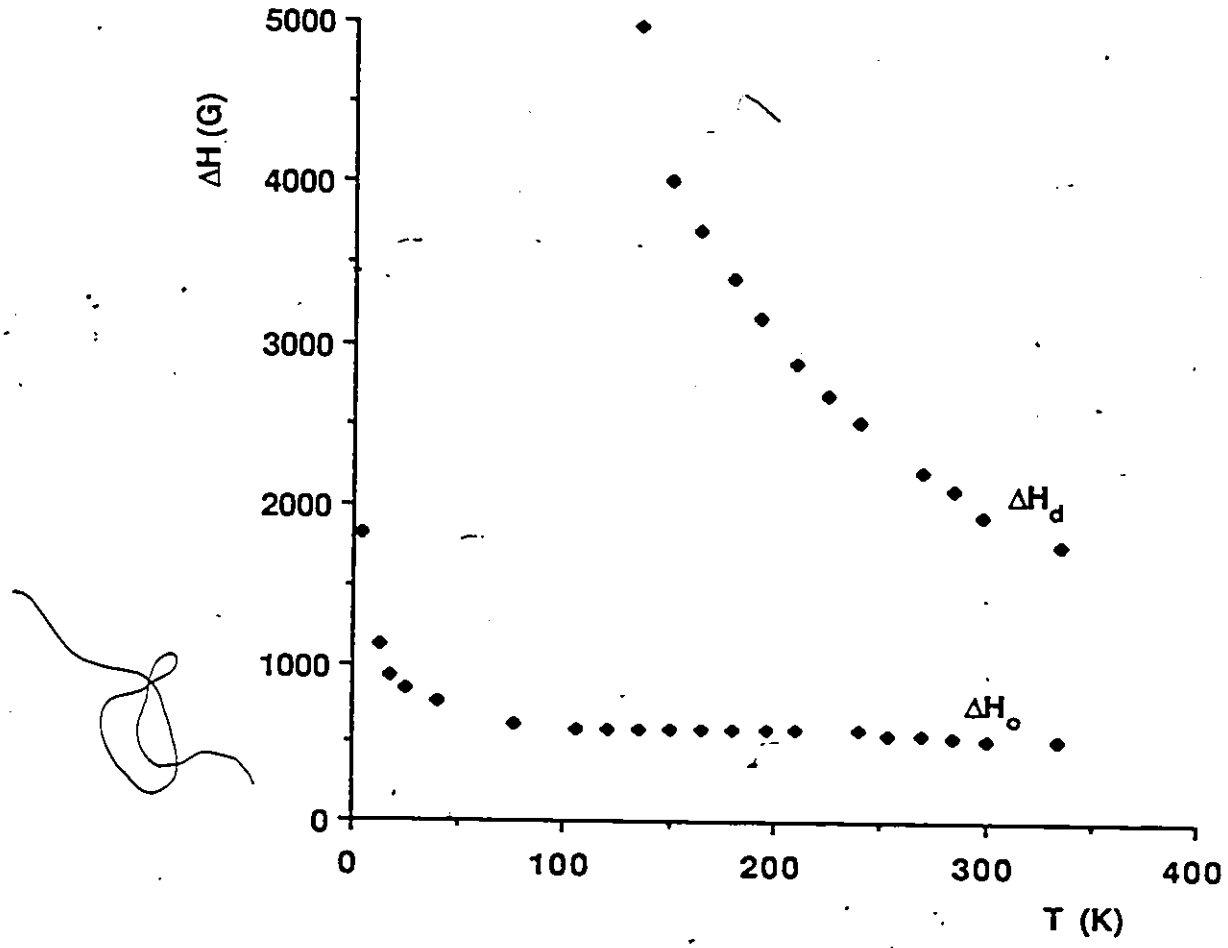

Fig (5.9) Temperature dependence of the ESR linewidth ΔH of the two spectral lines for sample y=3x, z=0.4.

was assumed that the form of ΔH_o was typical of antiferromagnetic behavior, i.e. the ordered structure appeared to show an antiferromagnetic Neel temperature $T_N = T_a$. However, the present results indicate that the behavior is not typically antiferromagnetic . A detailed investigation of the behavior of the ordered structure in this range would require completely ordered samples. However, no analysis of this ordered structure has been completed at present but further experimental work such as neutron diffraction etc. will be continued by other members in the research group (46-47).

Chapter 6

Conclusions

An investigation of some of the properties of the pseudo ternary alloy system $Zn_{2x}(CuIn)_yMn_{2z}Te_2$ which belongs to the group of materials known as semimagnetic semiconductors has been presented. Four main types of measurements were performed on these alloys; the determination of the lattice parameters, energy gaps, magnetic susceptibilities and ESR line width.

In chapter 2, the basic requirements of investigating the phase diagram of the ternary alloy system including the study of the variation of the lattice parameter with the composition is indicated. It has been shown that the lattice parameters vary smoothly with the composition. The limit of solid solution was found to vary from $z = 0.76$ to $z = 0.62$ as (CuIn) was substituted for Zn in the crystal lattice. The chalcopyrite structure existed up to $z= 0.27$ on $x=0$ line where the equilibrium structure became cubic before the solubility limit was reached. The boundaries of the single, two phase and chalcopyrite phase fields which are displayed by the present system were found to be, to some extent, dependent on the annealing temperature. The variation of the lattice parameter values of the single cubic phase with composition was fitted to a suitable empirical equation and from the fitted parameters contours of constant lattice parameters were drawn.

One other measurement which has been made and which shows the effect of ordered and disordered in the lattice is that the room temperature optical energy gap E_g. Values of energy gap and its dependence on the composition were determined. This was done by using the absorption technique as indicated in chapter 3. Over most of the range, E_g shows

a linear increase when the Mn concentration is increased. It is found that the value of the optical energy gap E_g and its variation with composition depend upon the structure concerned. These energy gap values have been attributed to different structures since the aiming points at z=1 were 1.33eV for chalcopyrite range, 1.9eV for the ordered cubic and 2.83eV for disordered range. Finally the variation of the parameter E_g with composition in the ordered field is fitted to a suitable empirical equation and from the fitted parameters contours of constant E_g were drawn. For the disordered field, a few contours of E_g were estimated because of the complicated variation of the energy gap with the composition and in the chalcopyrite range no contours were drawn because of the insufficient data in that field.

The magnetic susceptibility measurements carried out on the zinc blende and chalcopyrite single phase samples, as described in chapter 4, provided us with the spin glass freezing temperature T_g and the Curie-Weiss paramagnetic temperature θ, thus the dependence of these parameters on composition was also established. It was found that they depend mainly on the Mn concentration z. These susceptibility results indicate that despite the apparent single phase condition of the x-ray photographs, two different magnetic phases are observed and these are attributed to crystallographic ordering of the manganese atoms. For many samples, the susceptibility measurements give two transition temperatures, the lower one corresponding to the disordered structure and the higher to the ordered structure. The variation of these transition temperatures with z gives different lines for the chalcopyrite and cubic structures. Turning to the exchange mechanism which takes place, the interesting aspect about the disordered T_g results was that $\ln T_g$ was found to decrease in a linear fashion where the mean spacing between the Mn ions increases with decreasing z. This implies that the exchange interaction decreases exponentially with distance between the manganese spins. An exchange mechanism proposed by Geertsma et al (33) involving

virtual transition from the valence band to Mn $3d^5$ levels was assumed as the one occurring in these wide gap semiconductors. Using the expression involved in this mechanism, the nearest and next nearest neighbour exchange parameters J_1 and J_2 were predicted. All these calculated values were found to agree well with the experimental ones, which was strong evidence in support of our assumption that the Geertsma exchange mechanism is very likely the one taking place.

The electron spin resonance experiments, described in chapter 5, revealed other aspects of the magnetic behavior of the present semimagnetic semiconductor alloys. The presence of two lines in the ESR spectrum verify the results obtained in susceptibility measurements which indicated two different structures. The variation of the ESR line width with temperature indicates that the disordered phase shows spin glass behavior, but the conditions and the behavior of the ordered phase are still not determined.

Finally it is clear that this investigation of the $Zn_{2x}(CuIn)_yMn_{2z}Te_2$ system presented in this thesis has yielded valuable information which was very useful in giving a better understanding of some aspects of the physical behavior of this intriguing new class of materials called semimagnetic semiconductors. However, it would be of interest to make further experimental measurements to determine the ordered structure, which is being investigated by other members in our research group using neutron diffraction techniques.

REFERENCES

1. J.A.Gaj, Proc 15th Int. Conf. Physics of Semiconductors, Kyoto (1980). J. Phys. Soc. Japan 49 Suppl. A 797 (1980).
2. J.K. Furdyna, J. Appl. Phys. 53, 7637 (1982).
3. Peter J. Ford, Contemp. Phys. Vol. 23, No. 2, 141 (1982).
4. J.A.Mydosh, J. Mag Mag. Mat. 7, 237-248 (1978).
5. K.H. Fischer, Physica B86-88, 813 (1977).
6. J.A. Gaj, R.R. Galazka, M. Nawrock, Solid State Commun. 25, 193 (1978).
7. R.R. Galazka, S. Nagata, P.H. Keeson, Phys. Rev. B 22, 3344 (1980).
8. S. Oseroff, Phys. Rev. 25 B, 6584 (1982).
9. M. Escorne, A. Mauger, R. Triboulet, J.L. Tholence, Physica 107 B, 309 (1981).
10. Tom Donofrio, Ph.D. Thesis, University of Ottawa (1986).
11. M. Quintero, Ph.D. Thesis. University of Ottawa (1984).
12. R. Goudreault, Master's Thesis, University of Ottawa (1987).
13. M. Al-Najjar, Master's Thesis, University of Ottawa (1986).
14. S. Manhas, Master's Thesis, University of Ottawa (1987).
15. J.B. Nelson, D.P. Riley, Proc. Phys. Soc. 57 , 160 (1945).
16. D. Mckie, C. Mckie, Crystalline Solids, Nelson, Don Mills (1980).
17. C.K. Williams, T.H. Glisson, J.R. Hauser and M.A. Littlejohn, J. Electronic Mat. 7, 639 (1978).
18. J.P. Shay and G.H. Wernick, Ternary Chalcopyrite Semiconductors, Pergaman Press, New York 1975.
19. E.J. Johnson, Semiconductors and Semimetals, Vol. 3, 154 (1967).

20. R.H. Parmenter, Phys. Rev. 99, 1759 (1955).

21. C. Rincon, J. Gonzalez, G. Sanchez and C. Bellabarba, Nuovo Cimento 2D, 1895 (1983).

22. Allan H. Morrish, " The Principal of Magnetism ", Robert E. Krieger Publishing Company Inc. 1980, Ch. 2,6,7.

23. G. Toulouse, Comm. Phys. 2, 115 (1977).

24. V. Canella and J.A. Mydosh, Phys. Rev. B 6, 4220 (1972).

25. C.N. Guy, Physica B 86-88, 877 (1977).

26. A.P. Murani, Phys. Rev. Lett. 37, 450 (1976).

27. C. Kittel, " Introduction to Solid State Physics ", 5th edition, Published by John Wiley and Sons, Ch. 14.

28. L. Deseze, J. Phys. C10, 31 (1979).

29. J. Villain, Z. Phys. B33, 31 (1979).

30. N. Bloembergen and T. J. Rowland, Phys. Rev. 97, No. 6, 1679 (1958).

31. D. Beckett, Master's Thesis, University of Ottawa (1986).

32. G.E.T. Gonzalves de Silva and L.M. Falicov, J. Phys. C 5, 63 (1972).

33. W. Geertsma, C. Hass, G.A. Sawatzky and Vertogen, Physica, 86-88B, 1039 (1977).

34. P. W. Anderson, Solid State Physics, 14, 142 (1963).

35. J. C. Woolley, S.F. Chehab, T. Donfrio, S. Manhas, A. Manoogian and G. Lamarche J. Mag. Mag. Mat. 66 23-30 (1986).

36. U. Steigenberger, B. Lebech and R.R. Galazka, J. Mag. Mag. Mat. 54-57 1285 (1986).

37. S. Cheab Ph. D. Thesis, University of Ottawa (1986).

38. Abragam and Bleany, " Electron Paramagnetic Resonance of Transition Ions ", Clarendon, Press-Oxford (1970).

39. H. Watanabe, Progress of Theoretical Physics, Vol. 18, No. 4 (1957).

40. C. Kikuchi and J.Lambe, Phys. Rev. 119, 1256 (1960).

41. S.Oseroff, R. Colvo, W. Giriat, J. Appl. Phys. 50, 7738 (1979).

42. J.W. Searl, R.C. Smith, S.J. Wyared, Proc. Phys. Soc. 78, 1174 (1961).

43. S.B. Bhagat, M.L. Spano, J.N. Lloyd, Solid State Commun. 38, 261 (1981).

44. D.J. Webb, S.M. Bhagat, J.K. Furdyna, J. Appl. Phys. 55, 2310 (1984).

45. H.A. Sayad, S.M. Bhagat, Phys. Rev. B 31, 591 (1985).

46. D. Bissonnette, Master's Thesis, University of Ottawa (1988).

47. R. Brun del Re, Ph.D. Thesis, University of Ottawa (1988).

48. J.C. Woolley, G. Lamarche, A. Manoogian, M. Quintero, L. Dierker, M. Al-Najjar, D. Proulx, C. Neal and R. Goudreault, 'Ternary and Multinary Compounds' Proc. of the 7th Int. Conf. Colarado 1986. Ed. S.K. Deb & A. Zunger, Mat. Res. Soc. p.479 (1987)

49. M. Escorne, A. Mauger, Phys. Rev B, 25 4674 (1982).